

The influence of calcination temperature on structure and magnetic properties of pillared clays

Zur Erlangung des akademischen Grades eines
DOKTORS DER NATURWISSENSCHAFTEN

von der Fakultät für

Bauingenieur-, Geo- und Umweltwissenschaften
der Universität Fridericiana zu Karlsruhe (TH)

genehmigte

DISSERTATION

von

Dipl.-Chem.
Cherifa Bachir

aus Oran

Tag der mündlichen Prüfung: 23.09.2009

Hauptreferent: Prof. Dr. Heinz-Günter Stosch.

Korreferent: Prof. Dr. Annie Powell.

Karlsruhe 2009

Cherifa Bachir
Rintheimer Str. 13
76131 Karlsruhe.

Eidesstattliche Erklärung

Hiermit erkläre ich, dass ich die vorliegende Dissertation ohne unzulässige Hilfe Dritter und ohne Benutzung anderer als der angegebenen Hilfsmittel angefertigt habe.

Karlsruhe, den 20.06.2009

Cherifa Bachir

Acknowledgments

I am grateful to Dr. Peter- G Weidler for the countless hours spent patiently discussing, answering questions, for his constructive criticism of the work and knowledge.

I am very indebted to the Deutscher Akademischer Austausch Dienst (DAAD) for the scholarship in the program Research Grants for Doctoral Candidates under the matriculation: A/05/06306.

I am grateful to my PhD supervisor Prof. Dr. Heinz-Günter Stosch for having accepted me after the death of Prof. Dr. Rolf Nüesch and for the helpful discussions and advices.

Prof. Dr. Annie Powell, Dr. Valeriu Mereacre, and Dr. Yanhua Lan, University of Karlsruhe, and Prof. Christian Bender Koch, University of Copenhagen are gratefully acknowledged for magnetic measurements and precious discussions.

I would like to thank all my colleagues of Nanomineralogy group for the continuous encouragement, and the pleasant atmosphere to this thesis.

Special thanks go to Natalie Naguib for participating in the early stages of this work, Dr. Katja Emmerich, Dr. Hartmut Gliemann, Dr. Annett Steudel and Mehdi Adjdir for the precious help and discussions, Dr. Durime Buqezi-Ahmeti for the CEC investigations, Dr. Markus Hauser-Fuhlberg for the precious help and Dr. Frank Friedrich for his help in the Far infrared spectroscopy (FIR) measurement.

A very special thank to Julia Scheiber for supporting me at the end of this thesis by doing a lot of works I would not have managed alone.

Attention is drawn also on Astrid Biedermann and Christian Biedermann for the precious help.

I wish to thank Marita Heinle for the ICP-OES measurements, Brigitte Kiehling for the AAS measurements, Jens Bolle and Sibylle Heidt for the AGM measurements.

My acknowledgement is also for all those who are not cited and supported the present work in any way.

Contents

Acknowledgments

Abstract	I
Zusammenfassung	II

Introduction	1
---------------------	----------

1. Materials and methods	3
---------------------------------	----------

1.1. Parent clay	3
-------------------------	----------

1.1.1. Sedimentation	3
----------------------	---

1.1.2. NaCl saturation and dialysis	4
-------------------------------------	---

1.2. Preparation of pillared clays	4
---	----------

1.2.1. Pillaring solution	4
---------------------------	---

1.2.2. Pillared clays matrix	5
------------------------------	---

1.3. Preparation of magnetic pillared clays	6
--	----------

1.4. Instrumental methods for sample characterization	6
--	----------

1.4.1. X-ray diffraction (XRD)	6
--------------------------------	---

1.4.2. N ₂ gas adsorption	7
--------------------------------------	---

1.4.3. X-ray fluorescence (XRF)	7
---------------------------------	---

1.4.4. Cationic exchange capacity (CEC)	8
---	---

1.4.5. Inductively coupled plasma-optical emission spectroscopy (ICP-OES)	9
---	---

1.4.6. Determination of layer charge	9
--------------------------------------	---

1.4.7. Simultaneous thermal analyses (STA)	10
--	----

1.4.8. Attenuated total reflection infrared spectroscopy (FTIR-ATR)	10
---	----

1.4.9. Far infrared spectroscopy (FIR)	11
--	----

1.4.10. Environmental scanning electron microscope (ESEM)	11
---	----

1.4.11. Magnetic measurements	11
-------------------------------	----

1.4.12. Mössbauer spectroscopy	13
--------------------------------	----

1.5. Characterisation of the parent clay	14
1.5.1. Morphology	14
1.5.2. Chemical composition	14
1.5.3. Cation exchange capacity and layer charge	15
1.5.4. X-ray diffraction	16
1.5.5. N ₂ gas adsorption	18
1.5.6. Simultaneous thermal analysis	18
1.5.7. Magnetic properties	20
1.6. Optimisation of synthesis parameters	21
1.7. Calculation of the filling factor of pillared clays	24
2. Magnetic titanium pillared clays (Ti-M-PILCs)	27
2.1. Titanium pillared clays	27
2.1.1. XRD investigation	27
2.1.2. N ₂ gas adsorption	30
2.1.3. X-ray fluorescence XRF	34
2.1.4. Simultaneous thermal analysis	34
2.1.5. Cation exchange capacity	36
2.2. Magnetic titanium pillared clays	38
2.2.1. XRD investigation	38
2.2.2. N ₂ gas adsorption	40
2.2.3. X-ray fluorescence XRF	43
2.2.4. FTIR investigation	44
2.2.5. Magnetic properties	46
2.2.6. Mössbauer spectroscopy	51
2.3. Discussion	54

3. Magnetic aluminium pillared clays (Al-M-PILCs)	57
3.1. Aluminium pillared clays	57
3.1.1. XRD investigation	57
3.1.2. N ₂ adsorption	59
3.1.3. X-ray fluorescence XRF	63
3.1.4. Simultaneous thermal analysis	64
3.1.5. Cation exchange capacity	66
3.2. Magnetic aluminium pillared clays	67
3.2.1. XRD investigation	67
3.2.2. N ₂ adsorption	69
3.2.3. X-ray fluorescence XRF	72
3.2.4. FTIR investigation	72
3.2.5. Magnetic properties	75
3.2.6. Mössbauer spectroscopy	81
3.3. Discussion	84
4. Magnetic zirconium pillared clays (Zr-M-PILCs)	87
4.1. Zirconium pillared clays	87
4.1.1. XRD investigation	87
4.1.2. N ₂ adsorption	90
4.1.3. X-ray fluorescence XRF	94
4.1.4. Simultaneous thermal analysis	95
4.1.5. Cation exchange capacity	97
4.2. Magnetic zirconium pillared clays	98
4.2.1. XRD investigation	98
4.2.2. N ₂ adsorption	99
4.2.3. X-ray fluorescence XRF	102
4.2.4. FTIR investigation	103
4.2.5. Magnetic properties	105
4.2.6. Mössbauer spectroscopy	110
4.3. Discussion	113

5. Adsorption	115
5.1. Introduction	115
5.2. Theoretical foundation	115
5.2.1. Adsorption isotherm	115
5.2. 2. Adsorption kinetics	116
5.3. Materials and adsorption experiment	117
5.3.1. Materials	117
5.3.2. Adsorption experiment	117
5.3.3. Methods	118
5.4. Results and discussion	118
5.4.1. Adsorption isotherm	118
5.4.2. Adsorption kinetics	122
6. Discussion	125
7. Appendix	127
7.1. Theoretical part	127
7.1.1. Pillared clays	127
7.1.2. Background in magnetism	130
7.2. Ti-M-PILC hysteresis	135
7.3. Abbreviations list	136
8. References	139

Abstract

Magnetic pillared clays (Ti-M-PILCs, Al-M-PILCs, and Zr-M-PILCs) have been prepared from montmorillonite at ambient temperature. Therefore pillared montmorillonite (Ti-PILCs, Al-PILCs, and Zr-PILCs) have been produced at different calcination temperature. Ferrous ions have been added by ion-exchange and reduced by sodium borohydride.

A new evaluation method for gas adsorption data called NLDFT (non local density functional theory) was applied in order to calculate porosity, especially in the range of micropores (< 2 nm). Further investigation using evaluated XRD data, CEC determination, XRF data evaluation and FT-IR spectroscopy were carried out.

In addition to the previous cited methods, the properties of the magnetic pillared clays have been investigated using superconducting quantum interference devices (SQUID) and Mössbauer spectroscopy. Hysteresis, zero field cooled (ZFC) and field cooled (FC) measurements have been performed on different precursor materials prepared by calcination of PILCs at temperatures between 200 and 600 °C. Hysteresis loops have been recorded between -7 and 7 T in the temperature range 2-300 K. ZFC/FC measurements were carried out upon warming up from 2 to 300 K under an applied magnetic field of 39.8 kA m⁻¹. The influence of the calcination temperature of the initial PILC material on the structural and the magnetic properties of the resulted M-PILCs is discussed.

In the case of titanium precursors, the presence of two different Fe-alloy distributions was suggested, a dispersed one for the lower calcined Ti-PILCs, and clusters for the higher calcined ones. In addition the best calcination temperature is 400 °C, which maintained the highest SSA and pore volume with magnetic parameters, suitable for magnetic application.

Similar experiments with Al and Zr-pillars are discussed. A correlation between the XRF data, porosity, filling factor calculation and magnetic properties led to the conclusion that the sample Al-M-PILC-500 is the most stable materials after the magnetization process. The same examination in the case of Zr materials led to the highest stability of the sample Zr-M-PILC-300.

The sorption properties of PILCs and M-PILCs have been tested by copper adsorption. The results show the easiness of the copper sorption on the M-PILCs rather than on the original PILCs.

Zusammenfassung

Aus Montmorillonit wurden magnetische Säulentone (Pillared Clays) (Ti-M-PILCs, Al-M-PILCs und Zr-M-PILCs,) bei Raumtemperatur hergestellt. Hierfür wurden säulenförmige Montmorillonite bei unterschiedlichen Calciniertemperaturen getempert, Eisenionen mittels Ionentausch zugeführt und anschließend mit Natriumborhydrid reduziert.

Eine neue Auswertungsmethode für Gassorptionsdaten, NLDFT (Non Local Density Functional Theory), wurde genutzt, um die Porosität, speziell im Mikroporenbereich (Porenweite < 2 nm) zu berechnen. Weitere Untersuchungen mittels XRD, CEC Bestimmung, XRF und FT-IR Spektroskopie wurden durchgeführt.

Zusätzlich zu den genannten Methoden, wurden die Eigenschaften der Magnetischen Pillared Clays (M-PILCs) mittels SQUID (Superconducting Quantum Interference Devices) und Mössbauer Spektroskopie untersucht. Hysteresen, zero field cooled (ZFC) und field cooled (FC) Messungen wurden für verschiedene calcinierte (200 und 600 °C) PILCs gemessen. Hysteresen wurden in einem Bereich zwischen -7 bis 7 T und in einem Temperaturbereich zwischen 2-300 K aufgenommen. ZFC/FC Messungen wurden unter Aufwärmen der Proben von 2-300 K unter einem angelegten Feld von 39.8 kA m⁻¹ durchgeführt. Der Einfluss der Calciniertemperatur auf die strukturellen und magnetischen Eigenschaften wird diskutiert.

Im Falle des titanbasierten Säulenmaterials, weisen die Daten auf eine unterschiedliche Verteilung der Eisenzumischung hin und zwar für die bei niedrigen Calciniertemperaturen getemperten Ti-PILCs auf eine Verteilung auf alle Porenvolumina im Zwischenraum und für die bei höheren Temperaturen calcinierten auf eine Clusterbildung. Im Weiteren liegt die beste Calciniertemperatur bei 400 °C. Hier wurden die höchste SSA, sowie ein sehr großes Porenvolumen erreicht. Es wurden magnetische Eigenschaften ausgebildet, welche das Material/PILC für magnetische Anwendungen nutzbar macht.

Ähnliche Experimente wurden für Al- und Zr-Pillars durchgeführt. Die Korrelation zwischen den XRF Daten, der Porosität, den Füllfaktorberechnungen und den magnetischen Eigenschaften führen zu dem Schluss, dass 500°C die am besten geeignete Calciniertemperatur zur Herstellung von Al-PILCs ist. Für Zr-PILCs ergab sich hierfür eine Calciniertemperatur von 300 °C.

Die Sorptionseigenschaften der Pillared Clays und der Magnetischen Pillared Clays wurde mit Kupferadsorption getestet. Die Resultate zeigen eher eine Bevorzugung der Kupfersorption auf den M-PILCs gegenüber auf den originalen PILCs.

Introduction

Clays are low cost and readily available materials functioning as excellent cation exchangers, and have often been used in adsorption and catalysis. One important class of clay derivatives is pillared clays obtained from the insertion of metal oxide species into the clay (Kloprogge, 1998). Pillared clays with magnetic behaviors are very promising and provide new effective magnetic carriers suitable for a wide range of applications, such as magnetic separation.

The idea of combining interesting adsorption properties of materials with magnetic properties to produce novel kinds of adsorbents has become very attractive. This issue has recently been the subject of studies in some initiative works. An example is the use of polyacrylic acid-bound iron oxide magnetic nanoparticles for adsorption of methylene blue (Mak and Chen, 2004). Another example is the use of activated carbon/iron oxide magnetic composites for the adsorption of volatile organic compounds (Oliveira *et al.*, 2002) and the use of montmorillonite-iron oxide magnetic composites for the adsorption of metal cations (Oliveira *et al.*, 2003).

In the first experiment of magnetic montmorillonite synthesis, NaBH_4 solution has been used as a reducing agent for the iron exchanged-montmorillonite (Zhang and Mantthiram, 1996). In this work, new magnetically layered systems from different pillared matrix Ti-M-PILCs, A-M-PILCs, and Zr-M-PILCs have been prepared and characterised. The influence of the calcination temperature for each set of experiment has been examined.

An initial investigation using several methods was mandatory to check the textural properties and the thermal stability of the original titanium, aluminium, and zirconium pillared clays upon heat treatment. The textural properties of the magnetic form M-PILCs were also investigated. The properties of the obtained magnetic materials have been investigated using superconducting quantum interference devices (SQUID) in conjunction with Mössbauer spectroscopy. These methods including hysteresis and ZFC/FC measurements give a deep view on the intrinsic behaviour of the materials. Furthermore, this combination of characterization methods in this work will contribute new insight which is not available in this kind. Furthermore the present results are essential for the future sorption experiments.

In this study, a new advanced evaluation method for gas adsorption data was applied. This method is based on the NLDFT (non local density functional theory) and provides reliable information on pore size distribution, especially the micropore range.

In the following paragraphs, a description of the most important part of this work will be given.

First in Chapter 1, a detailed description of materials and methods has been carried out. In this part a complete characterisation of the starting clay, the optimisation of synthesis parameters, and the calculation of the filling factor of pillared clays were presented.

After that, Chapters 2, 3, and 4 focused on the examination of the influence of calcination temperature on the structure and the magnetic properties of three different pillared clays. Each chapter starts with the investigation of the pillared form followed by that of the pillared magnetic form. For these Chapters the discussions were also included.

A further topic in this work reported on the copper adsorption using some obtained pillared clays and their magnetic forms. A comparison of the adsorption features of these materials as function of pillar species was presented.

1. Materials and methods

1.1. Parent clay

The following montmorillonite was used as starting clay, on which a lot of research has already been performed in our institute: SWy-2 from Wyoming, USA supplied by the Clay Minerals Society. The clay was purified by conventional sedimentation collecting the < 2 μm fraction, followed by treatment with sodium chloride to ensure complete conversion to the sodium-exchanged form Na-SWy-2.

1.1.1. Sedimentation

The separation of the clay minerals fraction is important for the investigation of their properties. A quantitative XRD analysis revealed up to 75 % smectite in SWy-2 as shipped. After separation; the smectite content increased to 95 % (Chipera and Bish, 2001). In order to prepare pillared clays, aim of this work, it was necessary to concentrate the < 2 μm fractions, responsible of the exchange and swelling properties.

The fraction < 2 μm was obtained by sedimentation. 10 g of the starting clay were dispersed in 1 l of distilled water. In order to obtain a fully dispersed suspension 0.1 g of NaCl was added. The dispersion was stirred for 20 min in ultrasound (Emmerich and Steudel, private communications) and 24 h in magnetic stirrer. Chipera *et al.*, (1993) added to the clay suspension a small amount of $(\text{NaPO}_3)_6$ as dispersant. In this work, NaCl was used as dispersant in order to avoid any probability of cation exchange (Emmerich, private communication). After reaching the calculated time t given by the Stokes law (Stokes, 1845) the fraction < 2 μm was separated.

The Stokes settling time of particles < 2 μm is:

$$t = 18\eta_0 h / (\rho - \rho_0) g d^2 \quad (1)$$

where: t : the Stokes settling time

η_0 : the viscosity of water

h : the settling distance of the particles

ρ : the density of the clay mineral

ρ_0 : the density of the water, depending on the temperature

g : the gravitational acceleration and d : the particle diameter.

1.1.2. NaCl saturation and dialysis

As reported by literature (Cool and Vansant, 1998), the parent clay is usually in the inexpensive Na⁺-form when applied as basic substrates for pillaring. This choice is based on the best hydration and exchange properties of sodium.

After sedimentation, the fraction < 2 µm was coagulated with NaCl (the amount of NaCl depends on the sample amount). The sediment was then separated and washed with distilled water by dialysis. The dialysis tubes were previously cleaned in boiling water to eliminate contaminations for 2 h. The sediment was dialyzed for 2-3 weeks until the conductivity of the surrounding water reached 2 µs/cm.

Finally, the slurry was dried at 60 °C and milled slightly in an agate mortar. The obtained sample is denoted as Na-SWy-2.

1.2. Preparation of pillared clays

The pillaring of clays is a well established technique in the preparation of porous solids. It is an easy and controllable way to introduce porosity in an inexpensive substrate (Cool and Vansant, 1998). The physicochemical properties of the pillared clays depend on several synthesis parameters, including the nature and the concentration of the metal ion, the method of preparation, etc.

In this work, titanium, aluminium and zirconium pillared clays have been manufactured. The influence of some synthesis parameters of aluminium and zirconium pillared clays such as the ageing time of pillaring solution and the polycation/clay ratio is reported.

1.2.1. Pillaring solution

Titanium pillaring solution was prepared according to the method reported by Sterte, (1986). Titanium tetrachloride was hydrolysed with 6 M hydrochloric acid HCl and diluted with deionized water until a final concentration of [Ti⁴⁺] = 0.82 M was reached. This solution was aged for 3 h before use under stirring.

For preparing aluminium pillaring solution a sodium hydroxide solution 0.225 M NaOH was dropwise added with vigorous stirring to a 0.5 M AlCl₃.6H₂O solution. The amounts of sodium hydroxide added were calculated in order to obtain OH/Al molar ratio of 2. This solution was aged for 24 h and 48 h under agitation. For preparing zirconium pillaring solution a 0.1 M zirconyl oxychloride ZrOCl₂.8H₂O (Yamanaka *et al.*, 1979) was prepared just before use in order to avoid ageing and after ageing for 24 h.

1.2.2. Pillared clays matrix

Intercalation

The intercalated montmorillonites were prepared by slow addition under stirring of the corresponding amounts of pillaring solution to the suspension of Na-SWy-2 in order to obtain the corresponding cation/clay ratio expressed in mmol/g clay (Tab. 1.1). The mixture was stirred for the corresponding intercalation time. The solids were separated by centrifugation (4500 rpm, 10 min), washed with distilled water and dried at 60 °C.

Calcination

The intercalated solids were calcined at different temperatures (200, 300, 400, 500 and 600 °C) for the corresponding time, at a heating rate of 1 °C/min from room temperature up to the calcination temperature.

The different parameters of preparation as well as the nomenclature of aluminium and zirconium materials are collected in the Tab. 1.1.

Table 1.1: Preparation conditions of the different pillared clays

Pillaring solution						
	Ti ^a	Al			Zr	
Solutions	TiCl ₄ + HCl	AlCl ₃ .6H ₂ O+NaOH			ZrOCl ₂ .8H ₂ O	
Molar ratios	H/Ti=1.2	OH/Al=2				
Ageing time (h)	3	48 ^b	24	24	0 ^d	
Pillared clays matrix						
	Ti-PILCs ^a	Al-PILCs			Zr-PILCs	
Cation/clay (mmol/g)	10	4 ^b	10	15	10	
Clay suspension (% weight)	0.4	0.5			2	1
Intercalation time (h)	16	4 ^b	17		24	
Calcination temperatures (°C)	200, 300, 400, 500, 600					
Calcination time (h)	3	4 ^c			2 ^e	
Nomenclature	-	Al-1	Al-2	Al-3	Zr-1	Zr-2

^a: Sterte, 1986.

^b: V. Lenoble *et al.*, 2002.

^c: Elmchaouri and Mahboub, 2005.

^d: Ben Chaabene *et al.*, 2004.

^e: Mishra and Rao, 2005.

1.3. Preparation of magnetic pillared clays

The first experiment using NaBH_4 solution as a reducing agent for the iron exchanged-montmorillonite was carried out by Zhang and Manthiram, (1996). Subsequently, Naguib *et al.*, (2003) tried to apply this process to the pillared clays. In the present work further new magnetic PILCs were prepared. The study of the dependency of the calcination temperature on the obtained Al, Ti and Zr magnetic PILCs was investigated.

Magnetic properties were conveyed to the pillared clays by ion-exchange of the present interlayer ions with an excess of ferrous iron (0.2 M $\text{FeCl}_2 \cdot 4\text{H}_2\text{O}$) solution and stirring on a magnetic stirrer for 24 h. The products were centrifuged and washed several times until chloride free and dried at 60 °C. 1g of the iron exchanged Ti-PILCs was then suspended in 50 ml of deionized water and stirred. A freshly prepared solution of 0.5 M NaBH_4 was then added slowly to the suspension at room temperature. This product was stirred for 1 h, separated, freeze-dried and stored in a desiccator.

1.4. Instrumental methods for sample characterization

1.4.1. X-ray diffraction (XRD)

X-ray diffraction is the most important tool for qualitative and quantitative analyses of clay mineral samples as well as the synthesized pillared clays. It provides a large amount of information for mineral identification, detection of impurities, layer charge determination, and ethylene glycol solvation. For pillared clays, the change in the (001) spacing upon pillaring and the nature of pillar oxides are provided.

X-ray diffraction (XRD) was carried out on a Siemens D5000 diffractometer equipped with a graphite secondary monochromator and $\text{CuK}\alpha$ radiation ($\lambda = 1.5418 \text{ \AA}$) at 40 kV and 40 mA. In order to optimize the (001) intensities of pillared clays, oriented clay-aggregate specimens were prepared by drying clay suspensions on glass slides. Diffractograms were recorded over the range 2-12 °2 θ (step size 0.02 °2 θ , step time 4 s) for glass slide samples, and 2-72 ° (step size 0.025 °2 θ , step time 10 s) for powder samples.

Qualitative phase analysis was done by using Brindley and Brown, (1980) and Diffrac Plus evaluation 10.0 provided by Bruker AXS.

The full width half maximum (FWHM) values were determined by single line fitting with TOPAS 3.0 provided by Bruker AXS. A pseudo-Voigt function was applied as profile function. The background was fitted by a polynomial of 4th grade and the FWHM was modeled by the function described by Caglioto *et al.* (1958) using the UVW parameter. The instrumental contribution to the line broadening was calculated by TOPAS using the

instrumental parameters, such as goniometer radius, samples area viz. type of slits applied during measurement.

1.4.2. N₂ gas adsorption

Nitrogen adsorption measurements were performed using a Quantachrome Autosorb-1MP instrument in the relative pressure range p/p_0 from 10^{-5} to 1. The samples were outgassed overnight at 110 °C prior to the adsorption analysis. Specific surface areas were calculated according to the BET equation (Brunauer *et al.*, 1938). The non-local density functional theory (NLDFT) has been shown to give quantitatively correct pore size distributions in silica materials with cylindrical mesopores (Neimark and Ravikovitch, 2001 and Ravikovitch and Neimark, 2001), and extended to the range of micropores (Thommes *et al.*, 2006). This theory provides a set of model isotherms $\varphi(p,x)$ for homogenous pores of given sizes, which are then applied to the experimentally measured adsorption isotherm $X(p)$ in the numerical solution of the following equation:

$$X(p) = \text{Integral } f(x) \varphi(p,x) dx \quad (2)$$

to obtain the pore size distribution of adsorbent $f(x)$ (Seaton *et al.*, 1989). For the pillared clays and magnetic pillared clays the NLDFT was used to calculate total pore volume (V_p at $P/P_0 = 0.7$), micropore volume (V_{mp} , width less than 2 nm), and mesopore volume (V_{mes} , width between 2 and 50 nm) from the adsorption branch assuming cylindrical pore geometry. The NLDFT cumulative pore volume and the corresponding differential pore volume distribution curves of all pillared materials were also illustrated.

The N₂ adsorption-desorption isotherms of samples have been also established, in order to get information on the forms of the isotherms and their loop hysteresis which are related to the pore nature existing in their structure (Sing *et al.*, 1985 and Lowell *et al.*, 2006).

1.4.3. X-ray fluorescence (XRF)

The X-ray fluorescence (XRF) analyses provide the chemical compositions of the parent clay and the pillared clays. The chemical composition reported as oxides (%wt.) of pillared clays is important to determine the additional content of the intercalated element as well as the content of the additional iron of the magnetic pillared clays.

XRF measurements were performed using a MagiXPRO spectrometer from Philips, equipped with a rhodium X-ray tube, on air dry powdered samples fused with lithium tetraborate. The

loss on ignition, LOI, was determined separately by storing a sample in an oven at 1000 °C for 2 h. For each type of pillared clays differing in the pillaring agent, more calibrations of the TiO₂, Al₂O₃, and ZrO₂ content were required.

The structural formula, therefore the molecular weight of the parent clay can also be calculated from the chemical composition according to Köster, (1977) after measuring the layer charge.

1.4.4. Cationic exchange capacity (CEC)

The cation exchange capacity is one of the basic properties of clay minerals especially smectites. It has two origins; one origin is the isomorphic substitution in the tetrahedral and/or octahedral sheet such as substitution of aluminium by magnesium or silicon by aluminium which leads to a negative net charge. This part is considered to be constant since it is almost pH independent. The second origin is the dissociation of the aluminol groups on the edges, since the acidity of these groups is weak, the edge charges are pH dependent and the CEC depends on the pH. Thus the total CEC is the sum of the interlayer and edge CEC. At pH= 7 roughly 20 % of the CEC of smectites is located at the edges (Lagaly, 1981). In the acid pH range, the edges are positively charged and do not contribute to the measured CEC. However, in the basic pH range, the edges are negatively charged and contribute to the CEC.

CEC of the parent clays as well as the pillared ones was measured by the copper-triethylenetetramine exchange according to Meier and Kahr (1999). Prior to this exchange the samples were stored over magnesium nitrate (53 % r.h.) for at least 24 h. 50 -100 mg of the samples was dispersed in 10 ml of deionised water and 5 ml of a 0.01 M copper(II)-triethylenetetramine sulphate solution [Cu(trien)]²⁺, the dispersions were shaken for 3 h, then centrifuged at 4500 rpm for 10 min. The concentration of the [Cu(trien)]²⁺ complex was determined by photometry ($\lambda = 580$ nm) in the clear supernatant using UV-Vis Spectrometer Genesys 10 UV. Before starting the measurements a calibration curve with standard solutions was mandatory. The CEC measurements were always done in duplicate and two standards clay materials were used, volclay and calciegel which have CEC of 85 and 63 meq/100 g, respectively. The CEC value is related to the completely dehydrated sample, thus the water content was measured using either the TG/STA measurement or oven drying. More details for the CEC computation were given by Steudel, (2008).

1.4.5. Inductively coupled plasma-optical emission spectroscopy (ICP-OES)

The ICP-OES was used as an additional investigation to the CEC measurements. This method which allows the determination of ion concentrations in solution, was applied in order to quantify the exchanged cation concentrations in the supernatant solution after the exchange reaction with the $[\text{Cu}(\text{trien})]^{2+}$ complex. Furthermore, for the parent clay only the interlayer cations mostly Na^+ , Mg^{2+} , Ca^{2+} , and K^+ have been analysed. In addition to the interlayer cations, aluminium, zirconium, and titanium are also measured for the pillared clays. This is important to check the irreversibility of the pillaring element exchange.

For these determinations, 5 ml of the CEC supernatant solution was diluted with deionised water by 1:3 and acidified with nitric acid (65 %) until $\text{pH} \leq 2$. 10-20 ml of the mixture were needed for the analyses. During the measurements some additional dilutions were required (Heinle, private communication).

A Horiba Jobin Yvon, Typ JY 38 S ICP-emission spectrometer was used for analysis. Detailed information on the general system and working parameters as well as the analysed elements wavelengths is provided in Tab. 1.2.

Table 1.2: Experimental parameters and wavelengths of the analysed ions for ICP-OES.

	Parameters	Wavelengths	
		Elements	Wavelength (nm)
Monochromator	Czerny-Turner-specification (1 m)		
HF-Generator	Frequency 40.68 MHz/ Power 1100 W	Sodium	589.592
ICP-Torch	Demountable torch/ ceramic injector tube	Calcium	317.933
Nebulizer chamber	Cyclone chamber	Magnesium	279.553
Nebulizer	Burgener Graphit Mira Mist HS	Potassium	766.490
Argon gas flow	Plasma-/Coolinggas 12.0 l/min	Aluminium	396.152
	Protective gas 0.2 l/min Nebulizer gas 0.71 l/min	Zirconium	343.823
Sample uptake	Flexible-tube pump 1 ml/min	Titanium	337.280

1.4.6. Determination of layer charge

The properties of the smectites are also determined by their layer charge. It involves charge per $[\text{O}_{20}(\text{OH})_4]$ and the sum of the tetrahedral and octahedral charges. The interlayer cation exchange capacity originating from layer charge ξ can be deduced by the equation (3)

in terms of the molecular weight M of a formula unit (f.u) or half unit cell (u.c) (Mermut and Lagaly, 2001):

$$\text{Interlayer CEC (meq/100 g)} = \xi \text{ (eq/mol)}/M \text{ (g/mol)}*10^5 \quad (3)$$

For the layer charge determination (Lagaly, 1994), 100 mg of the sample were dispersed in 3 ml dodecylammonium formiate and stored at 60 °C. After 3 days the solid was separated by centrifugation, washed with ethanol once, and once again dispersed in fresh dodecylammonium formiate solution and stored again at 60 °C. Afterwards, the samples were washed with ethanol 16 times. Textured samples were obtained by dispersion in 3 ml ethanol together with small amounts of talc as XRD line standard. After drying the samples were stored in a desiccator over P₂O₅ until their basal spacings were recorded by XRD (Rühlicke and Kohler, 1981). The layer charge was calculated as recommended by Olis *et al.*, (1990) using the basal spacing of the dodecylammonium derivative ($n_c= 12$):

$$\xi = (d_{001}-5.52)/32.98 \quad (4)$$

1.4.7. Simultaneous thermal analyses (STA)

Simultaneous thermal analysis STA is a combination of thermogravimetry (TG) with differential thermal analysis (DTA) or differential scanning calorimetry (DSC). It is a very important device additional to XRD, XRF analysis among others. The most important reason for investigating pillared clays by STA is the thermal stability, which is directly related to the structural water and dehydroxylation temperature. STA were performed on 100 mg samples using a Netzsch STA 449C Jupiter-QMS 430 C Aeolos, with nitrogen as protective gas (20 ml/l) and synthetic air as purging gas (50 ml/l), with a heating rate of 10 K/min from 35 °C up to 1100 °C. Prior to the measurements the samples are stored in a dessicator over a saturated magnesium nitrate solution (Mg(NO₃)₂, 53 % r.h.).

1.4.8. Attenuated total reflection infrared spectroscopy (FTIR-ATR)

The attenuated total reflection ATR is a rapid, simple and very useful technique to characterize surfaces of minerals. This method was, therefore, used to investigate whether larger amounts of Fe-oxides are present on the outer surface. The (FTIR-ATR) spectra were obtained on a Bruker IFS66 with a DTGS detector and globar source. The ATR device was a Golden Gate single reflection diamond cell and the powder samples were pressed on to the

diamond with a torque of 90 cNm. For each sample 64 scans in the mid infrared region (400-4000 cm^{-1}) were recorded with a resolution of 4 cm^{-1} . In order to emphasize differences due to pillaring and the magnetization process Na-SWy-2 was applied as background.

1.4.9. Far infrared spectroscopy (FIR)

Vibrations in the far infrared reveal direct information about the interlayer species (Ishii, *et al.*, 1967, Velde and Couty, 1985, and Prost and Laperche, 1990).

In the present work, FIR was used to check the presence of iron oxides after the magnetization process. Far infrared spectra were collected at the IR-Beamline (IR1) of the synchrotron light source ANKA at the Forschungszentrum Karlsruhe.

For the measurements polyethylene pellets were pressed using a ratio of 2-6 mg sample powder to 55-100 mg polyethylene. The measurements were obtained in transmission mode using a Bruker IFS66v/S spectrometer operating under vacuum. The spectrometer was equipped with a Bolometer detector, operated at 4.2 K. A 6 μm multilayer beamsplitter (mylar/Si) was used, and for intensity attenuation a Si-window was set into the beam behind the sample holder. With this setup 128 scans in the 700-20 cm^{-1} spectral range were recorded with a resolution of 4 cm^{-1} . Spectral manipulation such as matrix subtraction and normalisation due to the slightly decreasing synchrotron electron beam current had to be performed, using the OPUS software package (Bruker Optics GmbH).

1.4.10. Environmental scanning electron microscope (ESEM)

The particle morphology of the parent clay was observed with an environmental scanning electron microscope (ESEM) (Philips ESEM XL 30 FEG). A chamber atmosphere of 1 Torr and an acceleration voltage of 20 kV were applied. The used holder consists of Al, which was laminated with an adhesive carbon foil. Very small amounts of the powdered samples were dispensed onto the foil.

1.4.11. Magnetic measurements

Alternating gradient magnetometer (AGM)

Magnetization measurements at room temperature were carried out on alternating gradient magnetometer Micromag 2900. The mass of samples used for measurements are between 2-5 mg.

Superconducting quantum interference devices (SQUID)

The magnetic measurements were carried out using a Quantum Design SQUID magnetometer MPMS-XL, which works between 1.8 and 400 K and dc applied fields ranging

from -7 to 7 T. Measurements were performed on a polycrystalline sample placed in a plastic container. The mass of samples used for measurements are between 10-13 mg. Hysteresis curves were recorded between -7 and 7 T at 2, 5, 10, 50, 100 and 300 K, respectively. The specific saturation magnetization (M_s), saturation remanent magnetization (M_{rs}), coercivity (H_c), coercivity of remanence (H_{cr}), magnetic squareness (M_{rs}/M_s), and the H_{cr}/H_c ratio were determined from the hysteresis curves. The shape of a hysteresis loop is determined by the domain state such as single domain (SD), multi domain (MD), pseudo-single domain (PSD) and superparamagnetism (SPM) (Muskowitz, 1991). Loops for SD (with high H_c and M_{rs}) materials are typically wider than loops for MD materials. The hysteresis loop parameters M_{rs}/M_s and H_{cr}/H_c have proven very useful in distinguishing domain state. Thus, the M_{rs}/M_s - H_{cr}/H_c diagram at 300 K of magnetic materials was compared with that obtained for magnetite by Muskowitz (1991).

ZFC/FC measurements were carried out as follows: after the sample was cooled from 300 to 2 K at $H=0 \text{ kA m}^{-1}$, subsequently a field of 39.8 kA m^{-1} was applied at $T=2 \text{ K}$ and the ZFC magnetization M_{ZFC} (and the corresponding susceptibility χ_{ZFC}) was measured between 2 and 300 K. The sample was again cooled to 2 K in the presence of the same field H and the temperature dependence of FC magnetization M_{FC} (χ_{FC}) was measured between 300 and 2 K. The Weiss constant, θ , and Curie constant, C , were determined by fitting the data of χ_{FC} deduced from FC-curves at 39.8 kA m^{-1} to the Curie-Weiss law (Morrish, 1965 and Suzuki *et al.*, 2003) in the paramagnetic region given by:

$$\chi_{FC} = \text{const} + C/(T - \theta) \quad (5)$$

the Curie constant C is given by:

$$C = N\mu^2/3k = N(p_{\text{eff}}\mu_B)^2/3k \quad (6)$$

where N are the atoms/cm³, μ is the number of magnetons, μ_B is the Bohr magneton ($9.27400915(23) \times 10^{-24} \text{ J T}^{-1}$) and k is the Boltzmann's constant, ($1.3806504(24) \times 10^{-23} \text{ J K}^{-1}$).

The effective magnetic number of Bohr magnetons p_{eff} related to C can be also deduced:

$$p_{\text{eff}} = (C3k/N\mu_B^2)^{1/2} \quad (7)$$

1.4.12. Mössbauer spectroscopy

Fifty years ago, Rudolf L. Mößbauer, while he was working on his doctoral thesis under Professor Maier-Leibnitz at Heidelberg “Germany”, discovered the Mössbauer effect (Mössbauer, 1958). This phenomenon developed rapidly to a new spectroscopic technique, called Mössbauer spectroscopy.

The most important information to be gleaned from Mößbauer spectra is on the hyperfine interactions between the Mößbauer nuclei and their electronic environment in solids, i.e., the chemical or isomer shift (IS), the electric quadrupole splitting (QS) and the magnetic hyperfine field, B_{hf} of the Mössbauer pattern. These provide information on the chemical state of the iron, mainly on its valence state (Fe^{2+} or Fe^{3+}) and its coordination state, as well as on the magnetic properties of the iron compounds.

In this work, Mössbauer spectroscopy was necessary to get more detailed information on the iron valence as well as magnetic properties of the synthesized magnetic pillared clays; even iron is only a minor constituent of these materials. Mössbauer spectra were acquired using a conventional spectrometer in the constant acceleration mode equipped with a ^{57}Co source (3.7 GBq) in rhodium matrix. Isomer shifts are given relative to the centroid of the spectrum of alpha-Fe at room temperature. The sample was inserted inside an Oxford Instruments Mössbauer-Spectromag 4000 Cryostat while the sample temperature was varied between 3 and 300 K.

1.5. Characterisation of the parent clay

1.5.1. Morphology

The starting material SWy-2 consists largely of Na-rich smectite, this smectite is montmorillonite and possesses mainly Na exchange cations (William and Moll, 2001). Fig. 1.1 shows the typical layered morphology of the smectite particles.

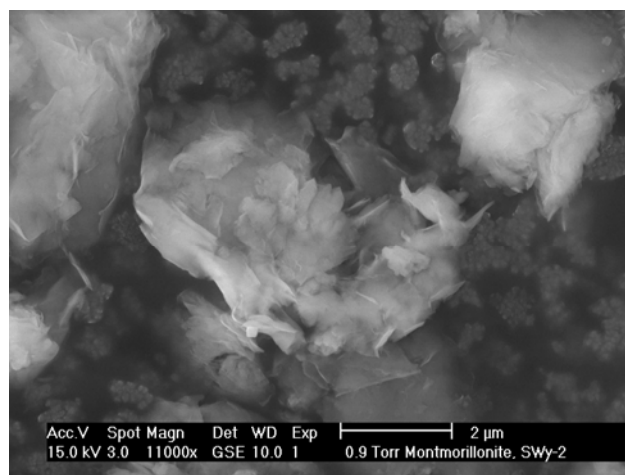


Figure 1.1: ESEM picture of SWy-2

1.5.2. Chemical composition

The chemical composition of the starting clay SWy-2 and the sodium saturated one Na-SWy-2 is given in Tab. 1.3. After sodium saturation the sodium content increased. These data show also a decrease of the CaO and K₂O content. For further investigations the chemical composition of Na-SWy-2 will be used for the computation of the structural formula.

Table 1.3: Chemical composition reported as oxides (%wt.) of SWy-2 and Na-SWy-2.

Oxides	SWy-2	Na-SWy-2
SiO ₂	61.75	60.42
Al ₂ O ₃	18.34	19.79
Fe ₂ O ₃	3.78	3.99
MnO	0.03	0.01
MgO	2.47	2.34
CaO	1.61	0.13
Na ₂ O	1.39	2.21
K ₂ O	0.60	0.11
TiO ₂	0.15	0.11
P ₂ O ₅	0.05	0.02
SO ₃	0.36	0.02
LOI	9.50	10.85

1.5.3. Cation exchange capacity and layer charge

The values of the measured layer charge (Lagaly, 1994 and Olis et al., 1990), the measured CEC (Kahr and Meier, 1999), the molecular weight calculated according to Köster, and the corresponding calculated CEC ((Mermut and Lagaly, 2001) are regrouped in Tab. 1.4. The measured layer charges are in agreement with that of montmorillonite (0.25-0.40 eq/FU, Mermut and Lagaly, 2001). On one hand, the calculated CEC is derived from XRF data and measured layer charge correspond only to the interlayer CEC and should be lower than the measured CEC, in contrast to the CEC value of raw material SWy-2. On the other hand, the measured CEC of the raw material SWy-2 is slightly lower than that of the <2 μm Na-SWy-2 due to the presence of impurities in the raw material.

Thus, only the chemical composition of the < 2μm Na-SWy-2 combined with the measured layer charge was used to calculate the structural formula of the < 2μm Na-SWy-2, thus the computation of the molecular weight per unit cell (Tab. 1.4):



Table 1.4: Layer charge and cation exchange capacity of SWy-2 and Na-SWy-2.

Samples	SWy-2	Na-SWy-2
Measured ζ (eq/mol)	0.30	0.30
Measured CEC (meq/100g)	78	85
<i>M</i> (g/mol)	753.09	746.83
Calculated CEC (meq/100g)	82	81

In addition, the interlayer cation content, mostly Na⁺, Mg²⁺, Ca²⁺, and K⁺, was measured by ICP-OES for SWy-2 and Na-SWy-2 (Tab. 1.5) after the exchange reaction with the [Cu(trien)]²⁺ complex. The Na⁺ content increased after saturation with NaCl. This increase is accompanied by a decrease in Mg²⁺, Ca²⁺, and K⁺ contents.

Table 1.5: Interlayer content in meq/100 g measured by ICP-OES of SWy2 and Na-SWy-2

Interlayer cations	SWy-2	Na-SWy-2
Mg ²⁺	17	6
Ca ²⁺	29	3
Na ⁺	44	77
K ⁺	2	0
Sum (CEC)	92	85

1.5.4. X-ray diffraction

The parent clay Na-SWy-2 was analyzed as air dried powders and oriented clay mineral aggregates prepared by suspending the sample in deionized water and pipetting the suspension onto a glass slide. Oriented samples were investigated under ambient room temperature, and after solvating in an ethylene glycol EG atmosphere as outlined by Moore and Reynolds (1989). To obtain ethylene glycol solvation, the samples were stored in a desiccator over ethylene glycol for 48 h at room temperature. As shown in Fig. 1.2 and Tab. 1.6, the Na-SWy-2 displays d_{001} of 1.24 nm. Ethylene glycol EG solvation increases this basal spacing to 1.69 nm with strong reflection which confirms the existence of smectite. The shifted higher-order $00l$ reflections of the EG solvated Na-SWy-2 are given in Tab. 1.6. The powder XRD patterns of SWy-2 shows the presence of smectite mostly montmorillonite, and a slight indication of muscovite and/or illite (Fig. 1.3).

Table 1.6: $00l$ reflections of air dried and EG solvated Na-SWy-2.

Basal spacing d_{001}	Air dried (nm)	EG (nm)
001	1.24	1.69
002	n.p	0.84
003	n.p	0.56
004	0.31	0.42
005	n.p	0.33

n.p: not present.

The presence of impurities such as quartz, feldspars, and calcite is also indicated. After sedimentation and the subsequent NaCl saturation, the reflections of calcite and feldspar disappeared. However, the powder diffractograms still reveal reflections corresponding to quartz. For both materials, the d_{060} is 0.1496 nm and showed that these materials are dioctahedral (Brindley and Brown, 1980).

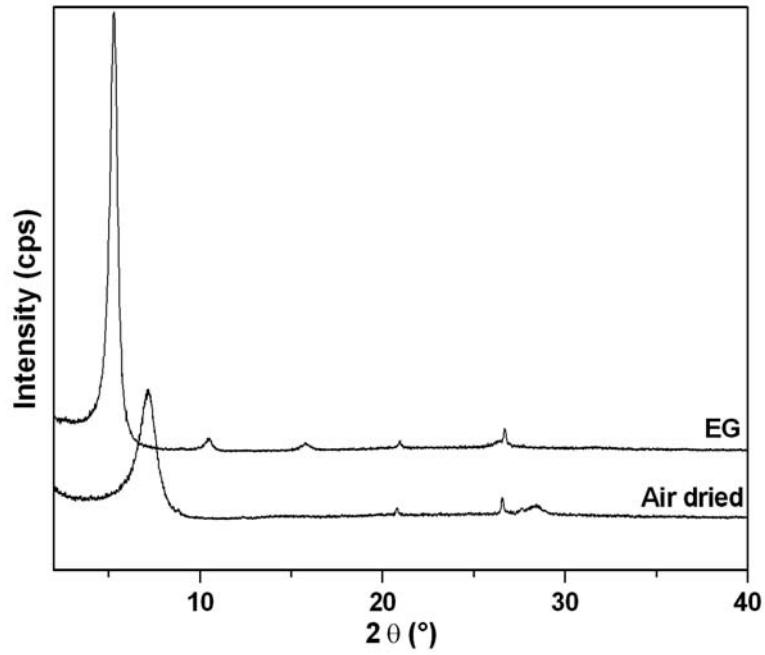


Figure 1.2: Na-SWy-2 in the oriented air dried and ethylene glycol solvated.

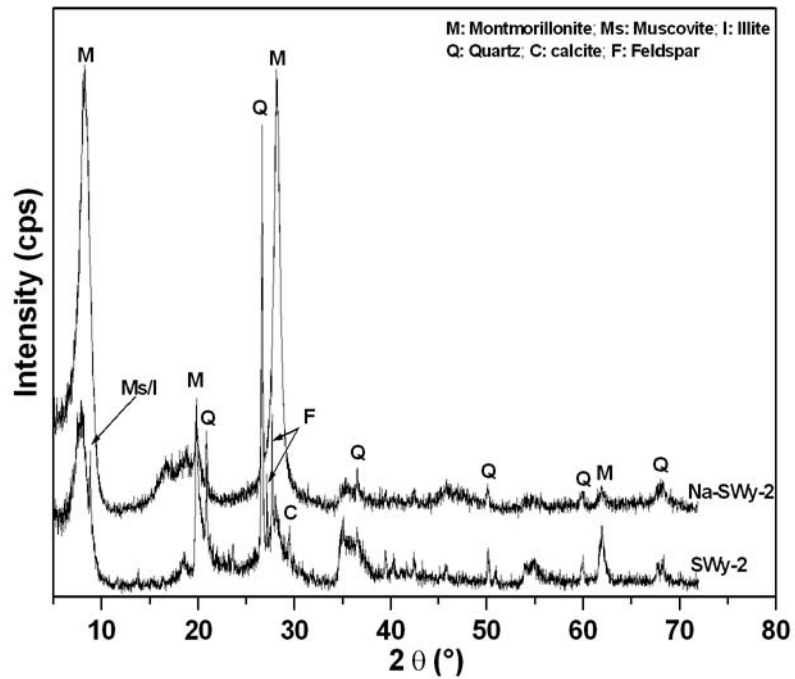


Figure 1.3: Powder X-ray diffractogram of SWy-2 and Na-SWy-2.

1.5.5. N₂ gas adsorption

The specific surface areas of the starting clays are 46 and 50 m²/g for SWy-2 and Na-SWy-2, respectively. Furthermore, the application of the NLDFT method does not show any micro- and mesopore size distribution. The N₂ isotherms (Fig.1.4) exhibit a type II shape, characteristic of non-porous materials or macroporous materials (Sing *et al.*, 1985). The existence of hysteresis behaviour indicates the presence of mesoporosity. This latter is inherent in the clay itself and arises from stacking defects (Hutson, 1999). These stacking defects are the result of the attraction between negatively charged basal surfaces and positively charged crystal edges (Van Olphen, 1963).

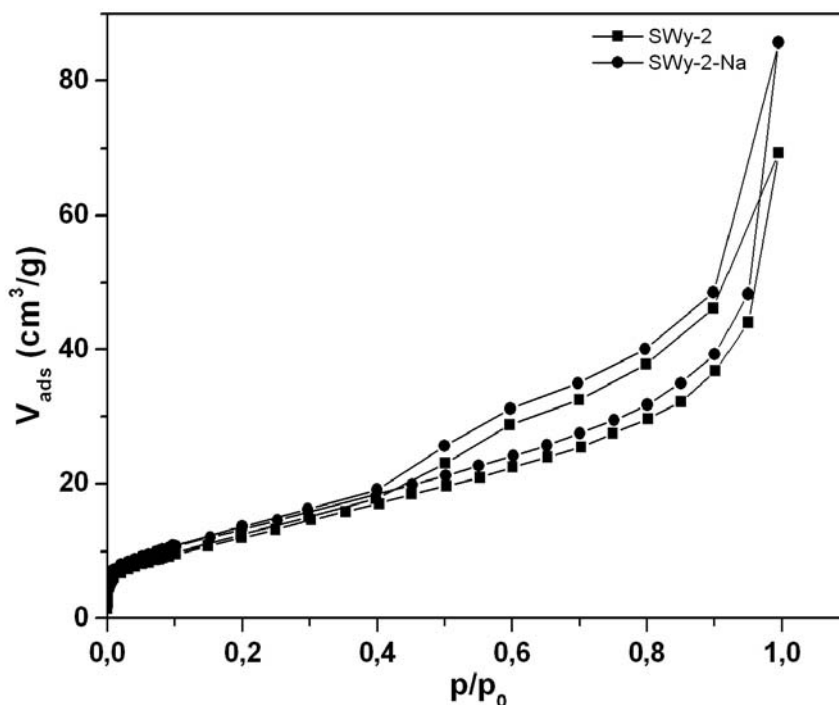


Figure 1.4: N₂ isotherms of SWy-2 and Na-SWy-2.

1.5.6. Simultaneous thermal analysis

In dependence of the temperature, smectites show four characteristic reactions during thermal analysis; dehydration, dehydroxylation, decomposition, and recrystallisation (Niederbudde *et al.*, 2002). During dehydration adsorbed water from outer surface and interlayer water from inner surfaces desorbed in an endothermic reaction between room temperature and 350 °C (Mackenzie, 1970 and Greene-Kelly, 1966). Above 400 °C dehydroxylation or the release of the structural water takes place as endothermic reaction. The

decomposition (endothermic reaction) started at temperatures between 850 and 920 °C, where a loss of crystalline order in the smectite phases occurs. Recrystallisation (exothermic reaction) takes place between 910 and 980 °C, which indicates the formation of anhydrous high temperature phases (Steudel, 2008).

Both SWy-2 and Na-SWy-2 were analysed by STA (Fig. 1.5 and 1.6). The endothermic and exothermic behaviours as well as the associated H₂O-MS curves of these materials are similar. However, no CO₂-MS curve was obtained in the case of Na-SWy-2, which is due to the elimination of organic matter and calcite after purification which is in agreement with the XRD results. In both samples the TG curves show two steps for mass loss corresponding to dehydration and dehydroxylation reactions.

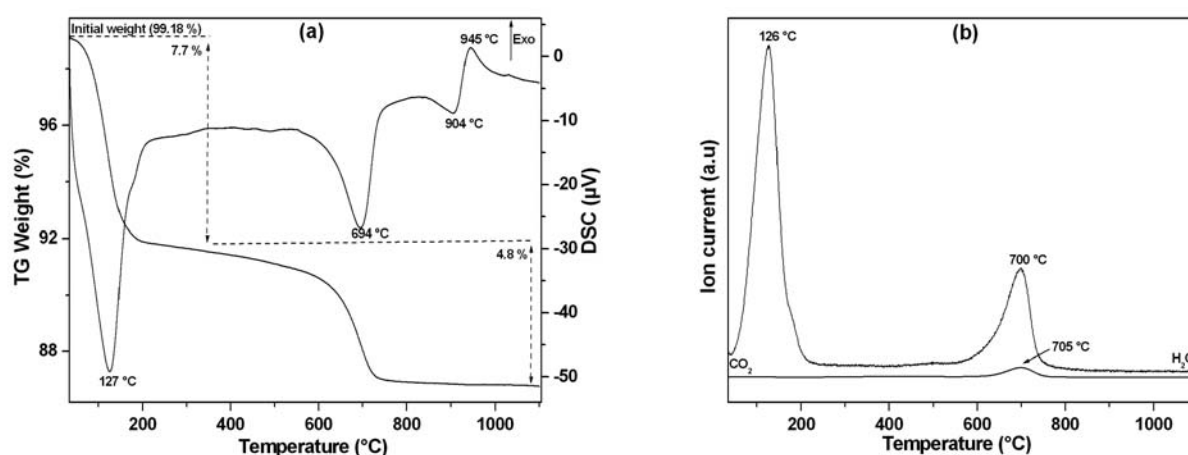


Figure 1.5: Simultaneous thermal analysis of SWy-2, (a) TG/DTA, (b) MS (H₂O and CO₂).

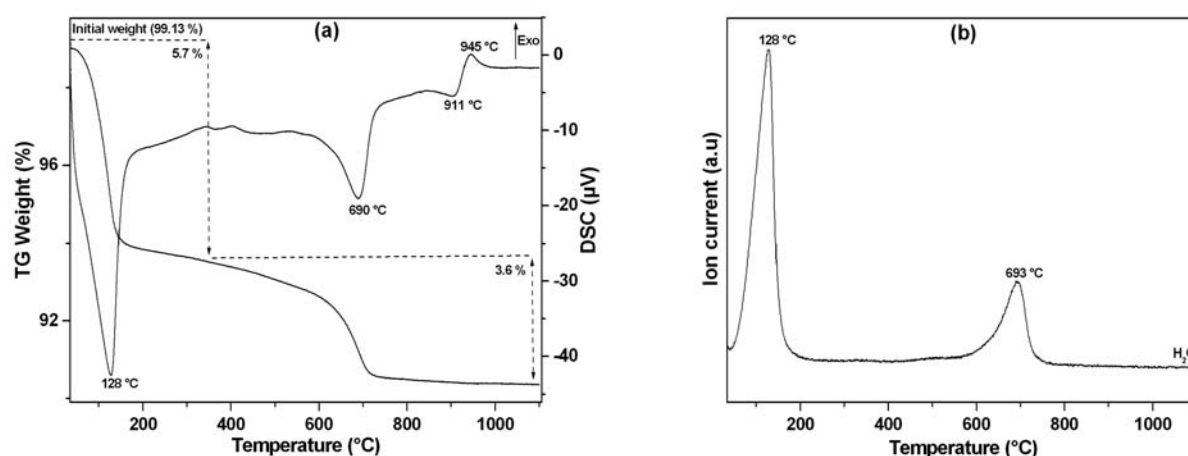


Figure 1.6: Simultaneous thermal analysis of Na-SWy-2, (a) TG/DTA, (b) MS (H₂O).

1.5.7. Magnetic properties

The montmorillonite is one of the iron bearing minerals. It exhibits a paramagnetic behaviour with a susceptibility of 13 in units of $10^{-8} \text{ m}^3/\text{kg}$ (Moskowitz, 1991). A study of the magnetic properties of oxidized and reduced smectites has been established by Schuette *et al.*, (2000). They showed that the low-Fe specimen (montmorillonite) was paramagnetic in both oxidized and reduced states and the Fe is essentially randomly distributed through the structure and is not concentrated in localized Fe-rich regions.

1.6. Optimisation of synthesis parameters

It is useful to mention again that the term of the intercalated clay as defined in IUPAC report (Schoonheydt *et al.*, 1999) indicates the exchanged clay, while the term of the pillared clay defines the calcined intercalated clay. In this part, the influence of some synthesis parameters of aluminium and zirconium pillared clays are presented. The materials obtained have been investigated by XRD and N₂ adsorption.

Al pillared clays

Results obtained from N₂ adsorption and XRD are listed in Tab. 1.7, the corresponding diffractograms are illustrated in Fig. 1.7. The main observation that can be first taken from the adsorption and XRD data is that, in all samples, the intercalation process was successful.

The basal spacing remains constant for most of the samples. It is important to note that in all preparations the OH/Al molar ratio was the same.

A study of the influence of ageing time was carried out in Al pillared Algerian montmorillonites by Khalaf *et al.*, (1997). They reported that the pillared products, obtained with the Al-solution aged only for a period of two hours, are thermally unstable even at 105 °C. An ageing time of 48 h led to the formation of stable materials even after calcination at 500 °C. This fact corresponds to the intercalation of aluminium polycations with 13 Al ions known as Keggin structure described by Johansson in 1960.

For the second set of experiments, and in order to reduce the time, 24 h ageing time was used instead 48 h, the obtained solution still has Al₁₃-Keggin cation structure justified by the increase of basal spacing and SSA (Tab. 1.7). In these experiments, the intercalation time is increased to 17 h from 4 h in order to allow the aluminium species to diffuse into the clay particles. With increasing aluminium concentration, the specific surface areas and pore volume were increased, more pronounced for 10 mmol/g. For the same condition, the surface area and porosity decrease with increasing aluminium concentration. In the case of intercalated clay Al-3-60, the decrease of surface area and pore volume is due to the decrease in the corresponding micropore volume. A high amount of Al added in the pillaring procedure could negatively affect the physicochemical and textural characteristics of the resulting pillared clays. This fact has been ascribed to the intercalation of different species between the clay layers of different sizes as reported previously (Valverde *et al.*, 2003). Finally, an ageing period of 24 h of the Al pillaring solution with an OH/Al= 2 together with an Al to clay ratio of 10 mmol/g were the best conditions for further investigations (Chapter 3).

Table 1.7: Basal spacing, specific surface area, and pore volume of differently prepared Al pillared clays.

Samples	d_{001} (Å)	SSA (m^2/g)	V_{mp} (cm^3/g)	V_{mes} (cm^3/g)	V_p (cm^3/g)
Al-1-60	19.0	172	0.052	0.038	0.090
Al-1-500	17.2	123	0.034	0.033	0.067
Al-2-60	18.4	243	0.086	0.029	0.115
Al-2-500	16.7	180	0.043	0.061	0.104
Al-3-60	18.7	202	0.073	0.021	0.094
Al-3-500	17.0	111	0.033	0.027	0.060

SSA: specific surface area, V_p : pore volume at $P/P_0 = 0.7$ (pore width ≤ 7 nm), V_{mp} : micropore volume, V_{mes} : mesopore volume.

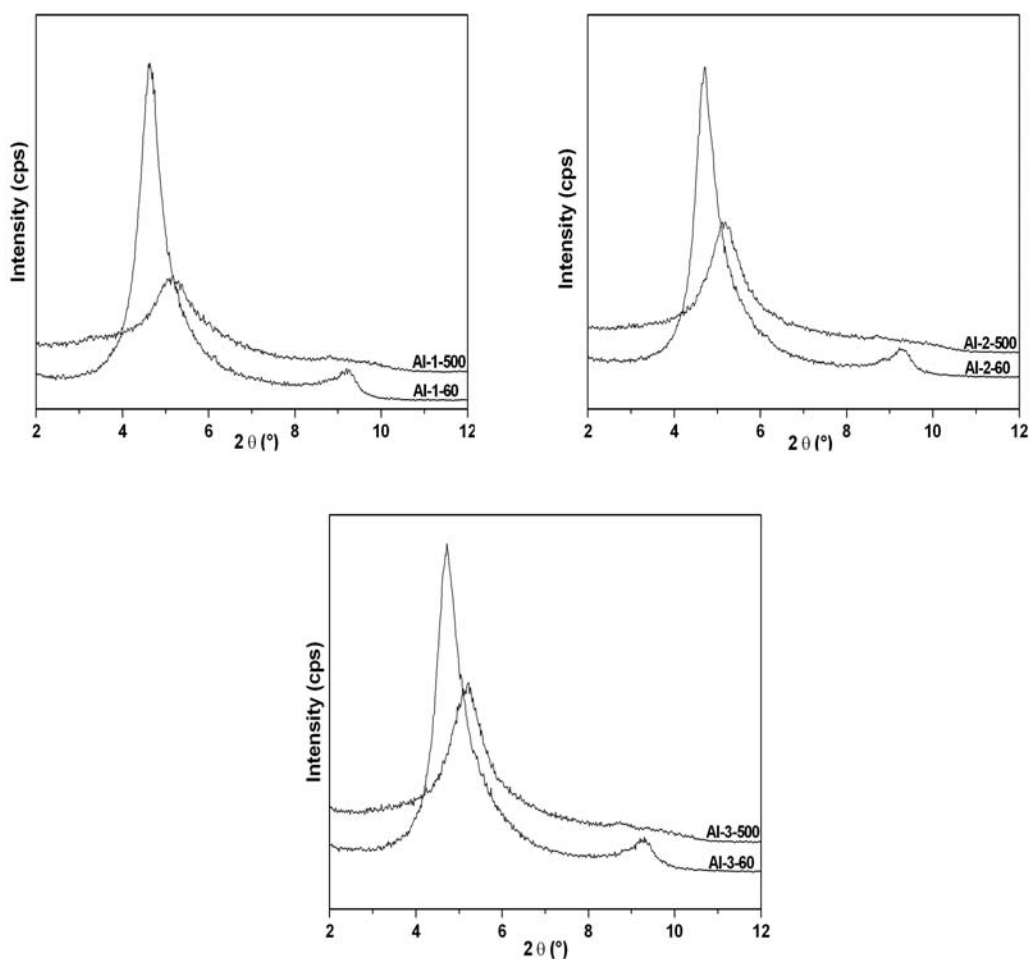


Figure 1.7: Oriented X-ray diffractograms of aluminium pillared clay dried at 60 °C and calcined at 500 °C.

Zr pillared clays

Compared to Al-pillaring, the Zr-pillaring of clays is less well investigated and documented in the literature. For Zr pillared clays intercalated species are not well identified. In this part two preparations have been manufactured, in which the Zr intercalated solution was used after ageing and without ageing. The intercalated materials and the corresponding calcined one have been characterized by XRD and N₂ adsorption (Tab. 1.8 and Fig. 1.8). An increase of basal spacing as well as the specific surface area and pore volume was obtained. For the samples with freshly made Zr solution the SSA and V_p are higher than for the samples made from aged solution. Thus, for further investigation, a freshly made zirconium solution was used together with a Zr to clay ratio of 10 mmol/g (Chapter 4).

Table 1.8: Basal spacing, specific surface area, and pore volume of different prepared Zr pillared clays.

Samples	d ₀₀₁ (Å)	SSA (m ² /g)	V _{mp} (cm ³ /g)	V _{mes} (cm ³ /g)	V _p (cm ³ /g)
Zr-1-60	18.5	132	0.035	0.039	0.074
Zr-1-500	15.0	80	0.015	0.035	0.050
Zr-2-60	18.4	201	0.066	0.031	0.097
Zr-2-500	15.1	105	0.022	0.041	0.063

SSA: specific surface area, V_p: pore volume at P/P₀ = 0.7 (pore width ≤ 7 nm), V_{mp}: micropore volume, V_{mes}: mesopore volume.

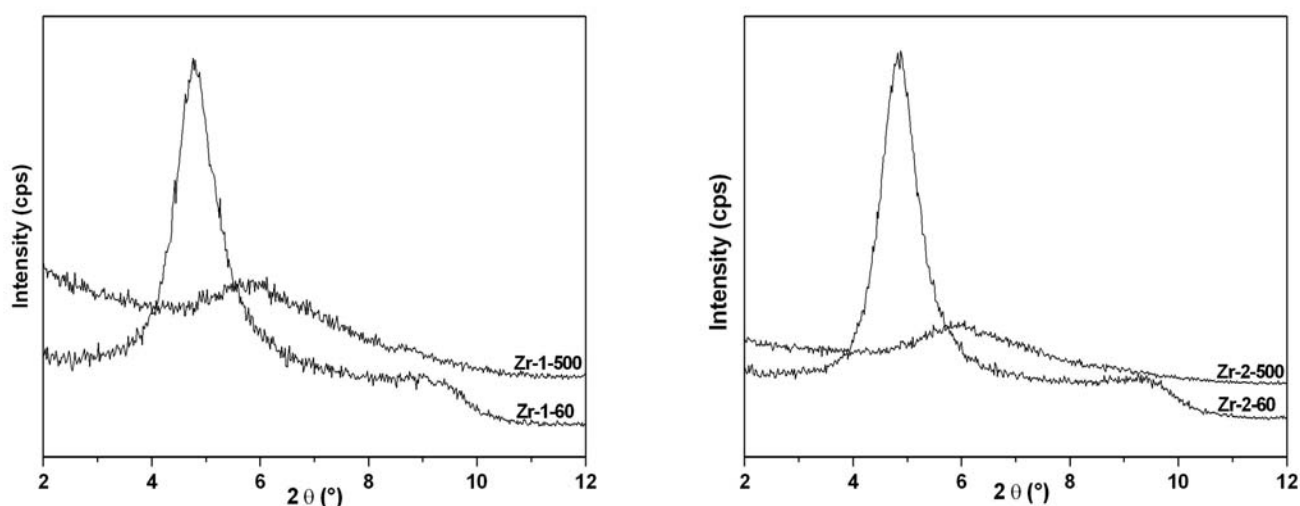


Figure 1.8: Oriented X-ray diffractograms of zirconium pillared clay dried at 60 °C and calcined at 500 °C.

1.7. Calculation of the filling factor of pillared clays

The structure of pillared clays depends on many factors. The most important are the pillar nature, the pillar size, the amount of the pillars and their distribution between the TOT layers. On the basis of a simple geometric model and experimental data it is possible to calculate, to a certain extent, the filling factors. Using this factor, the pillared structure can be estimated. The calculation has been done for Ti-PILCs, Al-PILCs, Zr-PILCs, as well as their magnetic forms.

Two approaches were used to determine the filling factor. A first approach is focused on the computation of the theoretical interlayer volume $V_{IL,the}$, taking into account the unit cell parameters of Na-SWy-2 and the interlayer spacing d_{IN} deduced from d_{001} basal spacing of the corresponding pillared clays. The second approach is based on the calculation of the pillar volume V_{PL} using the pillar density and the additional pillar content normalised to the Na-SWy-2 content. The obtained V_{PL} was added to the pore volume V_p at $P/P_0 = 0.7$ (pore width ≤ 7 nm) to obtain the required experimental interlayer volume, $V_{IL,exp}$.

The filling factor FF is given by:

$$FF = V_{IL,exp} / V_{IL,the} \quad (8)$$

With $V_{IL,the}$, based on the unit cell formula of Na-SWy-2, defined as:

$$V_{IL,the} = (d_{IN} * a * b) * N_{av} / M \quad (9)$$

where:

d_{IN} : is the interlayer space ($d_{IN} = d_{001} - t$, t : is the TOT layer thickness (Fig. 1.9)).

a , b : the unit cell dimensions of 5.15 Å and 8.98 Å, respectively (Fig. 1.10).

N_{av} : Avogadro number ($6.023 * 10^{23}$).

M : molecular weight of Na-SWy-2.

and $V_{IL,exp}$ defined as:

$$V_{IL,exp} = V_{PL} + V_p \quad (10)$$

where:

V_{PL} : the pillar volume.

V_p : the pore volume at $P/P_0 = 0.7$ (pore width ≤ 7 nm).

The corresponding intercalation factor can be also deduced from the FF factor as follows:

$$IF = 1/FF \quad (11)$$

The filling factor contains information on the number of intercalated pillared TOT-layers and the unaffected TOT-layers. From data presented in this work and from literature, the existence of non-intercalated layers must be assumed. As this work will show, the distribution of the PILC-layers is important for the magnetic properties. Moreover, this work combines structural data from XRD, XRF, and porosity data in one PILC-model.

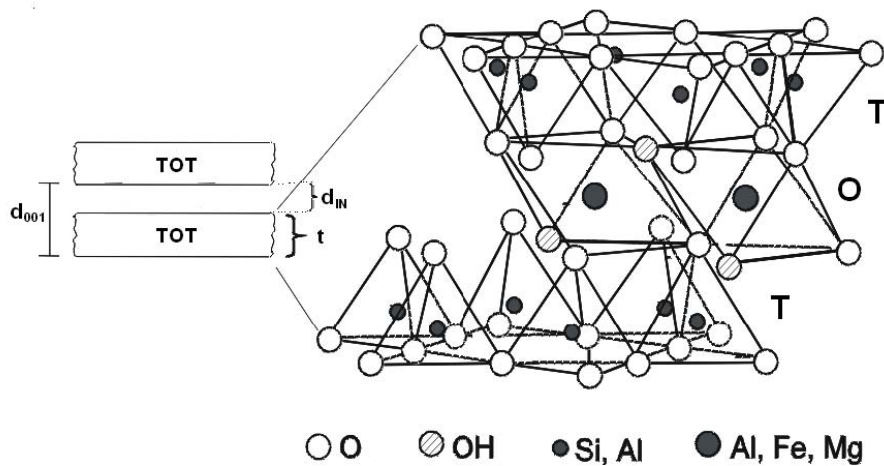


Figure 1.9: TOT layer of montmorillonite.

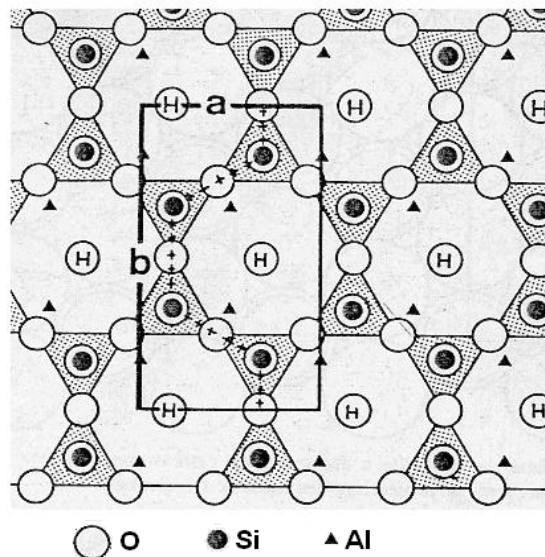


Figure 1.10: Top view of the TOT layer showing the hexagonal cavities.

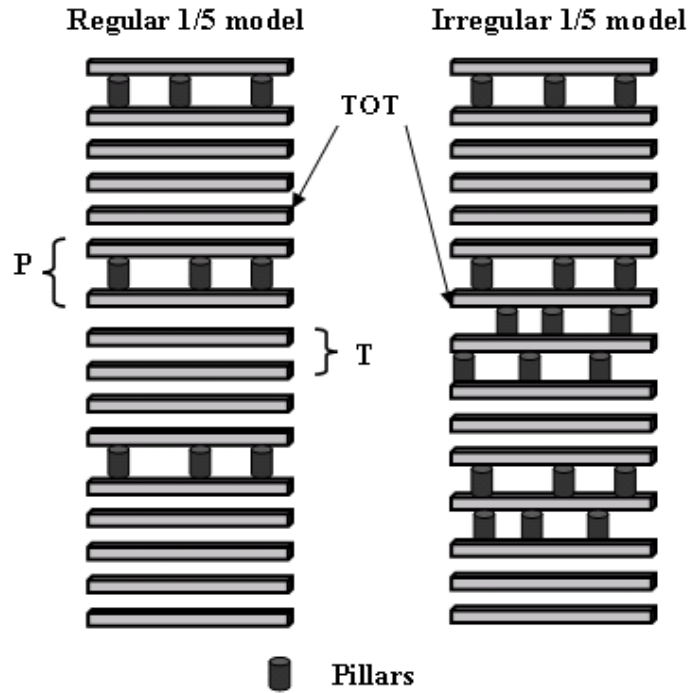


Figure 1.11: 1/5 pillared structure model.

Fig. 1.11 presents an example of pillared structure with $FF = 1/5$. Let's first define $T = \text{TOT}$ layer, $P = \text{PILC-layer}$. In this example $1/5$ means that, in five layers, there is one layer P filled with pillars. Hence, the model shown left is a regular $1/5$ model: PTTTTPTTTTPTTTT . The irregular one where the TOT stacking is irregular is shown in the right model: PTTTTPPTTPPTT . Beside the regular and irregular model, there can be, in addition, a regular and/or irregular pattern of the PILCs in its layer.

2. Magnetic titanium pillared clays (Ti-M-PILCs)

Ti-PILCs were prepared according to the method of Sterte (1986). TiCl_4 was hydrolysed in 6 M HCl and diluted with water to a final concentration of $[\text{Ti}^{4+}] = 0.82$ M. This solution was aged for 3 h before mixing with a 0.4 % Na-SWy-2 suspension in a ratio of 10 mmol Ti^{4+} /g clay. After 16 h of exchange, the intercalated clay was centrifuged, washed free of chloride and dried at 60 °C. Ti-PILCs were finally obtained by calcination of the intercalated material at 200-600 °C for 3 h in air.

Magnetic titanium pillared clays (Ti-M-PILCs) have been produced, thereafter, by sodium borohydride reduction of ferrous ions added by ion-exchange to titanium pillared montmorillonite (Ti-PILCs) at room temperature. An initial investigation using several methods was mandatory to check the textural properties and the thermal stability of Ti pillared clays upon heat treatment. The textural properties of the magnetic form Ti-M-PILCs were also investigated. In addition to XRD and N_2 sorption, the properties of the obtained Ti-M-PILCs have been investigated using superconducting quantum interference devices (SQUID) and Mössbauer spectroscopy. Hysteresis, zero field cooled (ZFC) and field cooled (FC) measurements have been performed on different precursor materials prepared by calcination of Ti-PILCs at temperatures between 200 and 600 °C. The original titanium pillared samples are designated in the text below as Ti-PILC followed by the corresponding calcination temperature (Ti-PILC-Temperature in °C). For the magnetic pillared samples the notation Ti-M-PILC-Temperature is used (M stands for magnetic).

In this chapter, the influence of the calcination temperature of the starting Ti-PILCs on structural and magnetic properties of Ti-M-PILCs is discussed. The results obtained suggest the presence of two different Fe-alloy distributions, a dispersed one for the lower calcined Ti-PILCs, and clusters for the higher calcined ones (Bachir *et al.*, 2009).

2.1. Titanium pillared clays

2.1.1. XRD investigation

The pillaring process is characterized by the evolution of the diffraction line (001) and the textural properties. Fig. 2.1a shows the oriented XRD patterns of the obtained titanium pillared montmorillonite calcined at various temperatures. For all samples except Ti-PILC-600 an increase of d_{001} is observed, which is justified by the insertion of the titanium pillars into the interlayer space (Tab. 2.1).

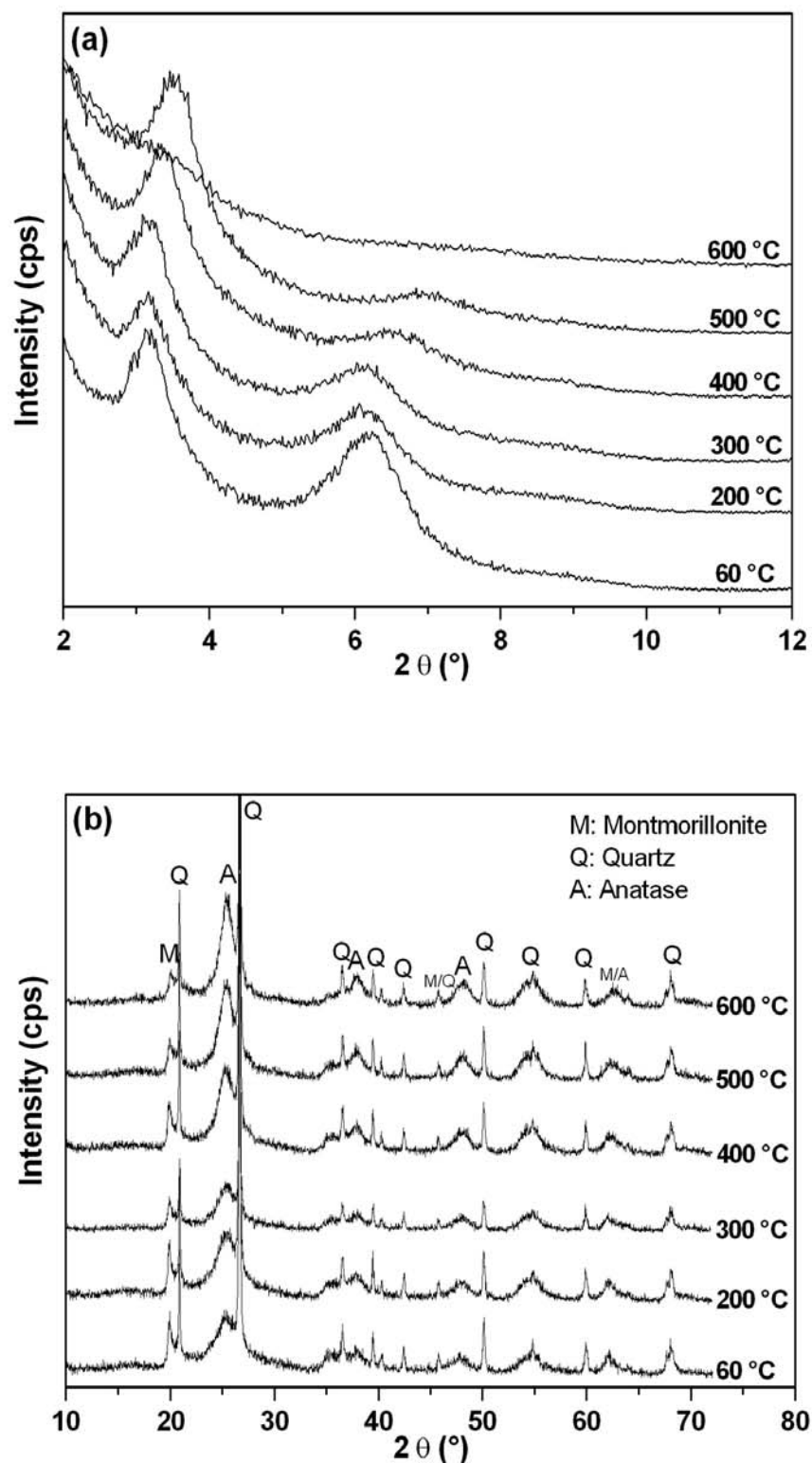


Figure 2.1: a) Oriented X-ray diffractograms of titanium pillared clay dried at 60 °C and calcined at various temperatures and b) Powder X-Ray diffractograms of Ti-PILCs.

Table 2.1: d_{001} values of Ti-PILCs.

Samples	d_{001} (nm)
Ti-PILC-60	2.80
Ti-PILC-200	2.80
Ti-PILC-300	2.80
Ti-PILC-400	2.65
Ti-PILC-500	2.50
Ti-PILC-600	n.p

n.p: not present.

A constant d-value of 2.80 nm is found for Ti-PILC-60, -200, and -300. At higher temperature, the d-value decreased with increasing calcination temperature from 2.65 nm for Ti-PILC-400 to 2.50 nm for Ti-PILC-500. A second peak at around $6^\circ 2\theta$ decreases in intensity upon increasing calcination temperature. The presence of this peak can be interpreted by the diffraction line (002) of Ti-PILCs. The pillared clay structure, though, is not completely affected after calcination at 600 °C; the powder diffractogram still reveals peaks attributable to montmorillonite, besides quartz and anatase (Fig. 2.1b). The powder XRD patterns of Ti-PILCs show also that the intensity of (101), the strongest peak ($d= 0.35$ nm and $2\theta= 25.35^\circ$) of anatase, increases with the increase of calcination temperature. This comparison in intensity was carried out qualitatively after normalisation to the intensities relative to the quartz peak. This finding reflects the growth of the crystalline grains of anatase with calcination temperature.

The crystal size, D , of the anatase can be estimated from Fig. 2.1b by the Scherrer equation (Jenkins and Vries, 1970):

$$D = k\lambda/\beta \cos \theta \quad (1)$$

where k is the shape factor with the value of 0.9, λ is the wavelength used, β is the line broadening which is the width of the diffraction line at its half intensity maximum, and θ is the diffraction angle. As given in Tab. 2.1, the calculation shows that the full width at half maximum β decreases at high temperature, therefore anatase crystallinity is higher at higher calcination temperature and therefore the D values of the anatase crystalline grain increase with the increment of calcination temperature.

2. Magnetic titanium pillared clays (Ti-M-PILCs)

Table 2.2: D and β values of anatase for Ti-PILCs

Sample	Ti-PILC-60	Ti-PILC-200	Ti-PILC-300	Ti-PILC-400	Ti-PILC-500	Ti-PILC-600
β	1.457	1.553	1.365	1.389	1.318	1.180
D (nm)	6.2	5.8	6.6	6.5	6.9	7.7

2.1.2. N₂ gas adsorption

SSA and porosity

Results obtained from N₂ adsorption analysis (Tab. 2.3) show that SSA are in the range of 200-300 m²/g and indicate a successful pillaring process. On one hand, heating up to 600 °C transformed the polycations into oxide pillars and had no strong impact on the SSA indicating a good thermal stability of the Ti-PILCs clay. On the other hand, an increase of the adsorbed volume, more pronounced in the mesopore range, has been obtained (Tab. 2.3). Thus Ti-PILCs exhibit both micro and mesoporosity, the mesoporosity is more accentuated.

Table 2.3: Specific surface areas and pore volumes of Ti-PILCs.

Samples	SSA (m ² /g)	V _{mp} (cm ³ /g)	V _{mes} (cm ³ /g)	V _p (cm ³ /g)
Ti-PILC-60	281	0.025	0.143	0.168
Ti-PILC-200	280	0.017	0.154	0.171
Ti-PILC-300	268	0.008	0.161	0.169
Ti-PILC-400	262	0.010	0.151	0.161
Ti-PILC-500	244	0.005	0.154	0.159
Ti-PILC-600	231	0.008	0.145	0.153

SSA: specific surface area, V_p: pore volume at P/P₀ = 0.7 (pore width ≤ 7 nm), V_{mp}: micropore volume, V_{mes}: mesopore volume.

Pore size distribution

Fig. 2.2 shows the NLDFT cumulative pore volume and the corresponding differential pore volume distribution curves of Ti-PILCs. For samples Ti-PILC-60 and Ti-PILC-200, the distribution presents two maxima: one at about 1.4 nm (microporous range), and the other peak, broader and with low intensity value at about 2.57-3.06 nm (mesoporous range). The corresponding cumulative pore volume shows two steps, each associated with one of the two pore distribution maxima. For the samples Ti-PILC-300, Ti-PILC-400, Ti-PILC-500, and Ti-

2. Magnetic titanium pillared clays (Ti-M-PILCs)

PILC-600, the pore volume distribution presents also two peaks, peak at about 1.4-1.5 nm and another peak, broader and with high intensity value at about 2.57-3.16 nm.

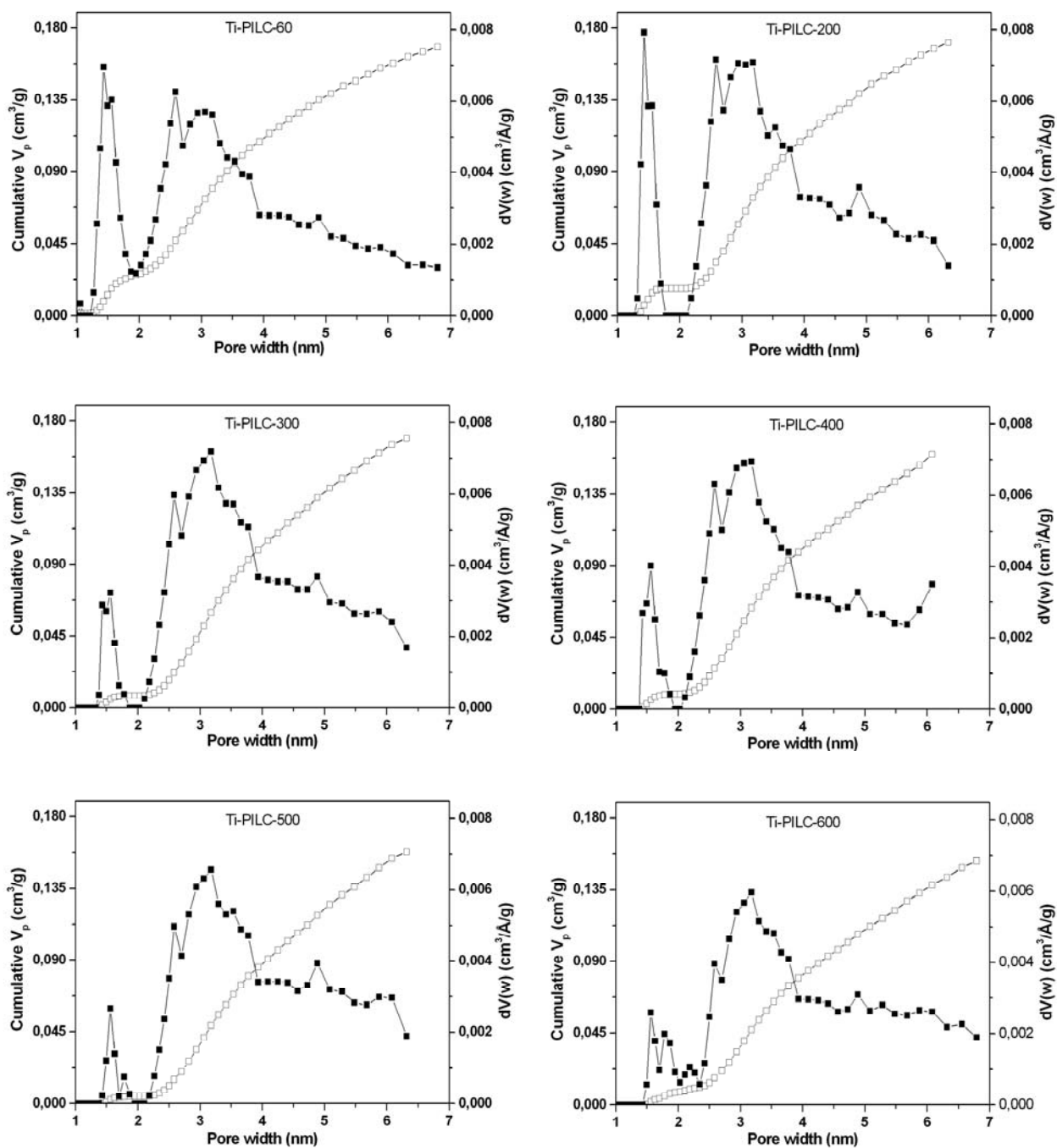


Figure 2.2: Pore size distribution of Ti-PILCs. Full symbols/ right y-axis: differential pore volume distribution curves, open symbols/ left y-axis: cumulative pore volume.

N₂ isotherms

The N₂ isotherms of Ti-PILCs compared with the Na-SWy-2, with linear and logarithmic relative pressure axis, are illustrated in Fig. 2.3. An increase of the adsorbed volume was obtained for all Ti-PILCs comparing with the original clay, at $P/P_0 < 0.1$, this increase is better seen when the isotherms are represented in the logarithmic scale. The isotherm shapes of Ti-PILCs correspond to type IV (Sing *et al.*, 1985, Lowell *et al.* 2006).

This isotherm type is characteristic of mesoporous materials. However, in the zone of low relative pressure values, Ti-PILCs present type I isotherm, which indicate the presence of micropores. The presence of a hysteresis loop in all of the isotherms indicates also some degree of mesoporosity. In the case of the original clay, the mesoporosity is inherent in the clay itself and arises by stacking defects (Hutson, 1999), as shown by the hysteresis loop seen in the adsorption isotherm of the unpillared clay. These stacking defects are the result of the attraction between negatively charged basal surfaces and positively charged crystal edges (Van Olphen, H., 1963).

In the case of Ti-PILCs, according to Maes *et al.* (1997), it is possible that a proportion of the TiO₂ particles do not penetrate in the layer and they are deposited as a TiO₂ phase on the external surface of the clay layers. This coating could bring about a large amount of mesopores in the pillared material besides micropores created by the pillaring process.

The hysteresis loop corresponds to type H4 in the International Union of Pure and Applied Chemistry (IUPAC) classification and this is characteristic of material with narrow slit-like pores.

All these results indicate that the obtained materials have both micro- and mesoporosity as confirmed by the pore size distribution and pore volume determination. However, the mesoporosity is dominant.

2. Magnetic titanium pillared clays (Ti-M-PILCs)

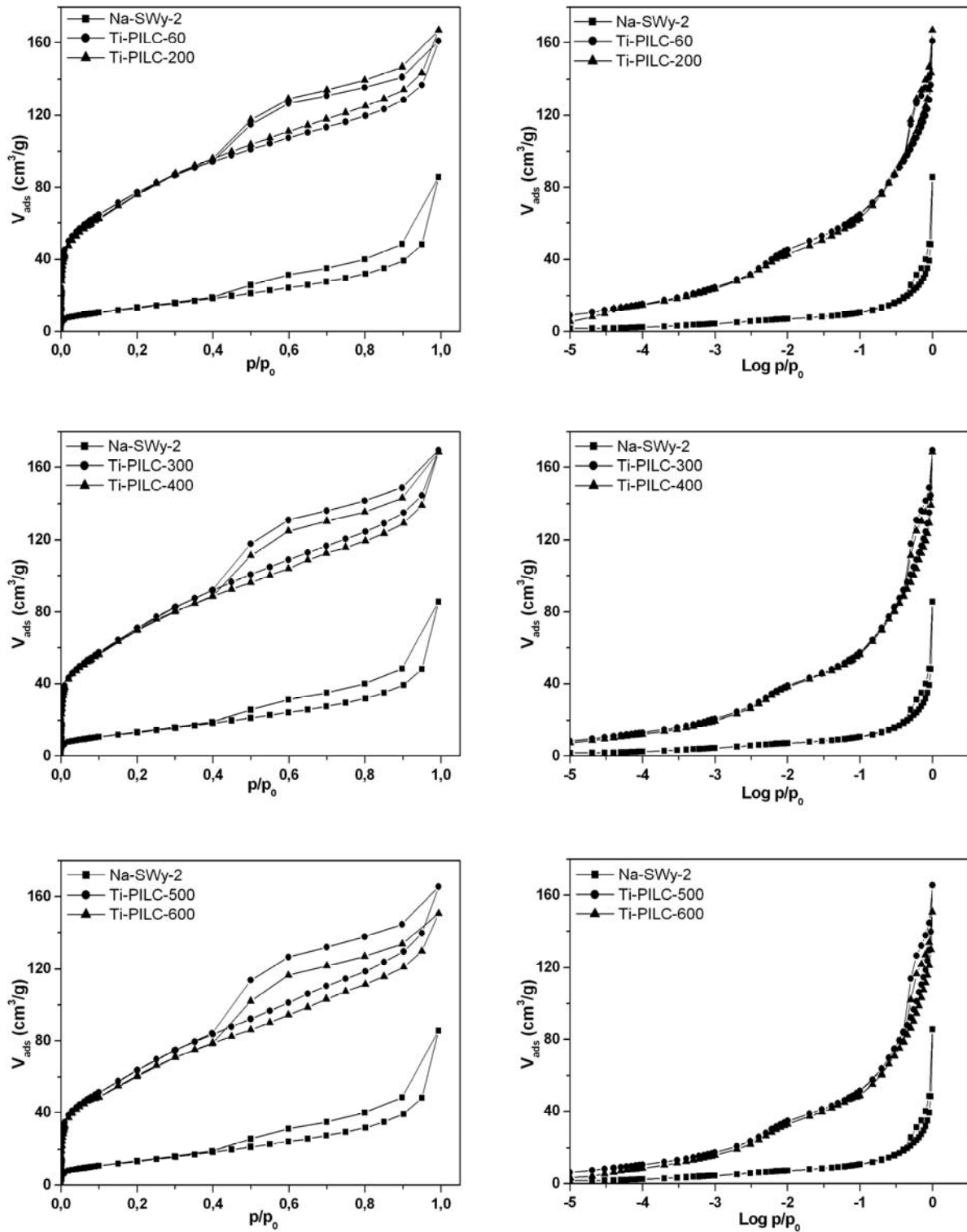


Figure 2.3: N_2 adsorption-desorption isotherms of Ti-PILCs

2. Magnetic titanium pillared clays (Ti-M-PILCs)

2.1.3. X-ray fluorescence XRF

XRF fluorescence was performed to determine the chemical composition of the obtained titanium pillared clays. The results are reported in Tab. 2.4. A higher content of TiO₂, resulting from pillaring, reflects Ti incorporation into the clay, this content is fairly constant for all samples. The oxide content related to the interlayer exchangeable cations is decreased, essentially all the sodium ions were exchanged with titanium species. The LOI, which is related to the volatile materials lost, usually water, decreases with increase in heat treatment.

Table 2.4: Chemical composition reported as oxides (%wt.) of Na-SWy-2 and Ti-PILCs.

Oxides	Na-SWy-2	Ti-PILC-60	Ti-PILC-200	Ti-PILC-300	Ti-PILC-400	Ti-PILC-500	Ti-PILC-600
SiO ₂	60.42	41.65	44.03	44.63	45.38	44.87	46.77
Al ₂ O ₃	19.79	7.48	7.91	8.05	8.20	8.07	8.37
Fe ₂ O ₃	3.99	1.71	1.69	1.72	1.68	1.80	1.80
MnO	0.01	0.00	0.01	0.01	0.01	0.00	0.00
MgO	2.34	0.75	0.79	0.81	0.81	0.81	0.84
CaO	0.13	0.12	0.13	0.13	0.13	0.14	0.13
Na ₂ O	2.21	b.d	b.d	b.d	b.d	b.d	b.d
K ₂ O	0.11	0.22	0.23	0.24	0.24	0.24	0.25
TiO ₂	0.11	34.08	36.02	36.59	37.12	36.70	38.16
P ₂ O ₅	0.02	0.04	0.04	0.04	0.04	0.04	0.04
SO ₃	0.02	b.d	b.d	b.d	b.d	b.d	b.d
LOI	10.85	13.90	9.10	7.73	6.33	7.27	3.58

b.d: below detection limit.

2.1.4. Simultaneous thermal analysis

As inferred from LOI, the water content of titanium pillared clays obtained at different temperatures is decreasing with increasing calcination temperature, the same behaviour is obtained from TG curves of Ti-PILCs (Tab. 2.5). This can be explained on the basis of the partial loss of the swelling properties of the clay and hence the lower water retention capacity upon heat treatment (Mishra and Rao, 2004). The total weight loss of Ti-PILCs is greater than that of the original clay. This difference is well pronounced in the first interval of Ti-PILCs/TG curves (36-350 °C) which is due to the loss of both physically adsorbed water and the dehydration of the chemical species those form the pillars.

DTA curves in Fig 2.4 of Ti-PILCs products show one endothermic peak near 120-130 °C induced by dehydration besides one small endothermic peak at about 600 °C assigned to dehydroxylation of both the clay structure and the titanium pillars. The dehydroxylation

2. Magnetic titanium pillared clays (Ti-M-PILCs)

temperature of this peak decreases for Ti-PILC-600. This fact shows that Ti-PILCs are less thermally stable at 600 °C, which is in agreement with the XRD results.

Other observed behaviour is that the dehydroxylation temperature of Ti-PILCs is lower than that of Na-SWy-2. Similar observations were reported by Han and Yamanaka 1998 and 1997; the dehydroxylation in a low temperature range was explained in terms of the condensation of the structural hydroxyl groups with Ti pillars.

An exothermic peak at about 960 °C is assigned to the recrystallisation of Ti-PILCs.

Table 2.5: STA results of Ti-PILCs and Na-SWy-2.

Samples	Dehydration temperature (°C)	Dehydroxylation temperature (°C)	Recrystallisation temperature (°C)	Total water Content (%)
Na-SWy-2	128	690	945	9.3
Ti-PILC-60	135	584	963	18.9
Ti-PILC-200	130	580	963	16.3
Ti-PILC-300	128	584	964	14.6
Ti-PILC-400	123	598	966	12.4
Ti-PILC-500	120	627	965	10.4
Ti-PILC-600	118	447	965	9.4

2. Magnetic titanium pillared clays (Ti-M-PILCs)

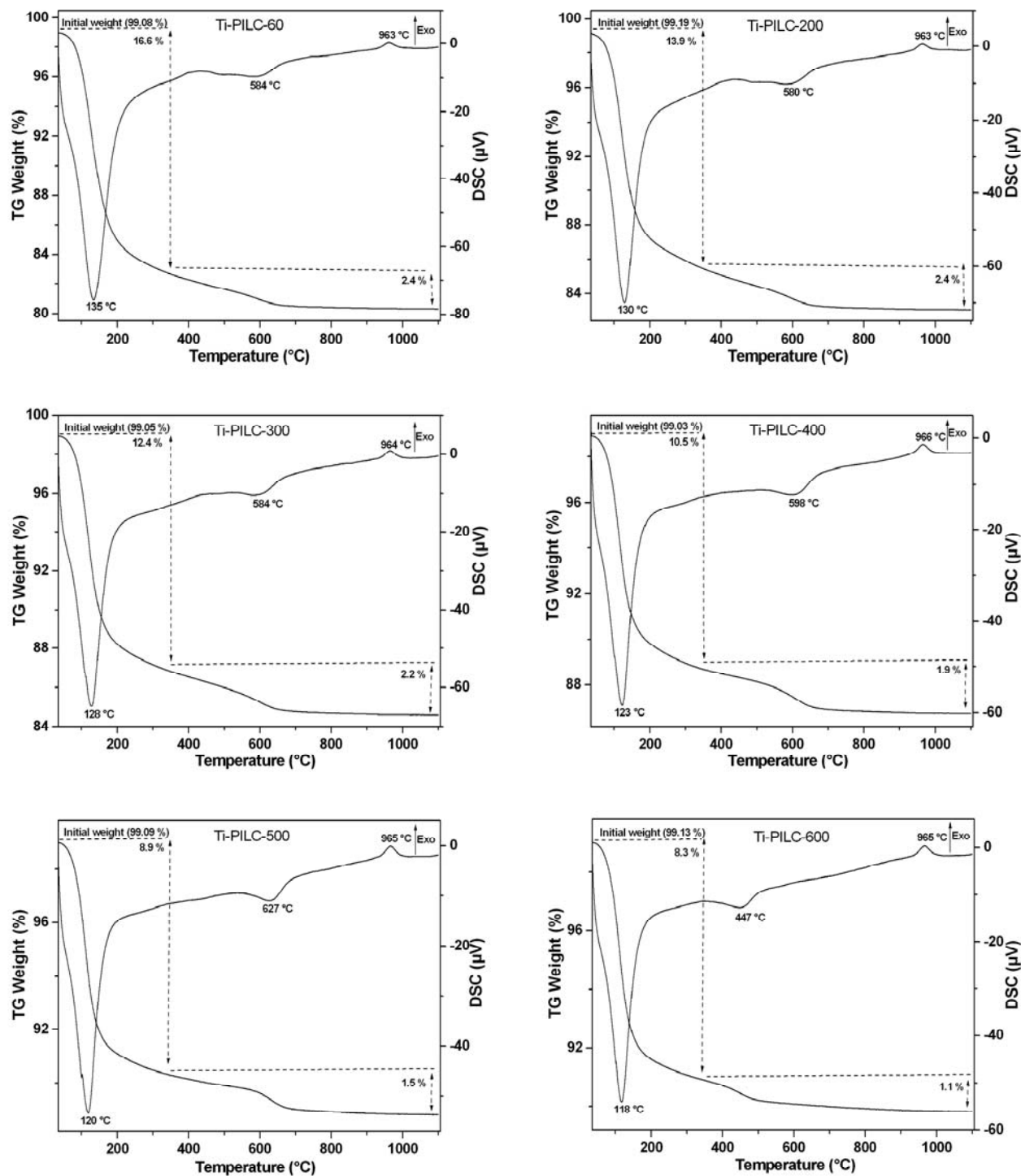


Figure 2.4: STA curves of Ti-PILCs

2.1.5. Cation exchange capacity

The cation exchange capacity CEC of Ti-PILCs was also determined with copper-triethylenetetramine exchange according to Meier and Kahr (1999), in order to see the influence of the pillaring process as well as the calcination temperature effect.

2. Magnetic titanium pillared clays (Ti-M-PILCs)

In order to find the CEC value in 100 g of the dried sample, water content related to the dehydration was also calculated from the STA measurements using TG curves (Tab. 2.6).

The low values of CEC after pillaring (Tab. 2.6) suggest the irreversibility of cationic exchange; the intercalated titanium polycations were hardly exchanged. Thus, CEC represents only the exchange of the residual interlayer cations mostly Na^+ , K^+ , Ca^{2+} , and Mg^{2+} . These suggestions are supported by the determination of the exchanged cations and titanium in the supernatant solution after copper-triethylenetetramine exchange using ICP-OES measurements. The obtained data show that no titanium content was found; only low CEC values of Na^+ , K^+ , and Mg^{2+} are obtained. Yamanaka and Brindley, (1979) explain that by the contribution of protons associated with polycations to the total CEC of pillared clays.

Another reason is the influence of pH, as shown in Tab. 2.6, the pH of CEC measurement of Ti-PILCs is less than that of the unpillared clay. This is due to the titanium pillaring solution obtained previously by the hydrolysis of TiCl_4 in HCl medium which exhibits a low pH (pH < 1). According to Peigneur *et al.*, 1975, Lagaly, (1981), and Jasmund and Lagaly, (1993), at low pH, the edges are positively charged, thus edge charge does not contribute to the measured CEC, which is the case for Ti-PILCs. However, Na-SWy-2 (pH= 8.1) exhibits exchange capacity of both the interlayer and the edge. For many smectites the interlayer CEC is about 80 % of the total CEC; 20% of the CEC results from cations at crystal edges (Vogt and Köster, 1978).

Table 2.6: CEC and water content of Ti-PILCs

Samples	CEC (meq/100 g)	CEC reduction (%)	Water content* (%)	pH
Na-SWy-2	85		5.7	8.1
Ti-PILC-60	30	65	16.6	4.4
Ti-PILC-200	25	71	13.9	4.6
Ti-PILC-300	23	73	12.4	4.5
Ti-PILC-400	15	82	10.5	4.5
Ti-PILC-500	13	85	8.9	4.7
Ti-PILC-600	12	86	8.3	5.0

*: The water content at 35-350 °C determined from TG curves.

2. Magnetic titanium pillared clays (Ti-M-PILCs)

The decrease of CEC with increasing calcination temperature is also related to the dehydration of titanium pillars at 35-350 °C. In this range, the water content decreases with increasing heat treatment. According to Hoffman and Klemen, (1950), it is known that the CEC decreases with increasing temperature, because small exchangeable cations like Li^+ and Cu^{2+} move into the structure.

In the case of pillared clays, the calcination step converts the polyoxycation precursors into rigid oxide pillars. During calcination, dehydration and dehydroxylation reactions of the charged pillar precursor occur to give neutral oxide particles. The equilibrium in electrical charge is maintained by the release of protons at elevated temperatures (Cool and Vansant, 1998):



Since all conditions of the Hoffman-Klemen effect are fulfilled (small exchangeable cations H^+ and heating), the liberated protons H^+ will migrate into the empty octahedral positions of the dioctahedral montmorillonite SWy-2. Therefore, the protons move into the interlayer space of the PILCs and are not available for further ion exchange. Thus a decrease of CEC of PILCs with increase in calcination temperature was observed.

2.2. Magnetic titanium pillared clays

2.2.1. XRD investigation

After the insertion of the iron and the subsequent reduction by NaBH_4 the interlayer spacing reduced to values of 1.70 nm for the samples Ti-M-PILC-60 and -200, 1.57 nm for Ti-M-PILC-300 and -400 and 1.37 nm for the sample Ti-M-PILC-500 (Fig. 2.5a and Tab. 2.7). Furthermore, the powder diffractograms (Fig. 2.5b), do not contain new peaks attributable to iron compounds.

Table 2.7: d_{001} values of Ti-M-PILCs

Samples	d_{001} (nm)
Ti-M-PILC-60	1.70
Ti-M-PILC-200	1.70
Ti-M-PILC-300	1.57
Ti-M-PILC-400	1.57
Ti-M-PILC-500	1.37
Ti-M-PILC-600	n.p.

n.p.: not present

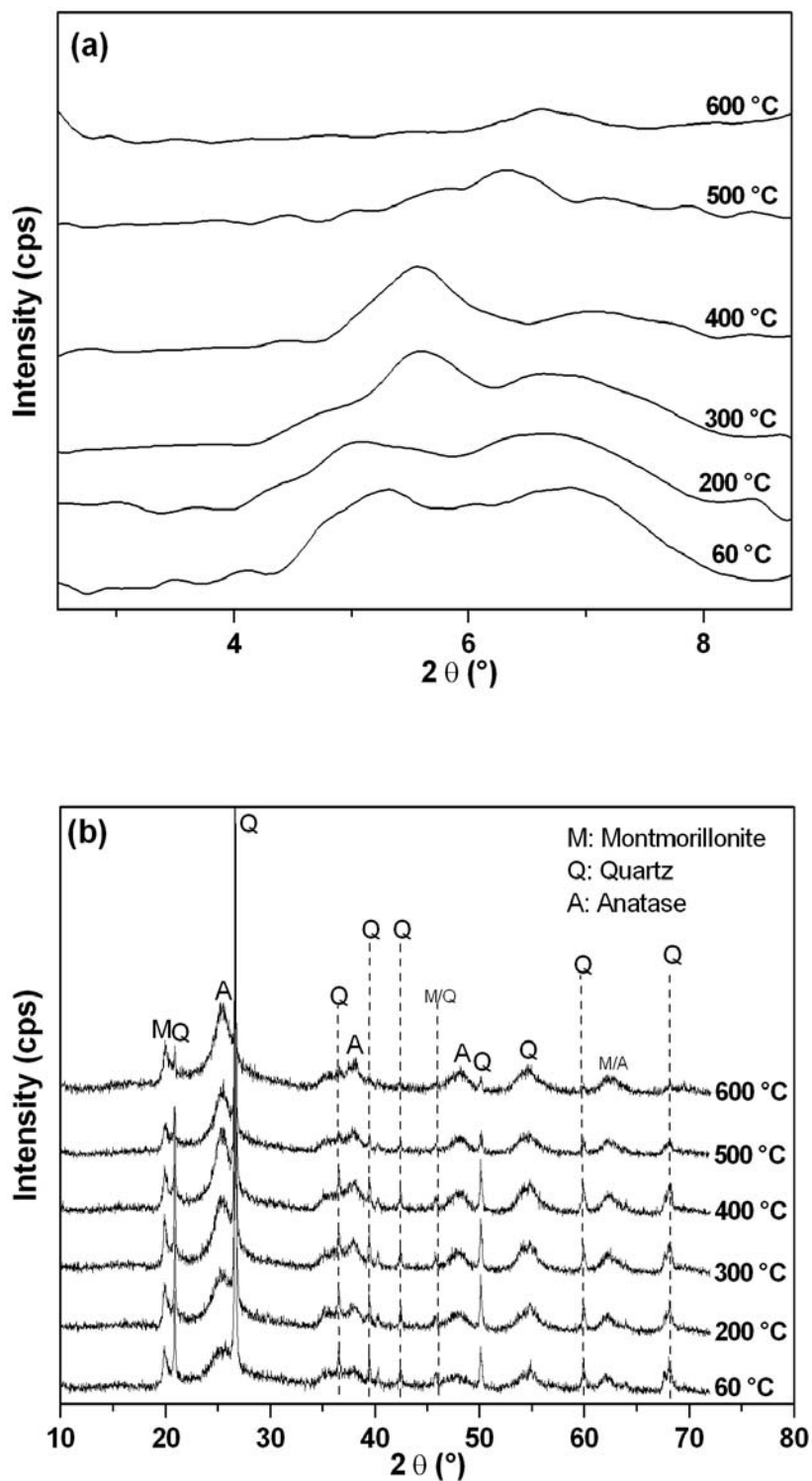


Figure 2.5: a) Oriented X-ray diffractograms of titanium magnetic pillared clay and b) Powder X-Ray diffractograms of Ti-M-PILCs.

2. Magnetic titanium pillared clays (Ti-M-PILCs)

2.2.2. N₂ gas adsorption

SSA and Porosity

After Fe exchange and NaBH₄ reduction (magnetization), both SSA and porosity are decreased (Tab. 2.8). This decrease is accentuated in the case of Ti-M-PILC-60 and Ti-M-PILC-200.

Table 2.8: Specific surface areas and pore volumes of Ti-M-PILCs

Samples	SSA (m²/g)	SSA reduction* (%)	V_{mp} (cm³/g)	V_{mes} (cm³/g)	V_p (cm³/g)	V_p reduction* (%)
Ti-M-PILC-60	65	77	0.003	0.047	0.051	70
Ti-M-PILC-200	137	51	0.006	0.092	0.099	42
Ti-M-PILC-300	180	33	0.006	0.118	0.125	26
Ti-M-PILC-400	211	20	0.007	0.129	0.136	15
Ti-M-PILC-500	175	28	0.004	0.110	0.114	28
Ti-M-PILC-600	168	27	0.003	0.111	0.114	26

*: Specific surface area and pore volume reduction after magnetization

Pore size distribution

The NLDFT pore size distribution PSD curves of titanium magnetic materials are shown in Fig. 2.6. In all magnetic samples the pore volume shows a peak of maximal width in the mesoporous range at about 2.5-3.5 nm and the disappearance of the peak corresponding to the microporous range. This reflects that magnetic titanium pillared clays have only mesoporous structure.

2. Magnetic titanium pillared clays (Ti-M-PILCs)

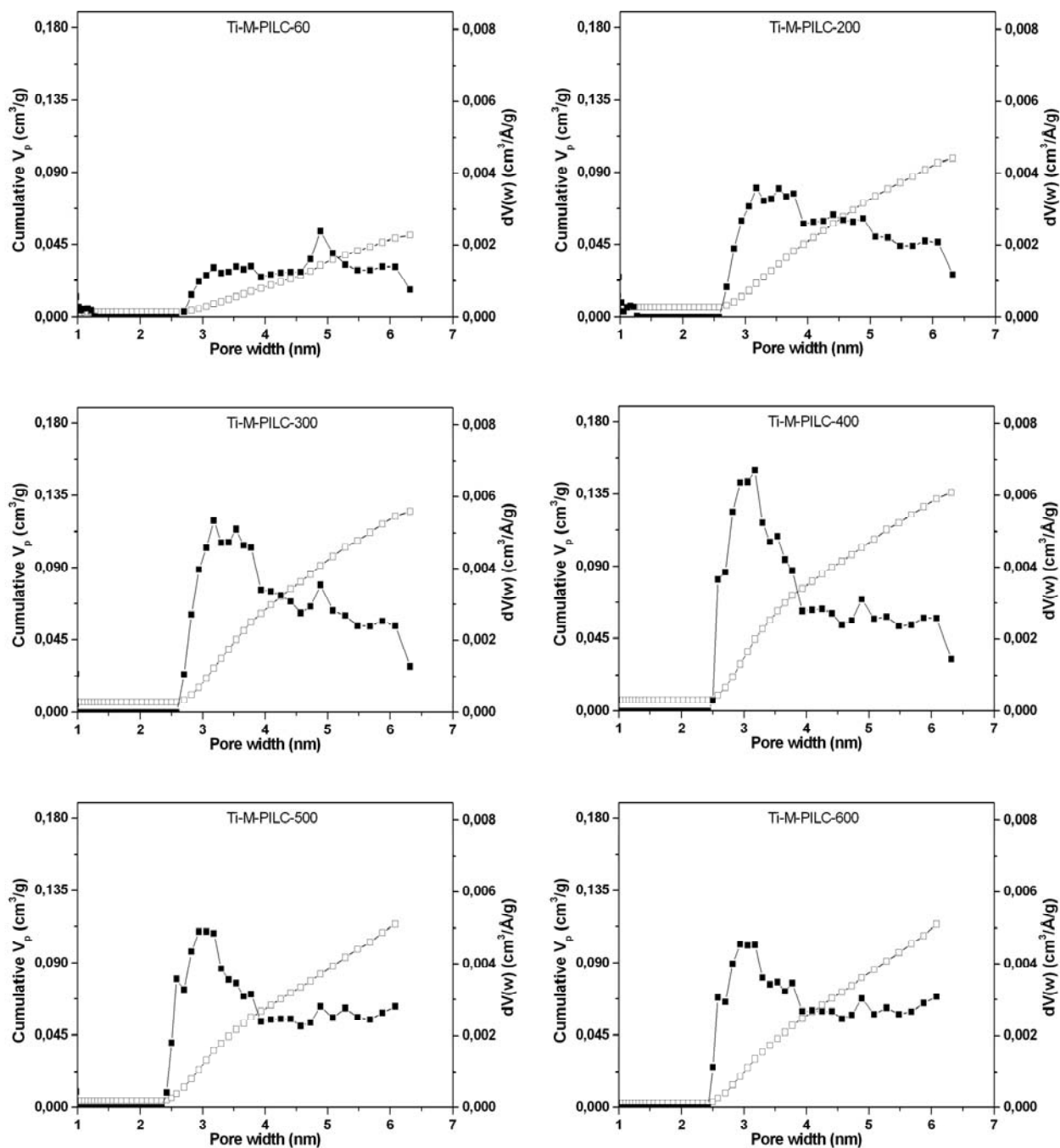


Figure 2.6: Pore size distribution of Ti-M-PILCs. Full symbols/ right y-axis: differential pore volume distribution curves, open symbols/ left y-axis: cumulative pore volume. curves.

*N*₂ isotherms

The *N*₂ isotherms of the magnetic materials obtained are shown in Fig. 2.7. The isotherm shapes correspond to type IV according to Sing *et al.*, (1985) characteristic of mesoporous materials. The hysteresis loop corresponds to type H4 in the IUPAC classification and this is characteristic of material with slit-like pores. These results indicate that the synthesized materials present mesoporosity as confirmed by the pore size distribution.

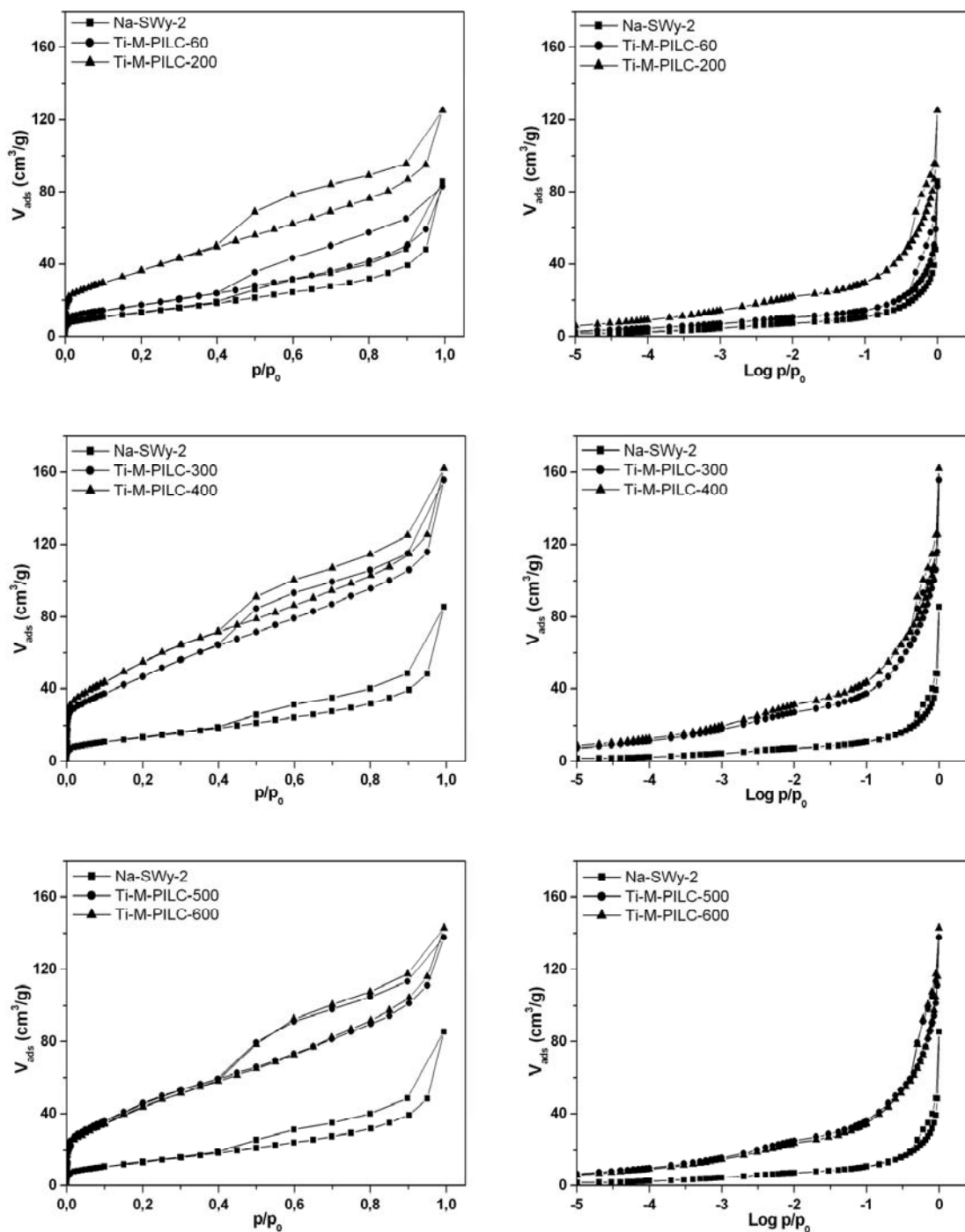


Figure 2.7: *N*₂ isotherms of Ti-M-PILCs

2. Magnetic titanium pillared clays (Ti-M-PILCs)

2.2.3. X-ray fluorescence XRF

Ti-M-PILCs were analysed by XRF (Tab. 2.9) in order to obtain the iron content after magnetization, which is responsible for the magnetic properties. This content has been calculated as follows:

$$\text{Fe}_2\text{O}_3^* = \text{Fe}_2\text{O}_3(\text{M-PILC}) - (\text{SiO}_2(\text{M-PILC}) / \text{SiO}_2(\text{Na-SWy-2})) * \text{Fe}_2\text{O}_3(\text{PILC})$$

here, $\text{Fe}_2\text{O}_3(\text{PILC})$ was normalised to the composition of Na-SWy-2.

The additional iron content of Ti-M-PILCs is constant for all samples and does not exceed 2 %. The additional TiO_2 content based on the composition of Na-SWy-2 has been deduced and will be used for the calculation of the filling factor.

Table 2.9: Fe_2O_3 and TiO_2 contents (%wt.) of Ti-M-PILCs and Ti-PILCs.

	Ti-M- PILC-60	Ti-M- PILC-200	Ti-M- PILC-300	Ti-M- PILC-400	Ti-M- PILC-500	Ti-M- PILC-600
Fe_2O_3^*	1.85	1.83	1.75	1.62	1.73	1.86
$\text{TiO}_2^\#$	48.84	49.01	48.89	49.93	50.95	51.27
	Ti- PILC-60	Ti- PILC-200	Ti- PILC-300	Ti- PILC-400	Ti- PILC-500	Ti- PILC-600
$\text{TiO}_2^\#$	49.44	49.44	49.53	49.43	49.42	49.31
ΔTiO_2	0.60	0.43	0.65	-0.50	-1.53	-1.96

*: Additional Fe_2O_3 content after magnetization based on the composition of Ti-M-PILCs.

#: Additional content based on the composition of Na-SWy-2 given as g of TiO_2 per 100 g of Na-SWy-2.

ΔTiO_2 : difference in TiO_2 content (% PILCs- % M-PILCs).

2.2.4. FTIR investigation

FTIR-ATR investigation

The structural OH-bending mode in montmorillonite absorbs IR radiation between 700 and 950 cm^{-1} and exhibits a series of peaks depending on the cations present in the octahedral sheet. In the case of Ti-PILCs two bands are observed at 913 and 875 cm^{-1} for all calcination temperatures (Fig. 2.8a). These bands have been assigned to the deformation of Al-Al-OH and Al-Fe-OH groups, respectively (Madejova and Komadel, 2001, and Farmer, 1974). The appearance of a weak band at 797 cm^{-1} indicates either the presence of traces of poorly crystalline silica (Si-O stretching of quartz and free silica) or Mg-Mg-OH vibrations. The band observed at 975 cm^{-1} is related to the stretching of Si-O group. A slight shift of this peak to higher wavenumber (986 cm^{-1}) with increasing calcination temperature has been observed. This phenomenon can be related to the dehydroxylation effect after calcination. This finding is supported by the decrease of CEC (Tab. 2.5).

As indicated by the XRD results of Ti-PILC-600, montmorillonite is still present in the sample. The ATR spectra show no major differences upon calcination at 600 °C.

Following the magnetization (Fig. 2.8b) it has not been possible to identify additional bands; specifically bands indicative of iron bearing phases. These results lead to conclude, that such phases are not present on the outer surfaces of Ti-M-PILCs.

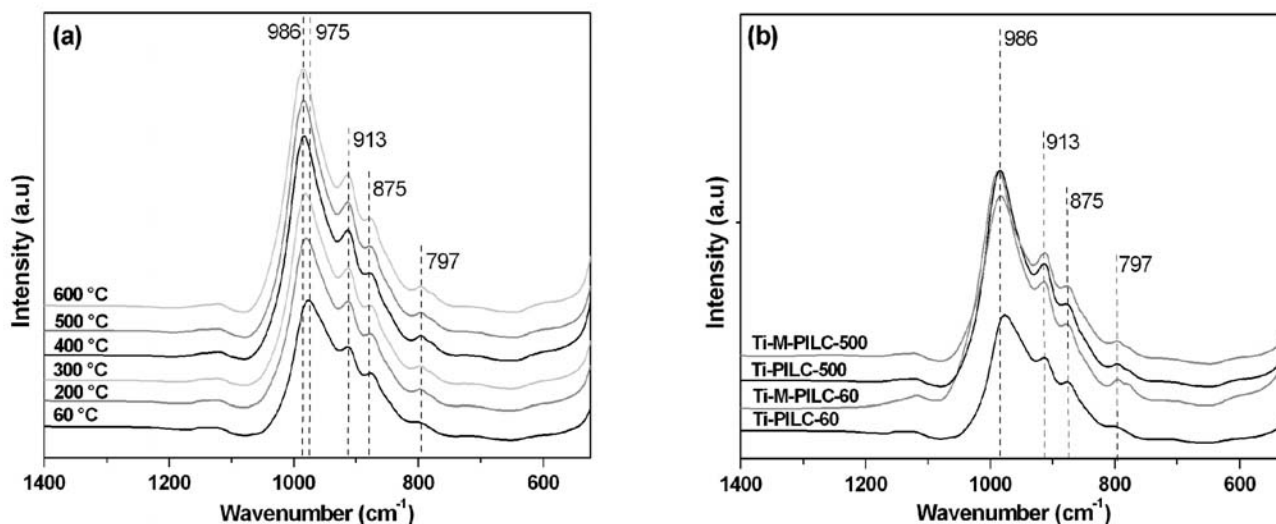


Figure 2.8: FTIR-ATR spectra of: a) Ti-PILCs and b) comparison of Ti-PILC-60 and Ti-PILC-500 with their magnetic form.

Far infrared spectroscopy

In addition to the FTIR-ATR measurements, the far infrared spectroscopy was applied in order to check whether the iron oxides are in the interlayer space of pillared materials. Besides the spectra of Ti-M-PILCs, spectra of magnetite, hematite, Na-SWy-2, and Na-SWy-2 mixed with 0.5-weight-% hematite were investigated (Fig. 2.9). Comparison of the reference spectra with those of Ti-M-PILCs revealed that hematite is present in the interlayer of the samples calcined at 60, 200 and 300 °C. For the samples heated initially at higher temperatures only traces can be found.

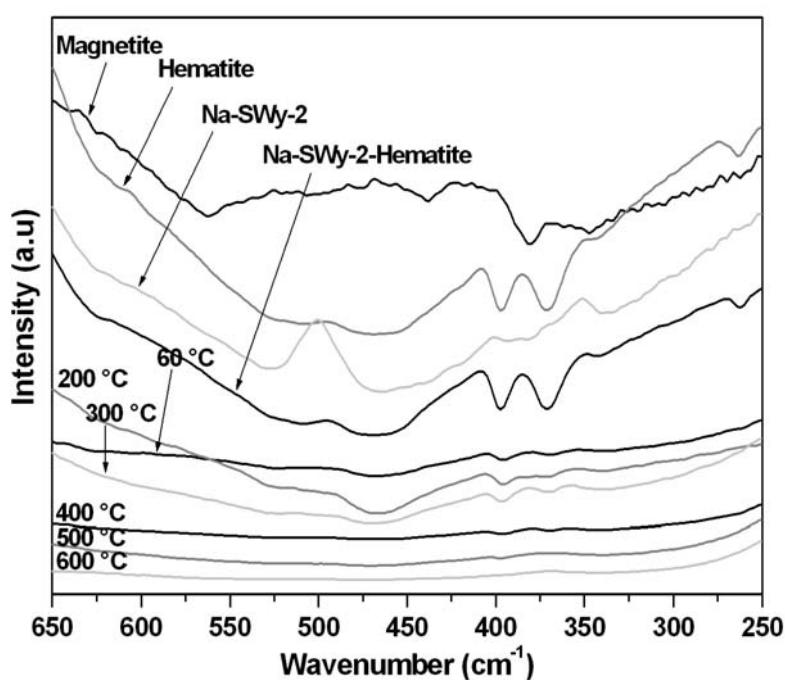


Figure 2.9: FIR spectra of Ti-M-PILCs, hematite, magnetite, Na-SWy-2, and Na-SWy-2-hematite.

2.2.5. Magnetic properties

Hysteresis curves (2, 5, 10, 50, 100, and 300 K)

The hysteresis curves of Ti-M-PILC-200 and Ti-M-PILC-300 exhibit similar shape as Ti-M-PILC-60, and those of Ti-M-PILC-400 and Ti-M-PILC-600 are similar to that of Ti-M-PILC-500. Thus, only those of Ti-M-PILC-60 and -500 are presented (Fig. 2.10), and the rest is reported in the Appendix. For Ti-M-PILC-60, hysteresis curves obtained at 50, 100, and 300 K have low areas (Fig. 2.10b). At 2, 5, and 10 K almost no hysteresis was obtained. The sample Ti-M-PILC-500 (Fig. 2.10d) reveals a pronounced hysteresis at all temperatures suggesting ferro(i)magnetic behaviour. Saturation magnetization increased furthermore with decreasing temperature for both Ti-M-PILC-60 and Ti-M-PILC-500 (Fig. 2.10). Ti-PILCs are only paramagnetic hence no hysteresis was obtained.

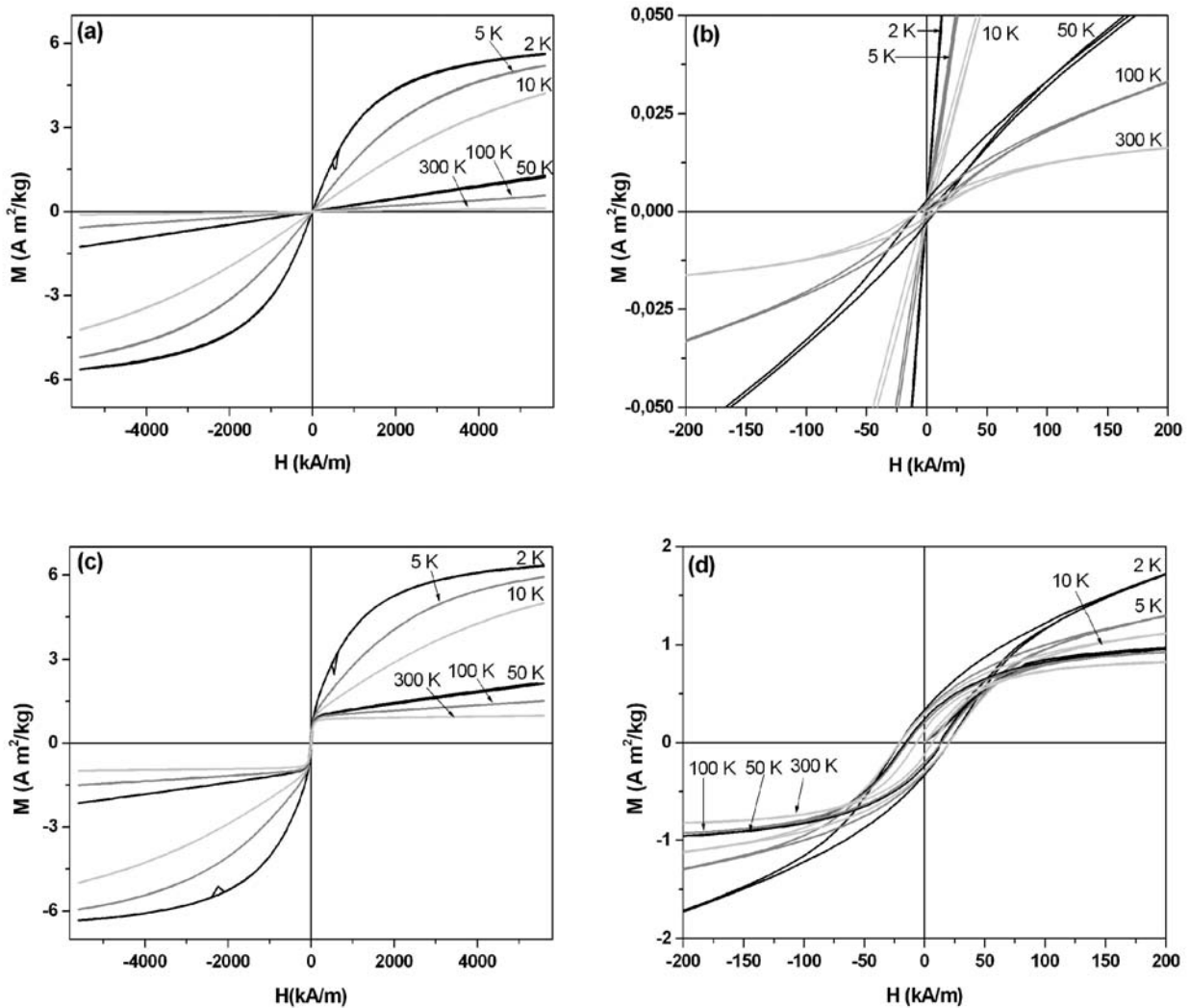


Figure 2.10: Hysteresis loops of Ti-M-PILC-60 (a, b) and Ti-M-PILC-500 (c, d). a, c: full range; b, d: zoom of loops.

2. Magnetic titanium pillared clays (Ti-M-PILCs)

Temperature dependency of hysteresis parameters

The variations of the M_s , M_{rs} , H_c , and M_{rs}/M_s of Ti-M-PILCs as a function of the SQUID measurement temperature are also depicted (Fig. 2.11). In general, the values increase with decreasing temperature. Exceptions from this trend can be observed for Ti-M-PILC-60 and Ti-M-PILC-200.

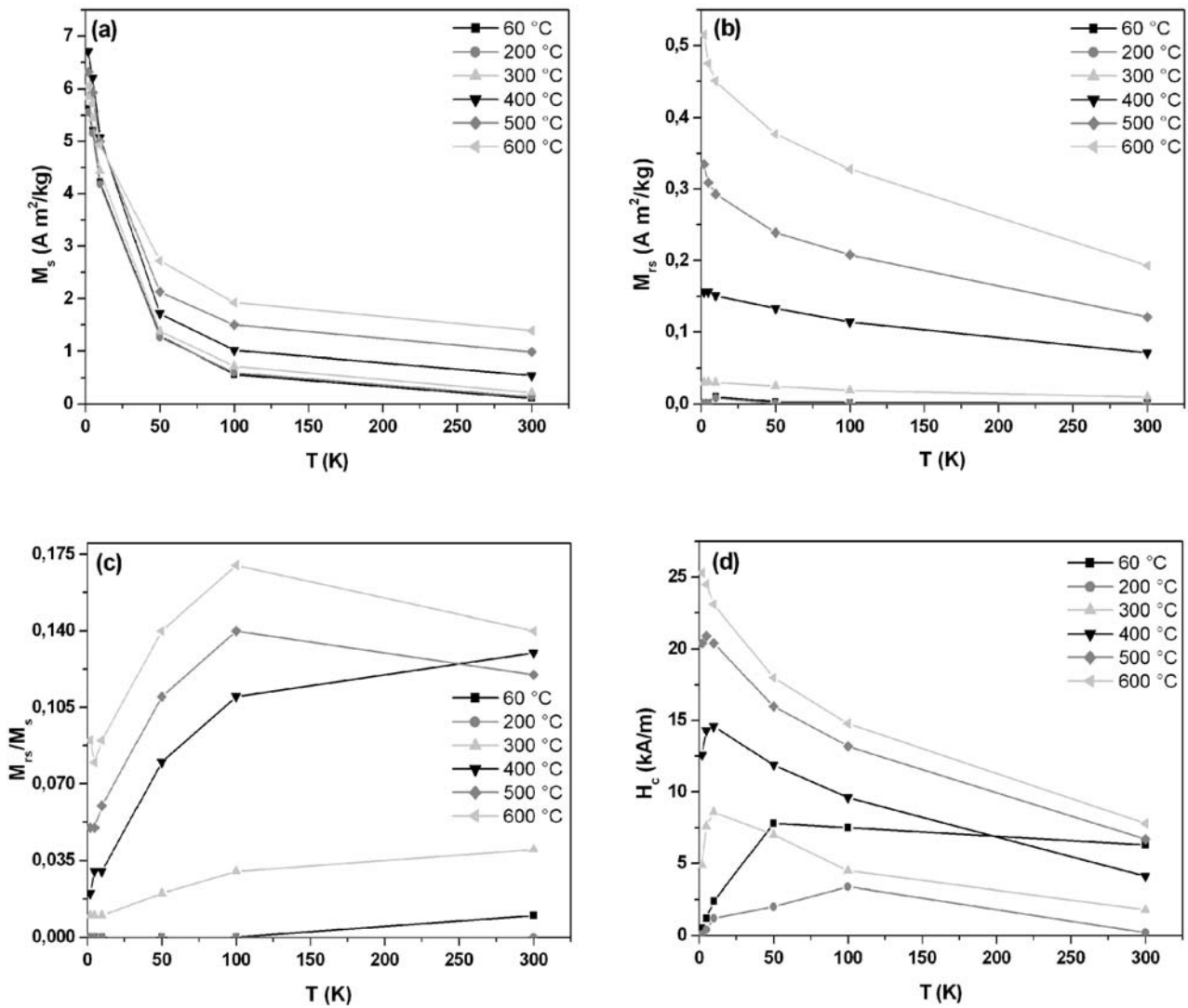


Figure 2.11: Temperature dependency of a) M_s , b) M_{rs} , c) M_{rs}/M_s , and d) H_c of Ti-M-PILCs.

2. Magnetic titanium pillared clays (Ti-M-PILCs)

Saturation magnetization at room temperature

To elucidate the nature of magnetic phases present in Ti-M-PILCs materials as well as the magnetic order, M_s at 300 K normalized to the additional iron content after magnetization have been determined (Tab. 2.10). Samples Ti-M-PILC-400, -500, and -600 show the highest M_s . Comparison with those of magnetite, maghemite, iron metal and Fe_xB (Moskowitz, 1991, and Zhang *et al.*, 2001) suggests the presence of such phases. The presence of a poorly ordered iron alloy must, however, also be considered.

Table 2.10: Specific saturation magnetization of Ti-M-PILCs at 300

Samples	$Fe_2O_3^{added}$ (Wt %)	M_s (A m ² /kg added iron)
Ti-M-PILC-60	1.85	6
Ti-M-PILC-200	1.83	8
Ti-M-PILC-300	1.75	12
Ti-M-PILC-400	1.62	33
Ti-M-PILC-500	1.73	57
Ti-M-PILC-600	1.86	75
Magnetite Fe_3O_4		90-92
Maghemite $\gamma-Fe_2O_3$		60
Iron Fe		218
Fe_xB		~60

Magnetic domain status

The M_{rs}/M_s - H_{cr}/H_c diagram at 300 K is compared with that obtained for magnetite by Moskowitz (1991) (Fig. 2.12). From this comparison Ti-M-PILC-500 and -600 exhibit PSD state, Ti-M-PILC-300 and -400 are in the transition range between MD and PSD, Ti-M-PILC-60 can be MD. The sample Ti-M-PILC-200 lacking M_{rs} and therefore H_{cr} could not be determined.

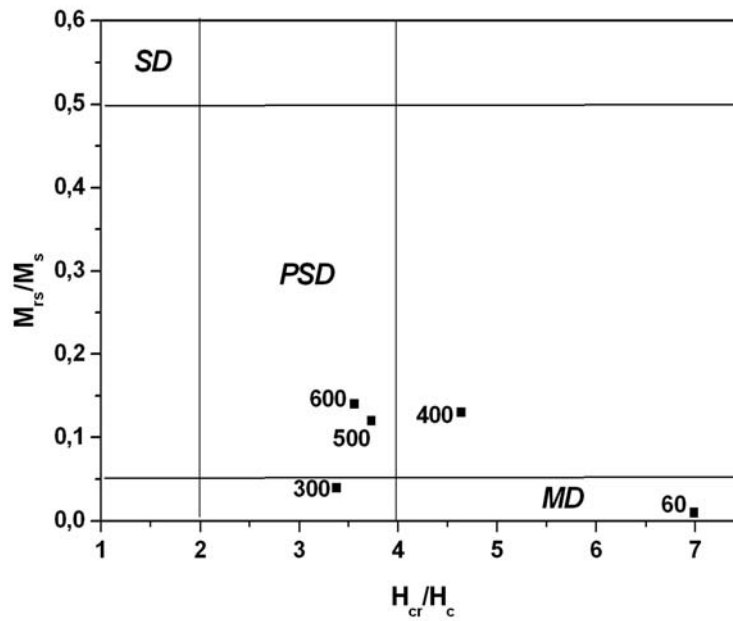


Figure 2.12: M_{rs}/M_s - H_{cr}/H_c diagram of Ti-M-PILCs at 300 K. Domain classification after Moskowitz, (1991).

ZFC/FC investigation

For Ti-M-PILC-600 (similar shape as Ti-M-PILC-500 and -400 (Fig. 2.13)) the obtained curve can be interpreted as a broad and shallow distribution of blocking temperatures related to the presence of very weak magnetic ordering. In the case of Ti-M-PILC-60 (similar shape as 200 and 300) the plot does not show any blocking temperature and is typically found for paramagnetic behaviour in this temperature range.

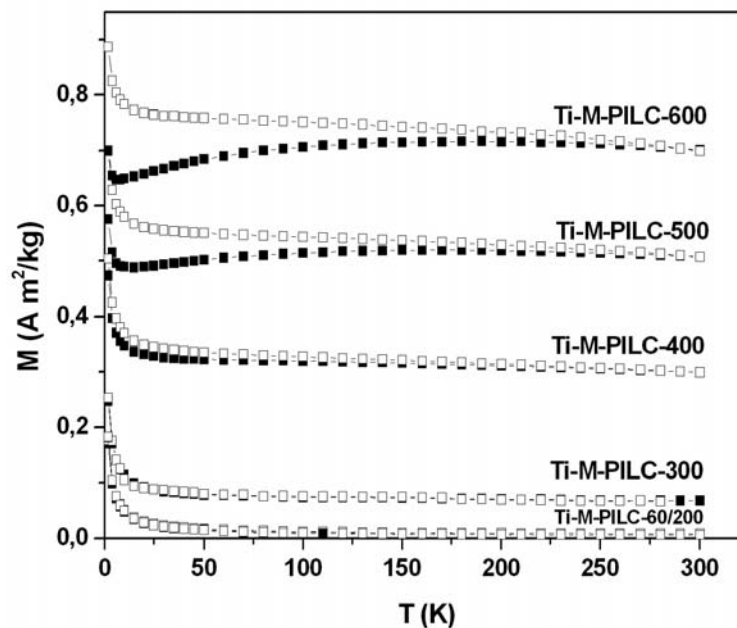


Figure 2.13: ZFC/FC curves of Ti-M-PILC. Full symbols ZFC, open symbols FC curves.

2. Magnetic titanium pillared clays (Ti-M-PILCs)

Curie-Weiss law: Determination of θ and C

The negative sign of θ (Tab. 2.11) indicates that all Ti-M-PILCs behave as ferrimagnetic materials. The first three samples however, possess a very small theta value and this finding corresponds to the results of the ZFC/FC examination, where these samples exhibited a more paramagnetic behaviour, which is characterized by a theta value of zero.

The Curie constant C increases with calcination temperature. If the number of Fe atoms N is estimated to be the same for all samples, as can be assumed from XRF-analysis (Section. 2.2.3), the effective magnetic number of Bohr magnetons p_{eff} related to C therefore increases for the samples calcined at higher temperatures. Knowing that p_{eff} of Fe^{3+} (5.92) is greater than that of Fe^{2+} (4.90), leads to the conclusion that the Fe^{3+} content is higher at higher calcination temperatures.

Table 2.11: Parameters of the Curie-Weiss-law of Ti-M-PILCs.

Samples	θ (K)	$C \cdot 10^6$ ($\text{m}^3 \text{K/Kg}$)	R^2
Ti-M-PILC-60	-0.8	11.9	1.000
Ti-M-PILC-200	-0.7	12.0	1.000
Ti-M-PILC-300	-0.5	11.7	0.994
Ti-M-PILC-400	-1.9	18.1	0.962
Ti-M-PILC-500	-2.3	17.3	0.931
Ti-M-PILC-600	-4.6	23.3	0.854

θ : Weiss constant and C: Curie constant

2.2.6. Mössbauer spectroscopy

Ti-M-PILCs were investigated by Mössbauer spectroscopy at room temperature. In addition to the all-ferric paramagnetic doublet, that characterizes the untreated SWy-2 sample (Fig. 2.14), a minor ferrous doublet can be observed in the spectra of the samples heated at 60, 200, and 300 °C (Fig. 2.15a). This indicates that the borohydride reduction only is partially effective in reducing the ferric ions.

The spectra of the samples heated at 400, 500, and 600 °C exhibit in addition to the ferric and ferrous doublets a very broad component contributing to absorption between approximately ± 4 mm/s (Fig. 2.15b). This broad component is interpreted as a magnetically split sextet due to FeB-alloys of different compositions (Van Wontergehm *et al.*, 1986). The absence of resolved lines in the sextet is presumably caused by high local variation in the composition (possibly including both B and Ti in the alloy).

The $\text{Fe}^{2+}/\text{Fe}^{3+}$ ratio (Tab. 2.12) decreases with higher calcination temperature up to 400 °C, which is in agreement with the results given by the Curie-Weiss-law calculations in the paramagnetic region. In the case of Ti-M-PILC-60 either at 300 or 3 K (Fig. 2.15a and Fig. 2.16a) the Mössbauer spectra contain two distinguishable quadrupolar split resonances. A superposition of quadrupole doublets with Lorentzian line shapes was used to fit these spectra. Spectral subcomponents for Ti-M-PILC-60 have Mössbauer spectral parameters characteristic of high-spin iron (II) and (III). No magnetic ordering was observed.

The similar spectra were obtained for Ti-M-PILC-200, -300, -400, -500, and -600. The spectra of Ti-M-PILC-600 at 300 and 3 K (Fig. 2.15b and Fig. 2.16b) are characterized by a distribution on relaxation times, more pronounced for 3 K. Due to this distribution, part of the sample relaxes fast in the Mössbauer time scale giving rise to a doublet and part of the sample relaxes slowly giving rise to a sextet characteristic of magnetic ordering. In addition, no evidence for metallic iron is found in any spectrum.

2. Magnetic titanium pillared clays (Ti-M-PILCs)

Table 2.12: $\text{Fe}^{2+}/\text{Fe}^{3+}$ ratios, isomer shift (IS) and quadrupole splitting (QS) determined by Mössbauer spectroscopy of Ti-M-PILCs.

Samples	$\text{Fe}^{2+}/\text{Fe}^{3+}$ ratio	Fe^{2+} IS (mm/s)	Fe^{2+} QS (mm/s)	Fe^{3+} IS (mm/s)	Fe^{3+} QS (mm/s)
Ti-M-PILC-60	0.16	1.15	2.91	0.38	0.75
Ti-M-PILC-200	0.14	1.16	2.94	0.39	0.73
Ti-M-PILC-300	0.10	1.13	2.84	0.35	0.75
Ti-M-PILC-400	0.09	1.21	2.85	0.36	0.78
Ti-M-PILC-500	0.20	1.20	2.72	0.33	0.89
Ti-M-PILC-600	0.14	1.19	2.64	0.33	0.89

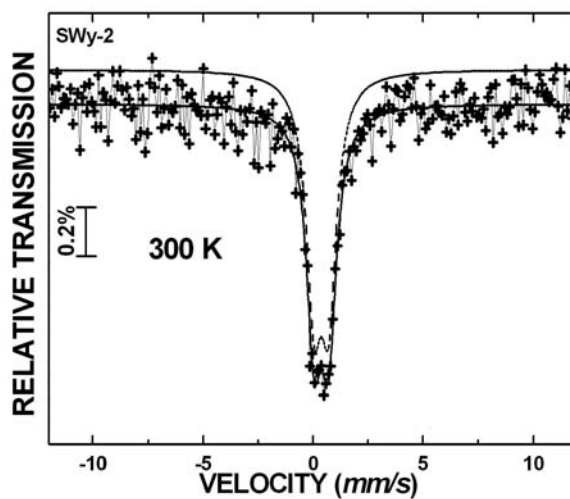


Figure 2.14: Mössbauer spectrum of SWy-2 at room temperature.

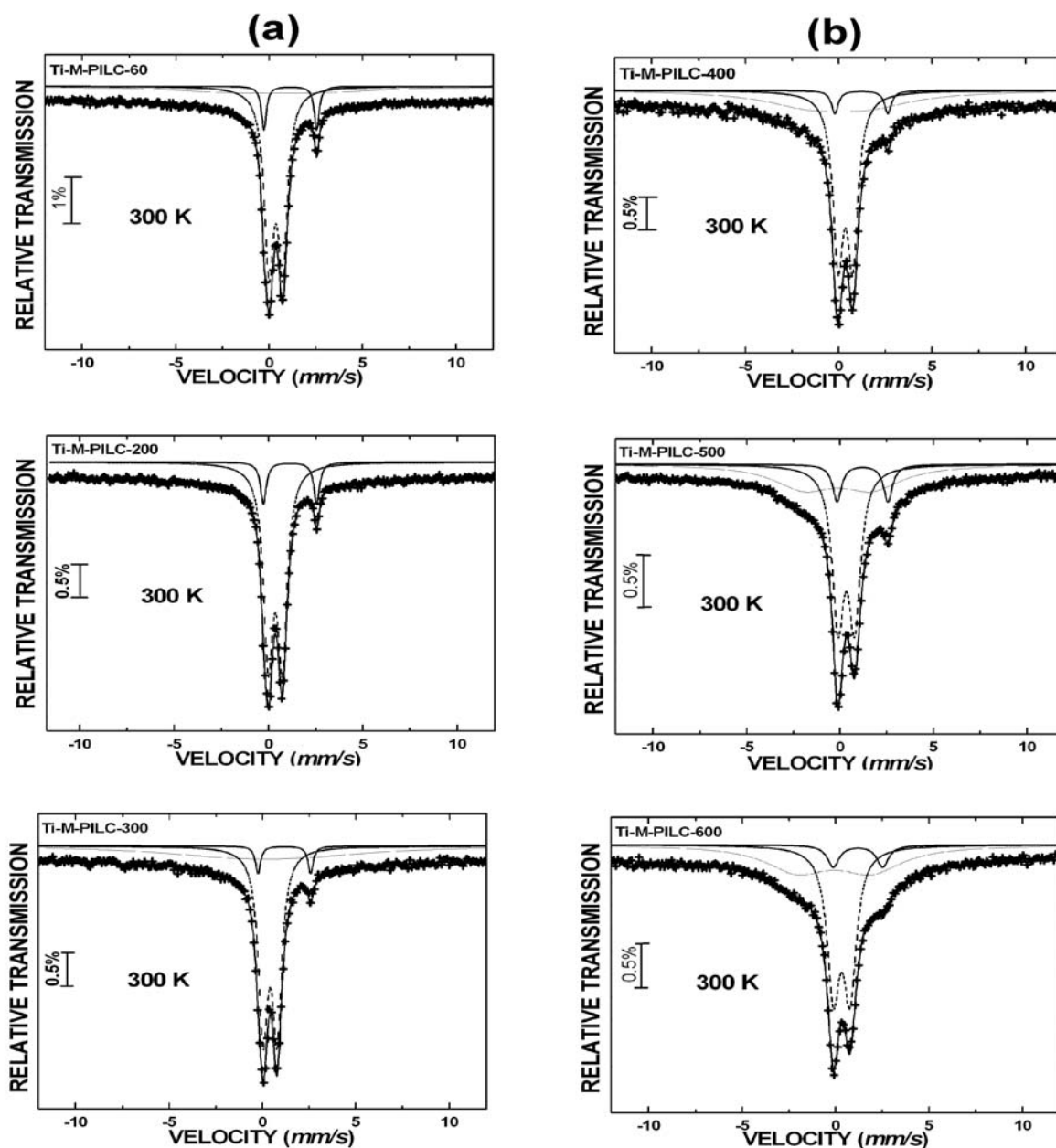


Figure 2.15: Mössbauer spectra of Ti-M-PILCs at room temperature.

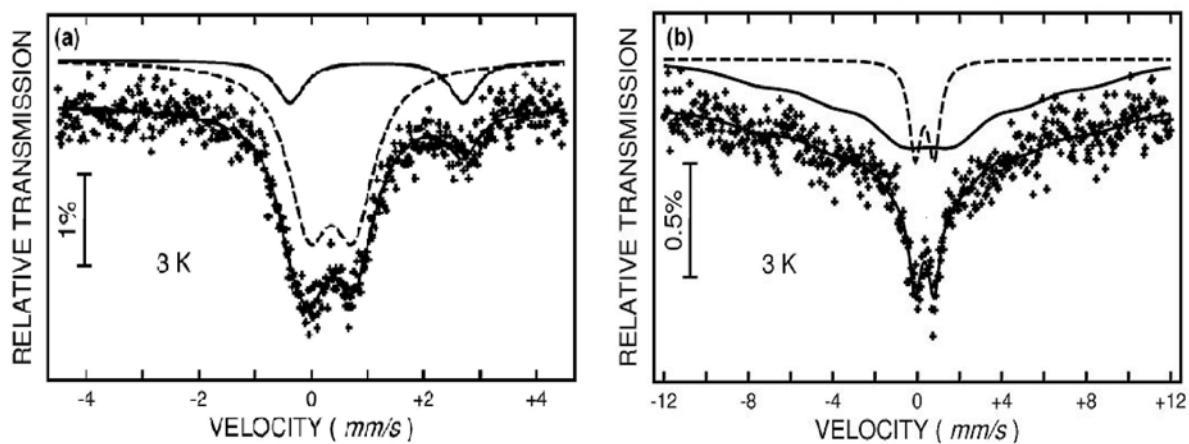


Figure 2.16: Mössbauer spectra at 3 K of a) Ti-M-PILC-60 and b) Ti-M-PILC-600.

2.3. Discussion

The Ti-PILC structure was affected during the reduction process. Rozenon and Heller-Kallai (1976) reported the reduction of Fe^{3+} in octahedral positions of smectites upon treatment with hydrazine and dithionite. This reduction was reversible, as they showed with FT-IR data. The band assigned to the Fe-OH-Al vibration at 870 cm^{-1} disappeared upon reduction and after a following oxidation reappeared. This reduction led to the partial deterioration of the Ti-PILC-structure, but after the introduction of the additional iron. This deterioration was more pronounced for the samples calcined at lower temperatures, hence lower stability, as indicated by the higher loss in SSA and porosity (Tab. 2.8). Re-oxidation of the Fe in the octahedral positions occurred since the bands at 875 cm^{-1} did not change (Fig. 2.8b).

Calcination temperature influences the SSA, the porosity, and the stability but the Ti-PILCs react differently on the magnetization process, which consists of the adsorption of Fe and reduction by NaBH_4 . Although the amount of additional iron is the same for all Ti-PILC samples, the M_s normalized to the additional amount of iron, is very different for each sample (Tab. 2.10). Some M_s values speak in favour of magnetite/maghemite phases, other for the presence of a FeB-alloy. Mössbauer data prove the presence of divalent and trivalent iron, but the calculated ratios are lower than 0.5, the characteristic value for stoichiometric magnetite. The sign of the Weiss constant θ supports the presence of a ferrimagnetic phase.

All the forgoing arguments speak in favor of the presence of a poorly ordered iron-boron alloy. The expected particle sizes of the additional iron containing alloys are confined to the dimension of the interlayer space of around 1.7 to 1.9 nm. Moreover, it can be supposed that the iron-alloy particles stretch wider within the interlayer, forming a thin flat entity. The assumption of such a shape is supported by the broad and shallow FC/ZFC curves indicating a broad distribution of freezing temperatures over a large temperature range from 3 to 300 K. This prevents any long range magnetic ordering which is also lacking in the Mössbauer data. Only the Ti-M-PILC-600, which possesses the highest saturation magnetization and the highest remanence values both for magnetization and coercivity, exhibits traces of a beginning of magnetic ordering in its Mössbauer spectrum at 3 K. Similar conditions, but with decreasing magnetic ordering with decreasing calcination temperature can be assumed for the Ti-M-PILC calcined between 500 and 400 °C.

The higher relative loss in porosity and specific surface area is reflected in the temperature behaviour of the magnetization (ZFC/FC) and Curie-Weiss parameters. These data, especially the Curie-constant C (Tab. 2.11) can be interpreted in a higher dilution of the magnetic

2. Magnetic titanium pillared clays (Ti-M-PILCs)

carriers. This on one hand can be explained by the higher SSA and porosity of the less calcined samples thus leading to a wider spread of the Fe particles. The accessibility of the additional iron for these less calcined samples is promoted by the well ordered PILC layers as indicated by the intensity of the (002) peak. For the more calcined samples less SSA and porosity is available and the interlayer spacing is less well pronounced, leading more easily to a clustering. But the separating TOT-layers hinder the formation of well ordered magnetic domains in these units and lead to the observed FC/ZFC behaviour.

The presence of these two different Fe-alloy distributions, dispersed for the lower calcined ones, and cluster for the higher calcined Ti-PILCs (Fig. 2.17), can be explained by the CEC. The less calcined samples are higher charged which prevents clustering because the intercalated Fe-species have to compensate the surplus of negative charge. For the low CEC samples, the high temperature calcined samples, a surplus of Fe-species is available which can adhere to already adsorbed Fe-sites within the interlayer compensating the interlayer charge. The clustering can be promoted during the reduction process, where reduced Fe^{2+} ions, known to be more mobile than trivalent Fe species, adsorb to already existing clusters similar to what is known as Ostwald ripening.

In addition, the presence of hematite in the low temperature calcined samples, as shown by FIR, supports the present magnetic results.

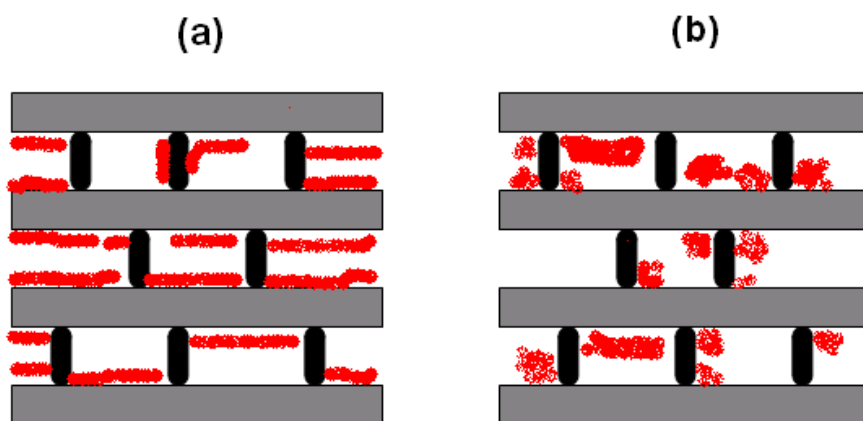


Figure 2.17: Model explaining the obtained results:
(a) Dispersed iron alloys/ high CEC, low temperature calcined samples,
(b) Iron alloys clustering/ low CEC, high temperature calcined samples.

Furthermore, in the case of Ti-PILCs and the associated Ti-M-PILCs, the obtained intercalation factor of 1 and larger (Tab. 2.13) must be interpreted as a complete filling of the entire interlayer space. Pore volume data, especially microporosity, which is due essentially to the pillaring, clearly contradicts this interpretation. Therefore, most of the Ti is located on the

2. Magnetic titanium pillared clays (Ti-M-PILCs)

surface. This is also indicated by the increase in the intensity of the anatase peaks in the X-ray diffractograms (fig. 2.1b and 2.5b).

In this set of experiments the best calcination temperature is 400 °C, which maintained the highest SSA and pore volume with magnetic parameters suitable for magnetic application.

Table 2.13: FF and IF of Ti-PILCs and Ti-M-PILCs

Samples	V_p (cm³/g)	V_{IL}^{the} (cm³/g)	V_{IL}^{exp} (cm³/g)	FF	IF
Ti-PILC-60	0.169	0.686	0.296	0.4	2
Ti-PILC-200	0.171	0.686	0.298	0.4	2
Ti-PILC-300	0.169	0.686	0.296	0.4	2
Ti-PILC-400	0.160	0.630	0.287	0.5	2
Ti-PILC-500	0.158	0.574	0.285	0.5	2
Ti-PILC-600	0.153	n.d	1.279	n.d	n.d
Ti-M-PILC-60	0.051	0.276	0.176	0.6	2
Ti-M-PILC-200	0.099	0.276	0.225	0.8	1
Ti-M-PILC-300	0.125	0.228	0.250	1.1	1
Ti-M-PILC-400	0.136	0.228	0.264	1.2	1
Ti-M-PILC-500	0.114	0.153	0.245	1.6	1
Ti-M-PILC-600	0.114	n.d	0.245	n.d	n.d

n.d: not determined.

3. Magnetic aluminium pillared clays (Al-M-PILCs)

For preparing aluminium pillaring solution a sodium hydroxide solution, 0.225 M NaOH, was added dropwise with vigorous stirring to a 0.5 M $\text{AlCl}_3 \cdot 6\text{H}_2\text{O}$ solution. The amounts of sodium hydroxide added were calculated in order to obtain OH/Al molar ratio of 2. This solution was aged for 24 h. The intercalated montmorillonites were prepared by slow addition under stirring of corresponding amounts of pillaring solution to the suspension of Na-SWy-2 montmorillonite in order to obtain 10 mmol of Al/g clay. The mixture was stirred for 17 h. The solids were separated by centrifugation, washed with distilled water and dried at 60 °C. The intercalated solids were calcined at different temperatures (200, 300, 400, 500 and 600 °C) for 4 h at a heating rate of 1 °C/min from room temperature up to the calcination temperature. Moreover, magnetic properties were conveyed to the Al-PILCs (Zhang and Manthiram, 1996) by ion-exchange of the present interlayer ion with an excess of ferrous iron (0.2 M $\text{FeCl}_2 \cdot 4\text{H}_2\text{O}$) followed by the reduction using 0.5 M NaBH_4 .

3.1. Aluminium pillared clays

3.1.1. XRD investigation

The oriented diffractograms of different calcined Al-PILCs are shown in Fig. 3.1a. The corresponding d_{001} spacings of these samples are provided in Tab. 3.1.

Table 3.1: d_{001} values of Al-PILCs

Samples	d_{001} (nm)
Al-PILC-60	1.87
Al-PILC-200	1.62
Al-PILC-300	1.76
Al-PILC-400	1.73
Al-PILC-500	1.66
Al-PILC-600	1.65

Two peaks were observed in the XRD patterns. The first peak corresponds to the d_{001} spacing of aluminium pillaring. The second peak with small d-spacing at around $9.3^\circ 2\theta$ can be attributed to the d_{002} spacing caused by aluminium pillaring. Upon increasing calcination temperature, the intensity of this peak decreases.

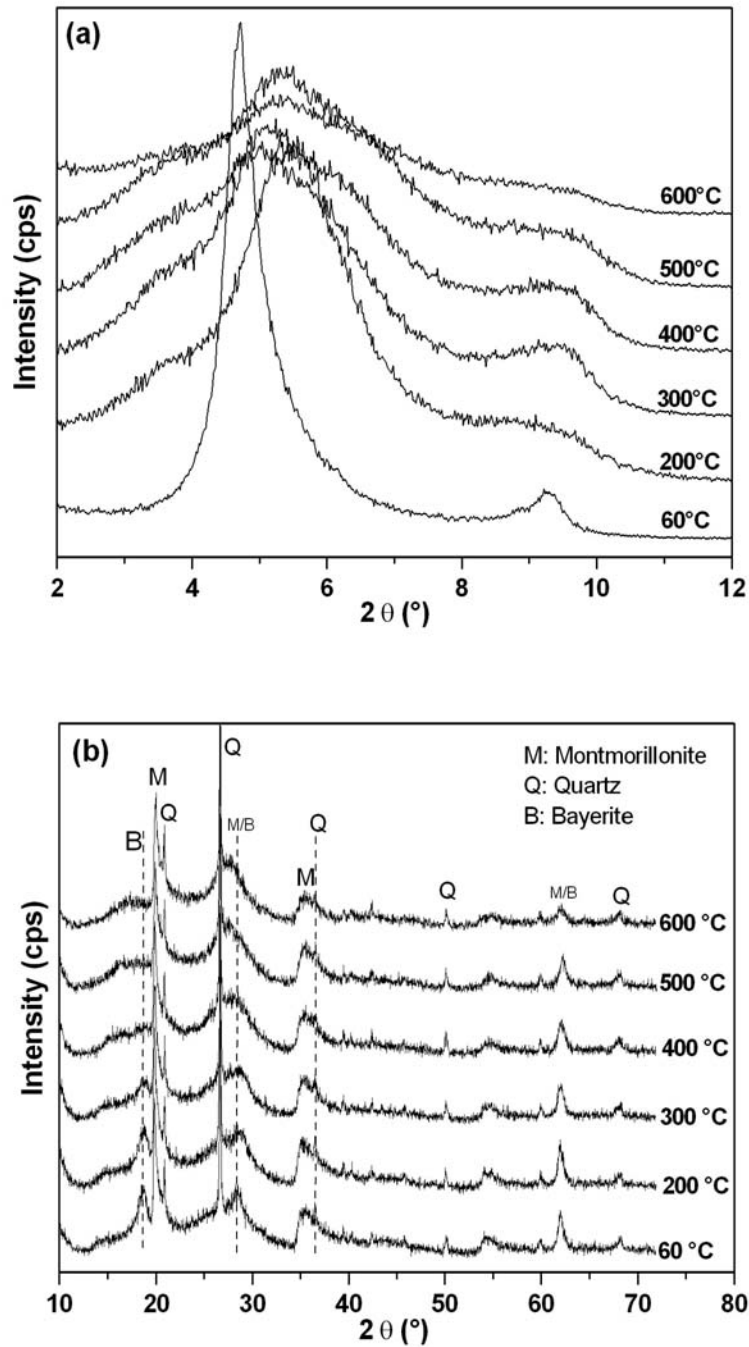


Figure 3.1: a) Oriented X-ray diffractograms of aluminium pillared clay dried at 60 °C and calcined at various temperatures and b) Powder X-ray diffractograms of Al-PILCs.

The presence of the (002) peak has been also confirmed in the case of Ti-PILCs (Bachir *et al.*, 2009). Besides quartz and montmorillonite (Fig. 3.1b), the powder diffractograms reveals the presence of (001) peak attributable to bayerite ($\text{Al}(\text{OH})_3$). The intensity of this peak decreases with increasing calcination temperature, until disappearance at 400 °C. As reported in literature (Levin *et al.*, 1998) when heated in air, the bayerite transforms into boehmite (γ -

3. Magnetic aluminium pillared clays (Al-M-PILCs)

AlOOH) which transforms to α -Al₂O₃ via a sequence of aluminas (γ -Al₂O₃, δ -Al₂O₃ or η -Al₂O₃, and θ -Al₂O₃). However, such phases were not found in the powder diffractograms (Fig. 3.1b), thus the values of D and β of the higher calcined samples could not be determined.

Sample	Bayerite		
	Al-PILC-60	Al-PILC-200	Al-PILC-300
β	0.863	0.948	0.812
D (nm)	10.4	9.4	11.0

3.1.2. N₂ adsorption

SSA and porosity

The structural parameters of the pore structure, including specific surface areas SSA, total pore volume V_p , micro- and mesopore volumes (V_{mp} , V_{mes}), are summarized in Tab. 3.3. An Al-pillaring process has been carried out successfully in montmorillonite matrix leading to the increase in SSA and pore volume mostly in the micropore range. The SSA decreases with increasing calcination temperature. However, thermal treatment at 600 °C had a strong effect on the SSA and porosity indicating a low thermal stability of the Al-PILCs clay at this temperature. The obtained data indicate that the formation of new pores, mostly micropores, after pillaring, is responsible for the increase in the surface areas. The mesoporosity also contributes to the considered total pore volume.

Table 3.3: Specific surface areas and pore volumes of Al-PILCs.

Samples	SSA (m ² /g)	V_{mp} (cm ³ /g)	V_{mes} (cm ³ /g)	V_p (cm ³ /g)
Al-PILC-60	243	0.086	0.029	0.115
Al-PILC-200	220	0.074	0.032	0.106
Al-PILC-300	206	0.064	0.040	0.104
Al-PILC-400	183	0.048	0.055	0.103
Al-PILC-500	180	0.043	0.060	0.103
Al-PILC-600	128	0.040	0.020	0.063

SSA: specific surface area, V_p : pore volume at $P/P_0 = 0.7$ (pore width ≤ 7 nm), V_{mp} : micropore volume, V_{mes} : mesopore volume.

3. Magnetic aluminium pillared clays (Al-M-PILCs)

Pore size distribution

The NLDFT cumulative pore volume and the corresponding differential pore volume distribution curves of Al-PILCs calculated from adsorption branch are depicted in Fig. 3.2. For Al-PILCs, the pore volume accumulates around a single type of pore, with a maximum at 1.5 nm (microporous range). This peak decreases in intensity with increasing calcination temperature.

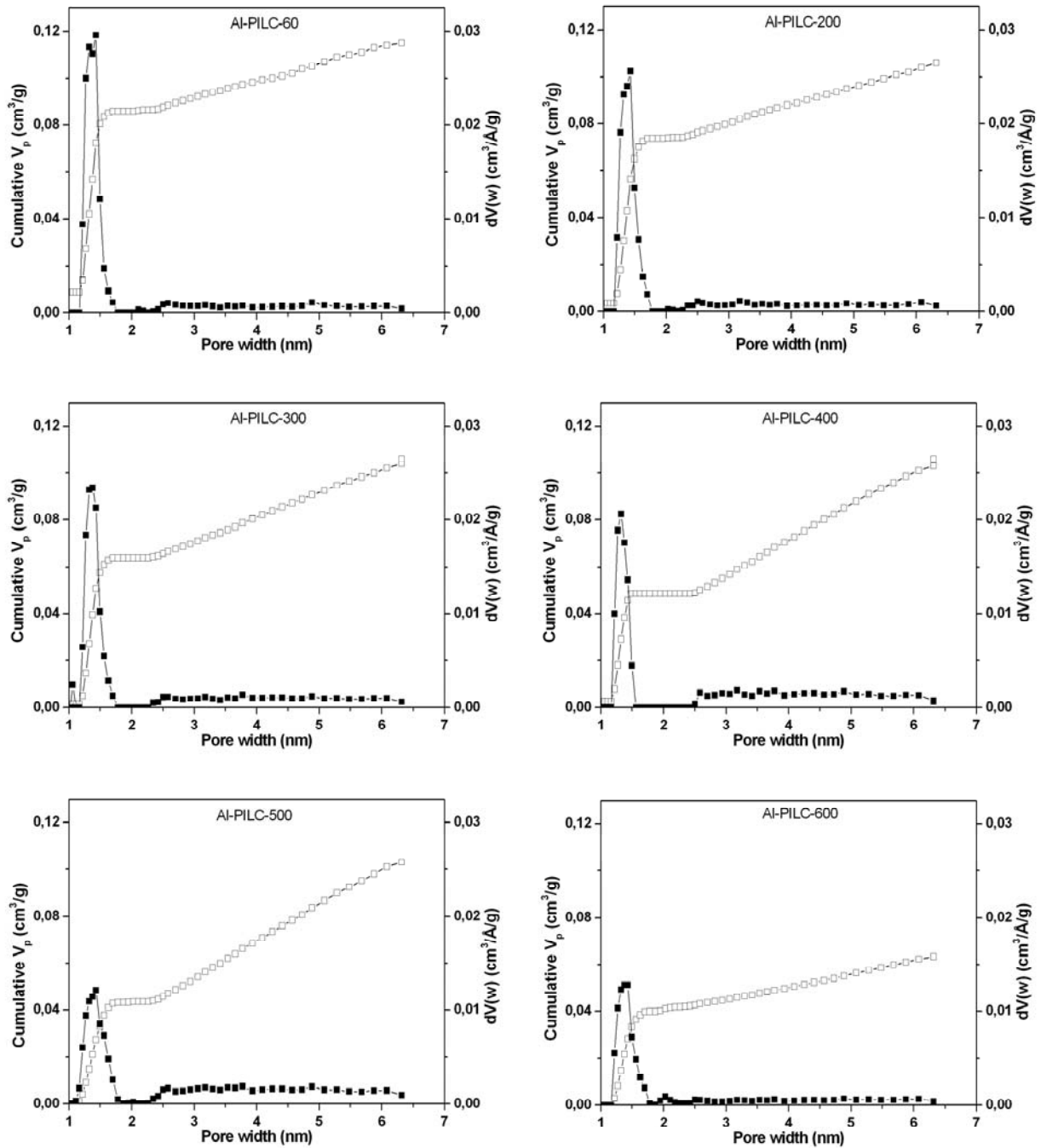


Figure 3.2: Pore size distribution of Al-PILCs. Full symbols/ right y-axis: differential pore volume distribution curves, open symbols/ left y-axis: cumulative pore volume curves.

N₂ isotherms

In Fig. 3.3 the N₂ isotherms of Al-PILCs are compared with the one of the Na-SWy-2. All the Al-PILCs isotherms presented in the linear and logarithmic relative pressure x-axis show an increase of the adsorbed volume almost exclusively in the micropore range, when compared with the original clay, as a result of the insertion of aluminium pillars.

The isotherm shapes of Al-PILCs correspond to type IV (Sing *et al.*, 1985, S. Lowell *et al.* 2006) characteristic of mesoporous materials. However, in the zone of low relative pressure values, Al-PILCs present type I isotherm, indicating the presence of micropores.

The existence of mesoporosity is also supported by the presence of hysteresis loops in all samples. In the case of the original clay, the mesoporosity is due to the clay structure itself as explained in chapter 2. The hysteresis loop corresponds to type H4 in the IUPAC classification characteristic of material with narrow slit-like pores.

3. Magnetic aluminium pillared clays (Al-M-PILCs)

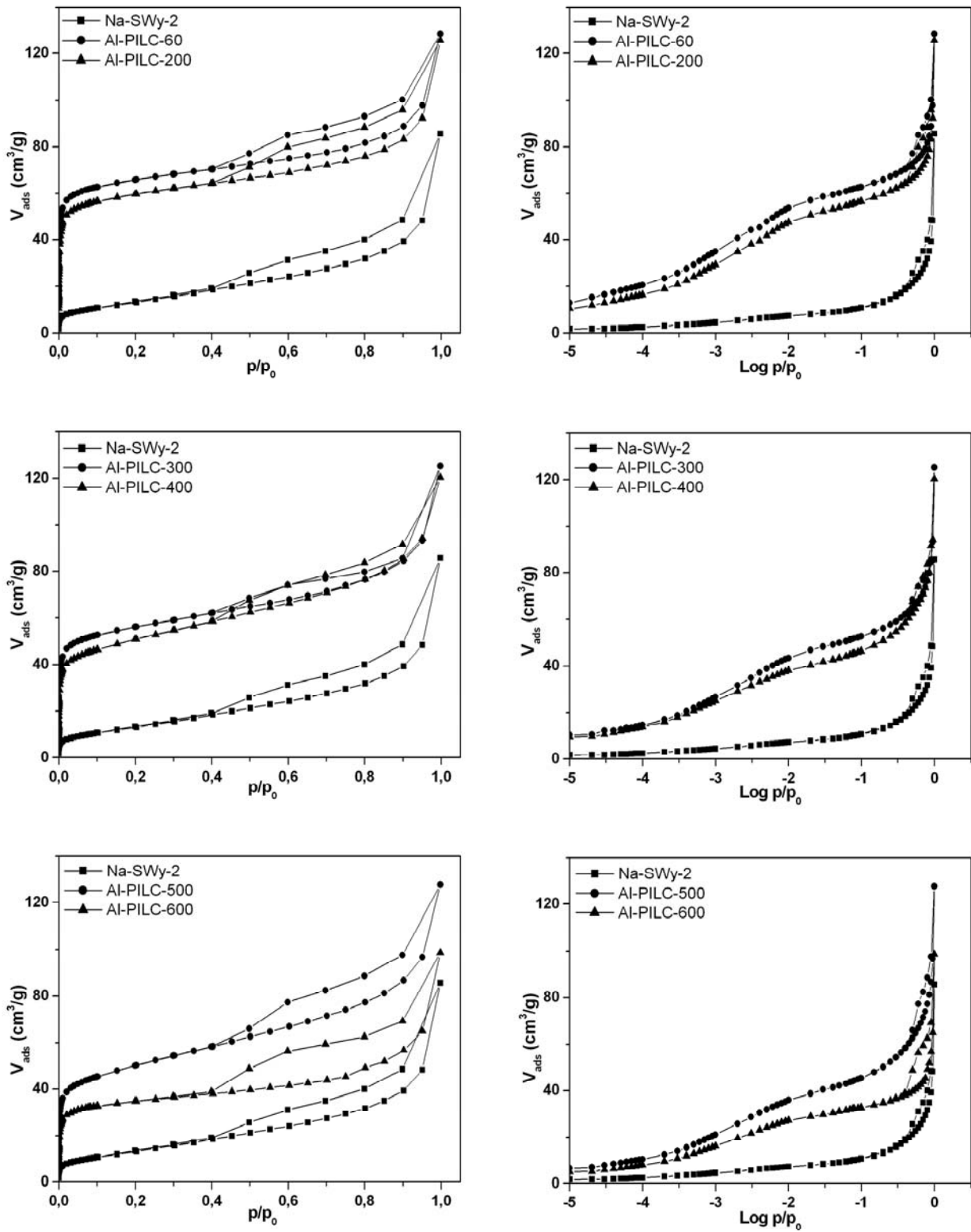


Figure 3.3: N₂ isotherms of Al-PILCs

3. Magnetic aluminium pillared clays (Al-M-PILCs)

3.1.3. X-ray fluorescence XRF

The chemical composition of Al-PILCs compared with the starting clay, determined by XRF, is given in Tab. 3.4. An increase of the Al₂O₃ content was obtained after pillaring. The oxide content related to the interlayer exchangeable cation, essentially sodium, is lowered except that of MgO. The LOI decreases with increasing heat treatment. The same behaviour was observed in the case of Ti-PILCs materials.

Table 3.4: Chemical composition reported as oxides (%wt.) of Na-SWy-2 and Al-PILCs.

Samples	Na-SWy-2	Al-PILC-60	Al-PILC-200	Al-PILC-300	Al-PILC-400	Al-PILC-500	Al-PILC-600
SiO₂	60.42	52.02	56.61	55.89	55.49	59.12	58.79
Al₂O₃	19.79	24.56	26.71	26.39	26.14	27.85	27.68
Fe₂O₃	3.99	3.45	3.75	3.70	3.68	3.91	3.88
MnO	0.01	0.01	0.01	0.01	0.01	0.01	0.01
MgO	2.34	1.99	2.18	2.14	2.13	2.27	2.26
CaO	0.13	0.01	0.01	0.01	0.01	0.01	0.01
Na₂O	2.21	0.02	0.02	0.03	0.02	0.02	0.02
K₂O	0.11	0.08	0.08	0.08	0.08	0.09	0.08
TiO₂	0.11	0.10	0.10	0.10	0.10	0.11	0.11
P₂O₅	0.02	0.02	0.02	0.02	0.02	0.02	0.02
SO₃	0.02	0.01	0.01	0.02	0.01	0.01	0.02
LOI	10.85	17.68	10.44	11.54	12.24	6.53	7.05

3.1.4. Simultaneous thermal analysis

In order to investigate the thermal stability of Al-PILCs calcined at different temperatures, simultaneous thermal analysis has been applied. The water content of Al-PILC obtained at different temperatures decreased with increasing calcination temperature; the same behavior is obtained from TG curves of Al-PILCs (Tab. 3.5). The first weight loss below 350 °C of Al-PILCs is greater than that of Na-SWy-2. This difference is due to the loss of both physically adsorbed water and the dehydration of the chemical species that form the pillars as has been found for the Ti-PILCs materials.

In Fig. 3.4 the DTA curves exhibit an endothermic reaction near 120-130 °C, induced by dehydration, besides a second endothermic peak at about 650 °C assigned to dehydroxylation of both the clay structure and the aluminium pillars. The dehydroxylation temperature of this peak decreases to 488 °C for Al-PILC-600, expressing a reduced thermal stability at this temperature. This finding is supported by the decrease of SSA (Tab. 3.2). The dehydroxylation temperature of most Al-PILCs is lower by about 50 °C than that of Na-SWy-2. This decrease is also lower than that found in Ti-PILCs (100 °C), and can be explained by the condensation of the structural hydroxyl groups with Ti pillars (Han and Yamanaka, 1998 and 1997). An exothermic peak at 960 °C assigned to the recrystallisation of Al-PILCs was also observed.

Table 3.5: STA results of Al-PILCs and Na-SWy-2.

Samples	Dehydration temperature (°C)	Dehydroxylation temperature (°C)	Recrystallization temperature (°C)	Total water Content (%)
Na-SWy-2	128	690	945	9.3
Al-PILC-60	135	645	927	19.9
Al-PILC-200	131	646	928	16.8
Al-PILC-300	128	650	929	15.4
Al-PILC-400	126	651	930	13.0
Al-PILC-500	122	656	930	11.3
Al-PILC-600	119	488	931	9.0

3. Magnetic aluminium pillared clays (Al-M-PILCs)

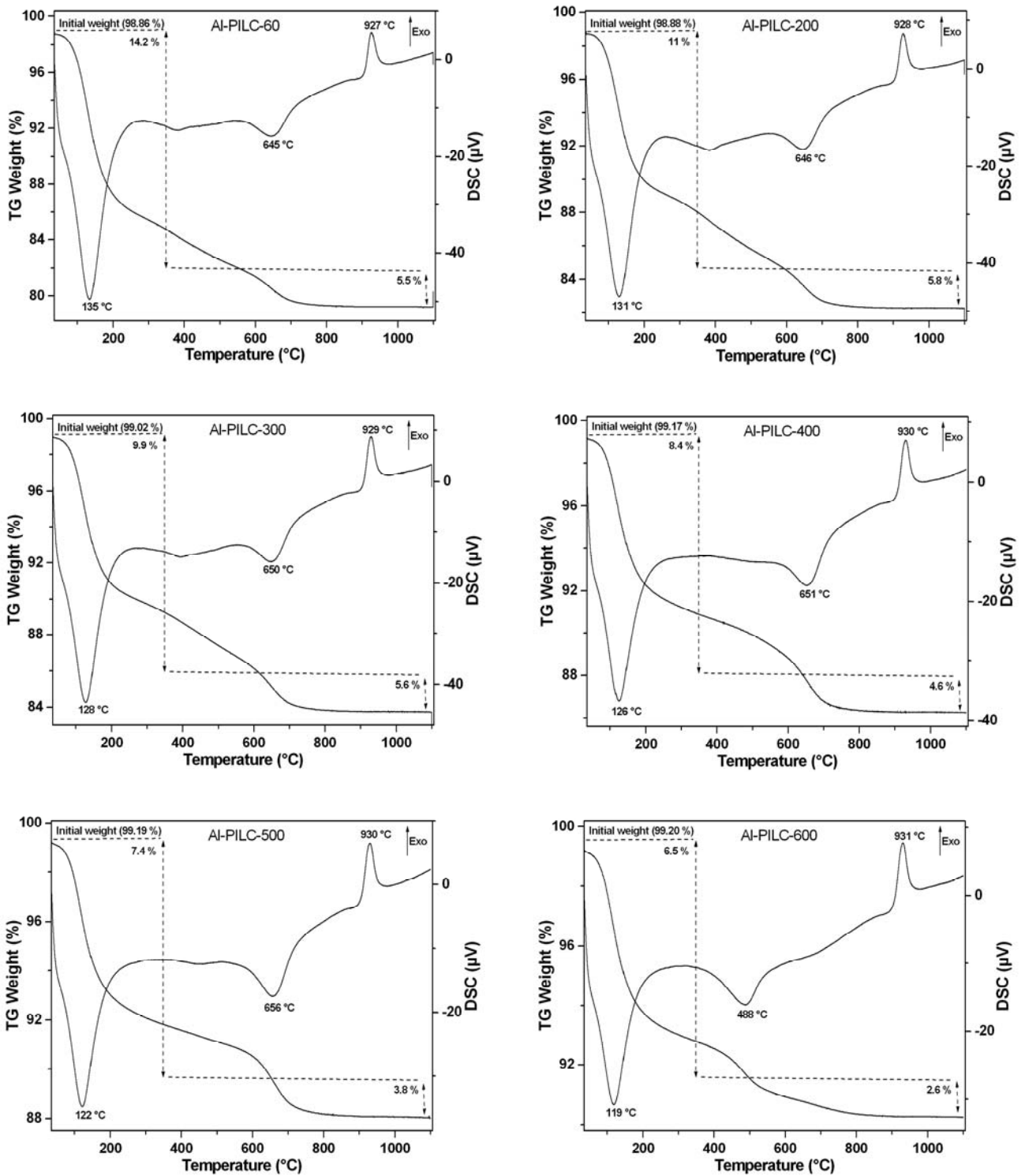


Figure 3.4: STA curves of Al-PILCs

3.1.5. Cation exchange capacity

The CEC of Al-PILCs was determined with copper-triethylenetetramine exchange according to Meier and Kahr (1999). The water content related to the dehydration was calculated from TG curves at temperature below 350 °C (Tab. 3.6).

The decrease of CEC after pillaring (Tab. 3.5) proves that the exchange of aluminium polycations has been established. CEC represented only the exchange of the residual interlayer cations mostly Na⁺, K⁺, Ca²⁺, and Mg²⁺. In addition, the low pH of Al-PILCs due essentially to the pH of the Al pillaring solution (3.9) can be related to the decrease of CEC (Table. 3.5). Indeed, at low pH the edges are saturated with protons, and therefore, are positively charged. Thus, the contribution of the edge-CEC in this case is excluded (Peigneur *et al.*, 1975, Lagaly, 1981, and Jasmund and Lagaly, 1993).

In contrast, in the case of Na-SWy-2 with high pH, the edges are negatively charged therefore about 20% of the CEC results from cations at crystal edges (Vogt and Köster, 1978).

Moreover, ICP-OES measurements were made in order to examine the origin of the CEC after pillaring with aluminium species, through the exchanged cations and aluminium content in the supernatant solution after copper-triethylenetetramine exchange. The data show that the aluminium was found in the supernatant along with low contents of Na⁺ and Mg²⁺. Thus, CEC represents the exchange of the residual Na⁺ and Mg²⁺ cations and aluminium monomers as suggested also by Lenoble *et al.*, (2002). The contribution of protons associated with aluminium polycations must, however, also be considered (Yamanaka and Brindley, 1979).

Table 3.6: CEC and water content of Al-PILCs

Samples	CEC (meq/100 g)	CEC reduction (%)	Water content* (%)	pH
Na-SWy-2	85		5.7	8.1
Al-PILC-60	47	45	14.3	4.8
Al-PILC-200	42	51	11.0	4.6
Al-PILC-300	40	53	9.9	4.7
Al-PILC-400	24	72	8.4	4.9
Al-PILC-500	18	79	7.4	4.9
Al-PILC-600	6	93	6.5	5.1

*: The water content at 35-350 °C determined from TG curves.

The decrease of CEC with increase calcination temperature can be related to the dehydration and dehydroxylation of aluminium polyoxycations upon heating. This fact is similar to the Hoffman Klemen effect (Hoffman and Klemen, 1950). After calcination, Al_2O_3 pillar oxides are formed. This reaction is accompanied by liberation of protons H^+ as explained in Chapter 2 (Section. 2.1.5). The interlayer H^+ ions move into the octahedral positions and the cation exchange capacity of the clay are thereby reduced (Cool and Vansant, 1998).

3.2. Magnetic aluminium pillared clays

3.2.1. XRD investigation

The values of the basal spacing of Al-M-PILCs are given in Tab. 3.7. The magnetization process caused a collapse of the basal spacing to values between 1.3-1.4 nm for the samples Al-M-PILCs except Al-M-PILC-600, which decreased to 1.24 nm (Fig. 3.5a). The XRD powder diffractograms (Fig. 3.5b) are lacking new peaks related to iron compounds. In addition, the (001) peak attributable to bayerite ($\text{Al}(\text{OH})_3$) disappeared for the samples Al-M-PILC-60, -200, and -300.

Table 3.7: d_{001} values of Al-M-PILCs.

Samples	d_{001} (nm)
Al-M-PILC-60	1.34
Al-M-PILC-200	1.40
Al-M-PILC-300	1.40
Al-M-PILC-400	1.42
Al-M-PILC-500	1.36
Al-M-PILC-600	1.24

3. Magnetic aluminium pillared clays (Al-M-PILCs)

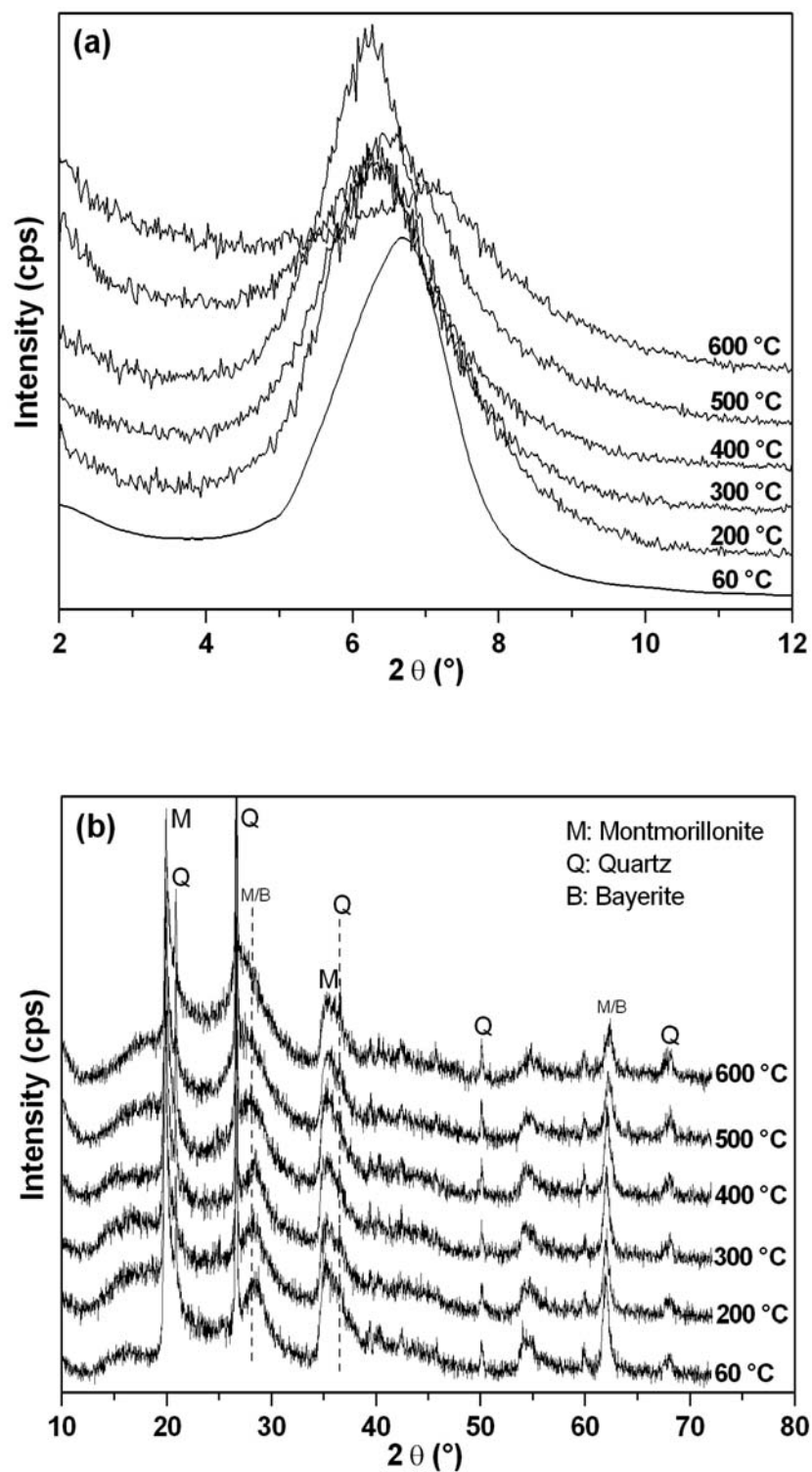


Figure 3.5: a) Oriented X-ray diffractograms of aluminium magnetic pillared clay and b) Powder X-ray diffractograms of Al-M-PILCs.

3.2.2. N₂ adsorption

SSA and Porosity

The SSA and porosity decrease after inserting the iron and the subsequent reduction by NaBH₄. This decrease is especially in the microporous range and was more pronounced in the case of Al-M-PILC-60, -200, and -300 (Tab. 3.8).

Table 3.8: Specific surface areas and pore volumes Al-M-PILCs.

Samples	SSA (m ² /g)	SSA reduction* (%)	V _{mp} (cm ³ /g)	V _{mes} (cm ³ /g)	V _p (cm ³ /g)	V _p reduction* (%)
Al-M-PILC-60	9	96	0.000	0.008	0.008	93
Al-M-PILC-200	16	93	0.000	0.014	0.014	87
Al-M-PILC-300	17	92	0.001	0.009	0.010	90
Al-M-PILC-400	37	80	0.003	0.027	0.030	71
Al-M-PILC-500	77	57	0.014	0.034	0.048	53
Al-M-PILC-600	74	42	0.016	0.029	0.045	29

*: Specific surface area and pore volume reduction after magnetization

Pore size distribution

The cumulative pore volume and the corresponding differential pore volume distribution curves of Al-M-PILCs at different temperatures were computed from the adsorption branch using the NLDFT method (Fig. 3.6).

At lower calcination temperatures (Al-M-PILC-60, -200, and -300) the magnetic samples present only a broad peak in the mesoporous range at about 3-7 nm. The peak corresponding to the microporous range disappears.

At higher calcination temperatures samples (Al-M-PILC-400, -500, and -600), the distribution displays two maxima: the first one at roughly 1.2 nm (microporous range), and the second one at a pore diameter of roughly 2.5-6.5 nm (mesoporous range). The latter maximum is broader and less intense than the corresponding curves forms of the Al-PILC samples. The magnetic aluminium pillared clays maintained to some extent both the micro- and the mesoporous structures at higher calcination temperature.

3. Magnetic aluminium pillared clays (Al-M-PILCs)

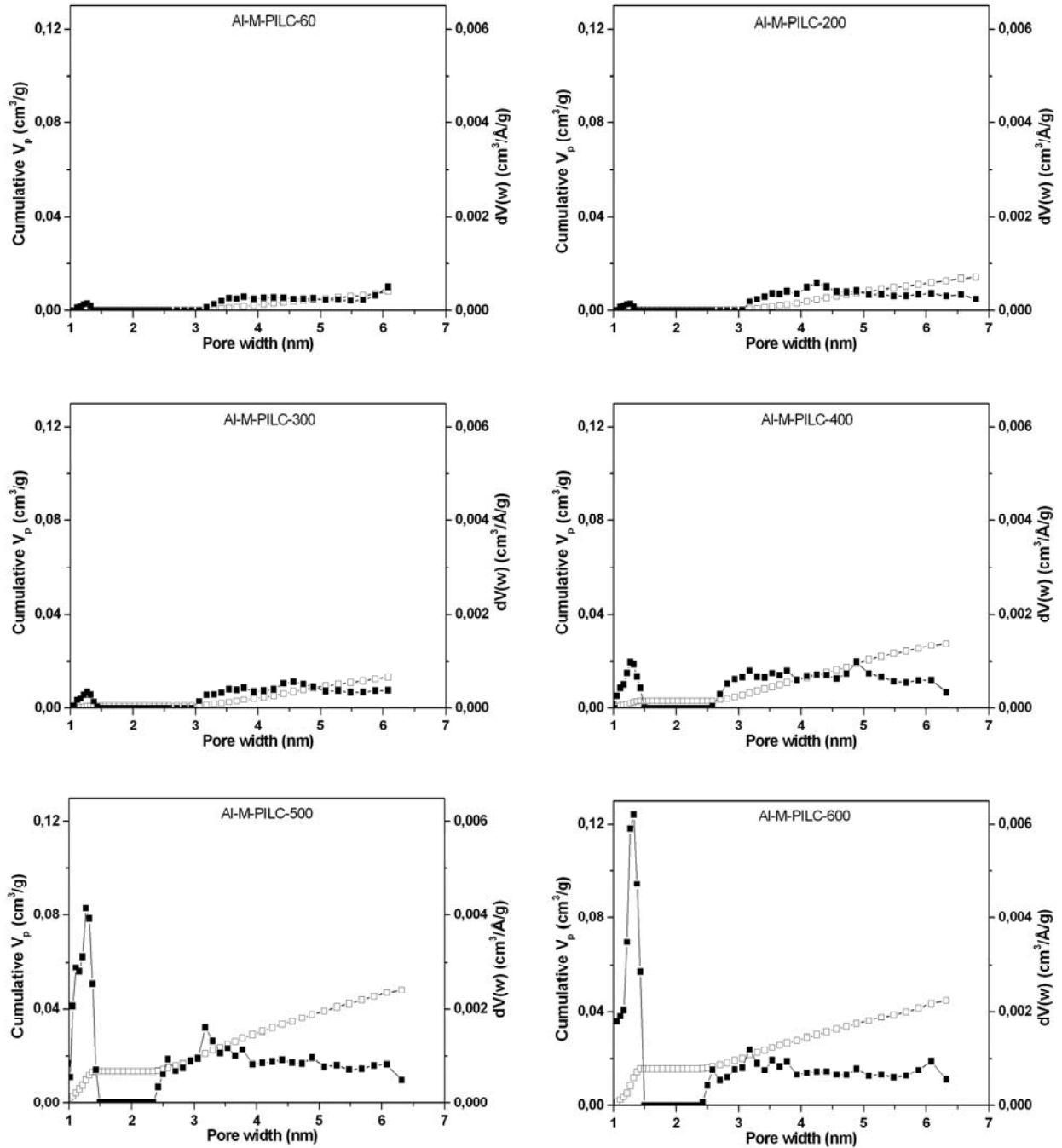


Figure 3.6: Pore size distribution of Al-M-PILCs. Full symbols/ right y-axis: differential pore volume distribution curves, open symbols/ left y-axis: cumulative pore volume curves.

3. Magnetic aluminium pillared clays (Al-M-PILCs)

N_2 isotherms

The results of the N_2 isotherms of the magnetic materials are shown in Fig. 3.7. The relative pressure axis is set to a linear and logarithmic scale in the left and right panels respectively. Except of those of Al-PILC-M-60, -200, and 300, the isotherms are of type IV which characterises the mesoporous materials (Sing *et al.*, 1985). Moreover, the hysteresis loop corresponds to type H4 in the IUPAC classification characteristics of materials with slit-like pores. As a result, the samples which have been initially calcined above 300 °C, show mesoporosity as is confirmed by the pore size distribution.

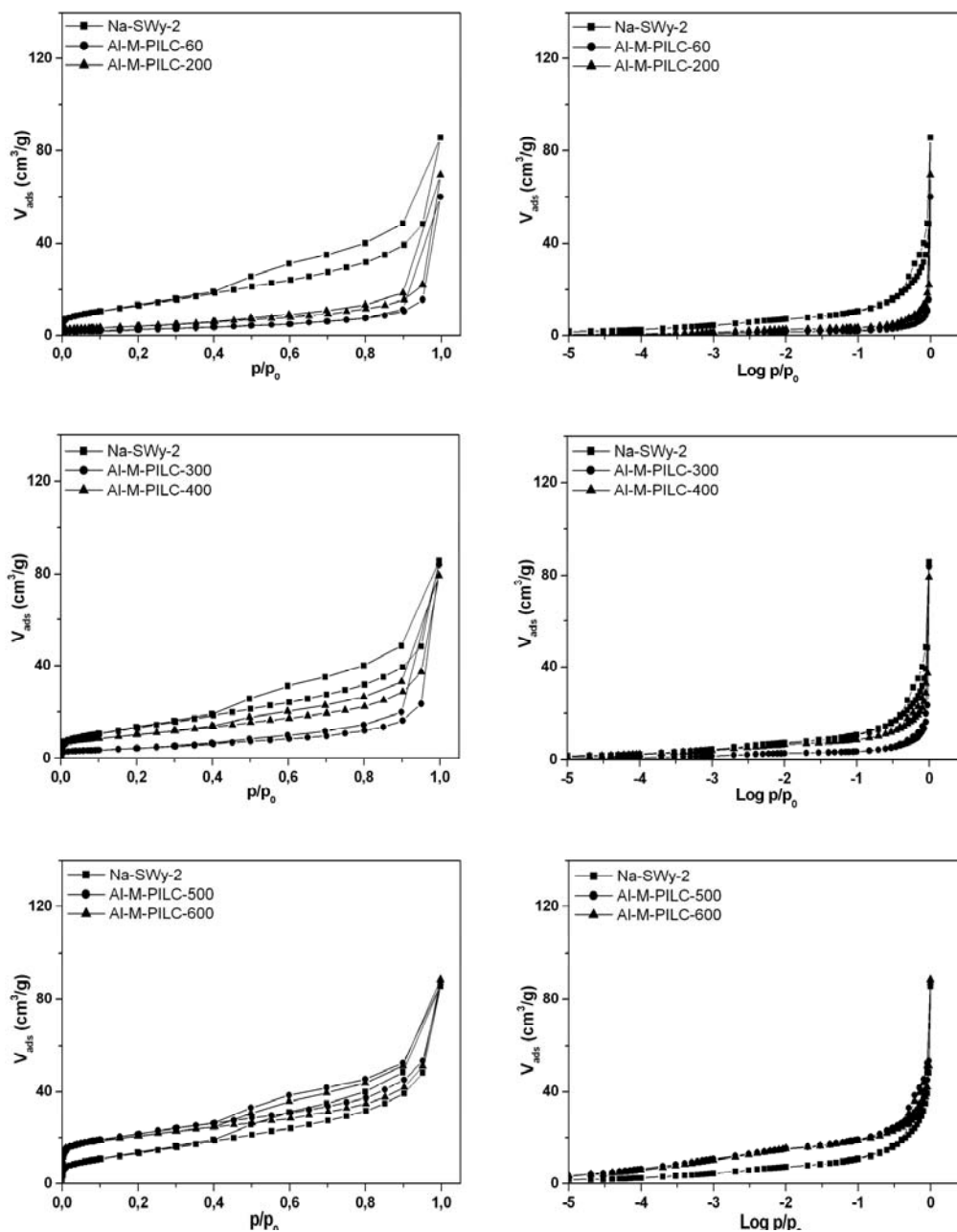


Figure 3.7: N_2 isotherms of Al-M-PILCs

3. Magnetic aluminium pillared clays (Al-M-PILCs)

3.2.3. X-ray fluorescence XRF

The results of the XRF analysis of the chemical composition of Al-M-PILCs are reported in Tab. 3.9. After the magnetization, the iron content increased. Note that the additional iron content of Al-M-PILCs samples is different for each sample. The samples Al-M-PILC-60, -200, -300, and -400 have higher additional iron content than Al-M-PILC-500 and -600.

Table 3.9: Fe₂O₃ and Al₂O₃ contents (%wt.) of Al-M-PILCs and Al-PILCs.

	Al-M- PILC-60	Al-M- PILC-200	Al-M- PILC-300	Al-M- PILC-400	Al-M- PILC-500	Al-M- PILC-600
Fe ₂ O ₃ [*]	3.93	3.85	4.06	3.58	2.35	1.53
Al ₂ O ₃ [#]	5.76	6.07	6.06	6.48	7.47	8.21
	Al- PILC-60	Al- PILC-200	Al- PILC-300	Al- PILC-400	Al- PILC-500	Al- PILC-600
Al ₂ O ₃ [#]	8.74	8.72	8.74	8.67	8.67	8.66
ΔAl ₂ O ₃	2.98	2.65	2.68	2.19	1.21	0.45

^{*}: Additional Fe₂O₃ content after magnetization based on the composition of Al-M-PILCs.

[#]: Additional content based on the composition of Na-SWy-2 given as g of Al₂O₃ per 100 g of Na-SWy-2.

ΔAl₂O₃: Difference in Al₂O₃ content (% PILCs- % M-PILCs).

3.2.4. FTIR investigation

FTIR-ATR investigation

As indicated in the previous Chapter (Section 2.2.4), the goal of using the ATR method is to investigate whether larger amounts of Fe-oxides are present on the outer surface. The band observed at 1062 cm⁻¹ (Fig. 3.8a) is related to the stretching of Si-O groups (Madejova and Komadel, 2001, and Farmer, 1974). A shift of this peak to lower wave number (1041 and 1009 cm⁻¹) with increasing calcination temperature has been observed. Here also, as we argued in Section 2.2.4, the dehydroxylation effect after calcination is possibly the reason for this shift. This statement can be deduced directly from the observed decrease of CEC (Tab. 3.5).

The weak band which appears at 796 cm⁻¹ could be interpreted as either the presence of traces of poorly crystalline silica (Si-O stretching of quartz and free silica) or the presence of Mg-Mg-OH vibrations. Two other weak bands at 776 and 684 cm⁻¹ for all Al-PILCs were assigned to the Si-O stretching of quartz, and Si-O group respectively.

3. Magnetic aluminium pillared clays (Al-M-PILCs)

Further identification of iron bands was not possible for Al-M-PILCs. This can be seen in Fig. 3.8b where no differences to the analysis presented in Fig. 3.8a can be detected.

Therefore, from these results, it can be assumed that well crystallized iron containing phases are not present on the outer surfaces of Al-M-PILCs.

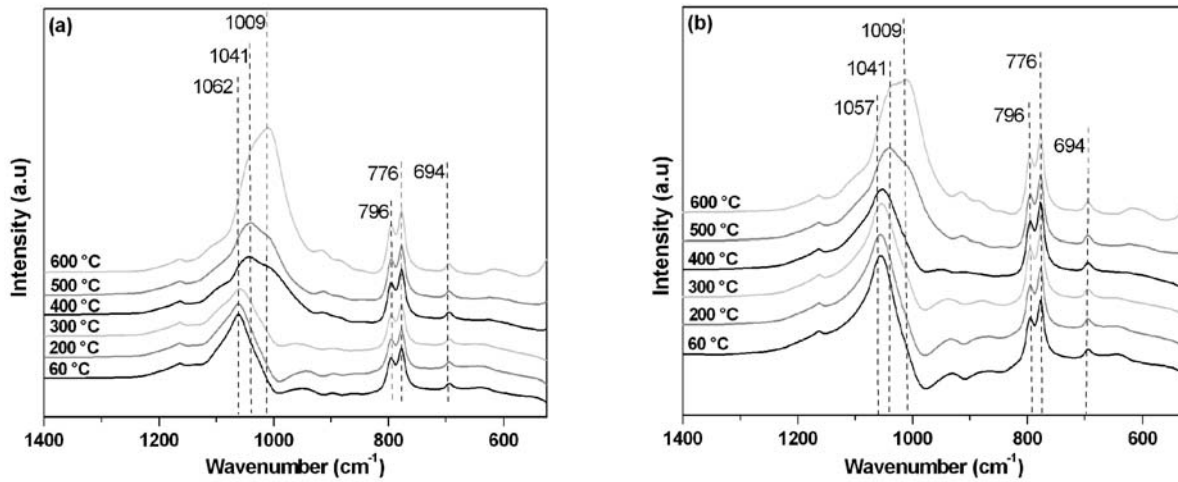


Figure 3.8: FTIR-ATR spectra of: a) Al-PILCs and b) Al-M-PILCs.

Far infrared spectroscopy

Fig. 3.9 presents the FIR spectra of Al-M-PILCS compared with those of the references (magnetite, hematite, Na-SWy-2, and Na-SWy-2-hematite). The spectra of Al-M-PILC-60, -200, and -400 indicate the presence of magnetite and/or maghemite together with traces of hematite. However, the spectra of Al-M-PILC-300, -500, and -600 do not show the presence of well defined iron phases.

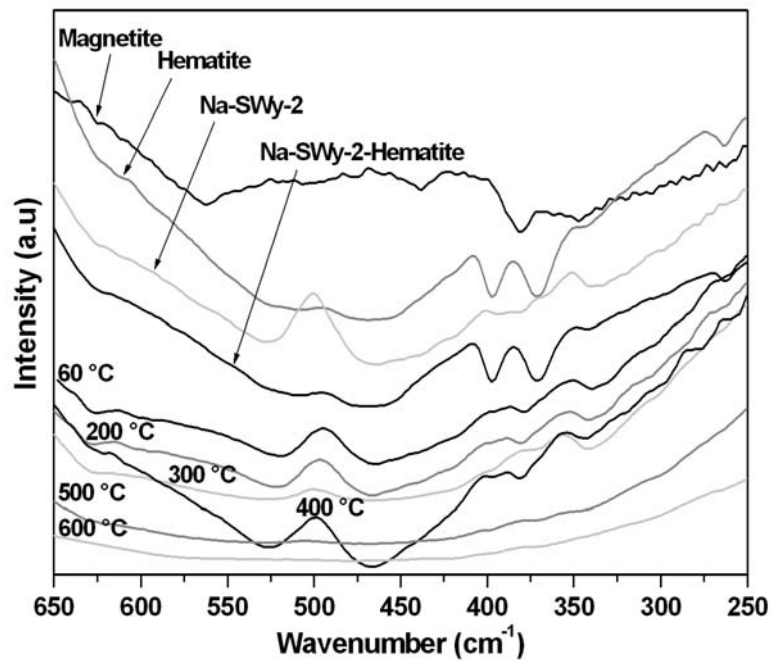


Figure 3.9: FIR spectra of Al-M-PILCs, hematite, magnetite, Na-SWy-2, and Na-SWy-2-hematite.

3.2.5. Magnetic properties

On the basis of the previous results of Al-M-PILCs supported by XRD, N₂ adsorption, and XRF analysis we selected the samples Al-M-PILC- 200, -400, and -500 for further magnetic investigation. The magnetic properties of the above samples were recorded by a SQUID magnetometer.

Hysteresis curves (2, 5, 10, 50, 100, and 300 K)

The hysteresis curves of the three measured samples in the full range (left side) and zoom (right side) are presented in Fig. 3.10. All samples exhibit hysteresis at all temperatures, whereas hysteresis area was smallest for sample Al-M-PILC-500 (Fig. 3.10g).

3. Magnetic aluminium pillared clays (Al-M-PILCs)

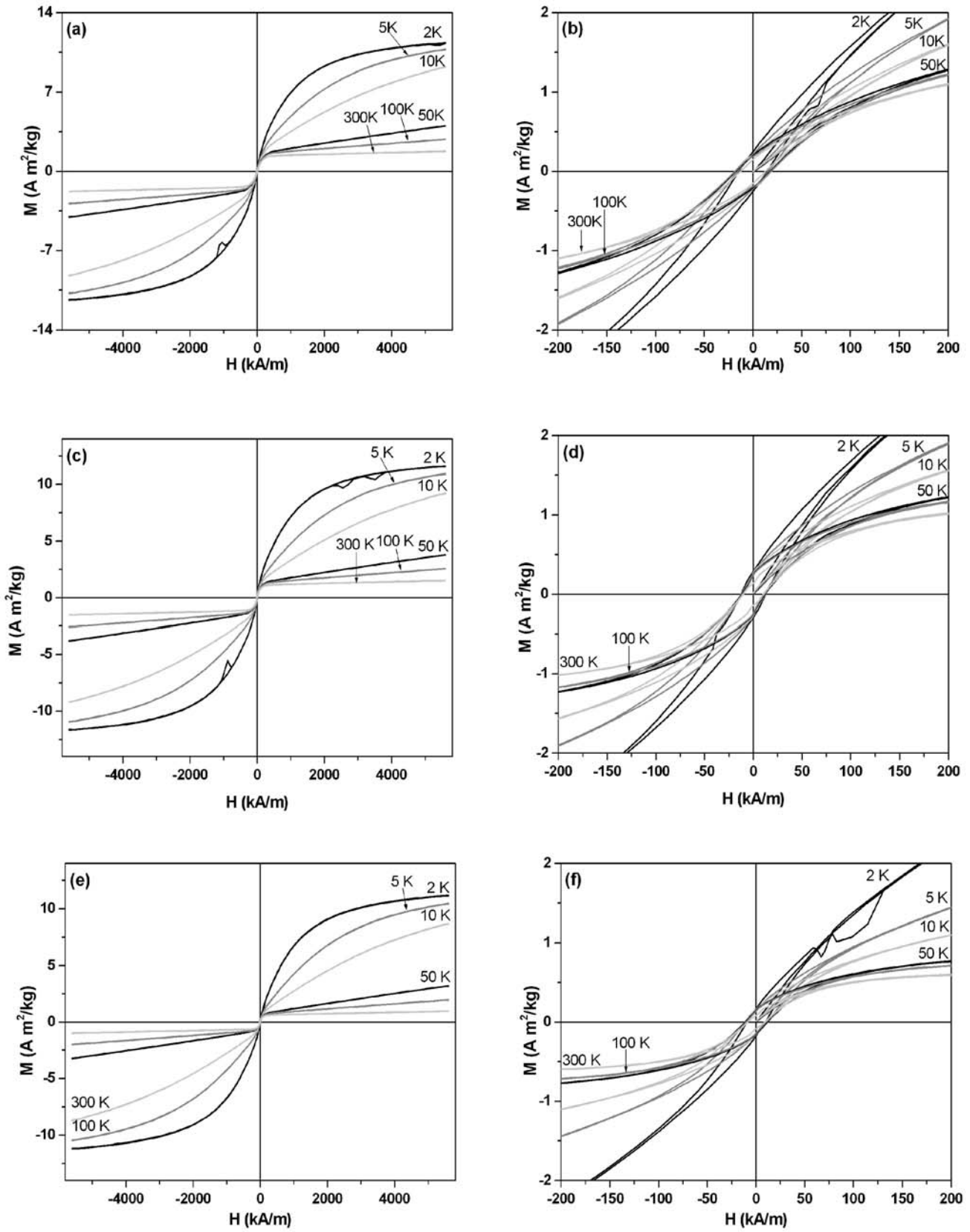


Figure 3.10: Hysteresis loops of Al-M-PILC-200 (a, b), Al-M-PILC-400 (c, d), and Al-M-PILC-500 (e, f), full range (left side) zoomed in (right side).

3. Magnetic aluminium pillared clays (Al-M-PILCs)

Temperature dependency of hysteresis parameters

The variations of the hysteresis parameters of Al-M-PILCs as a function of the SQUID measurement temperature are presented in Fig. 3.11. The values of M_s , M_{rs} , and H_c increase with decreasing temperature. However, the value of the M_{rs}/M_s ratio increases as the temperature increases.

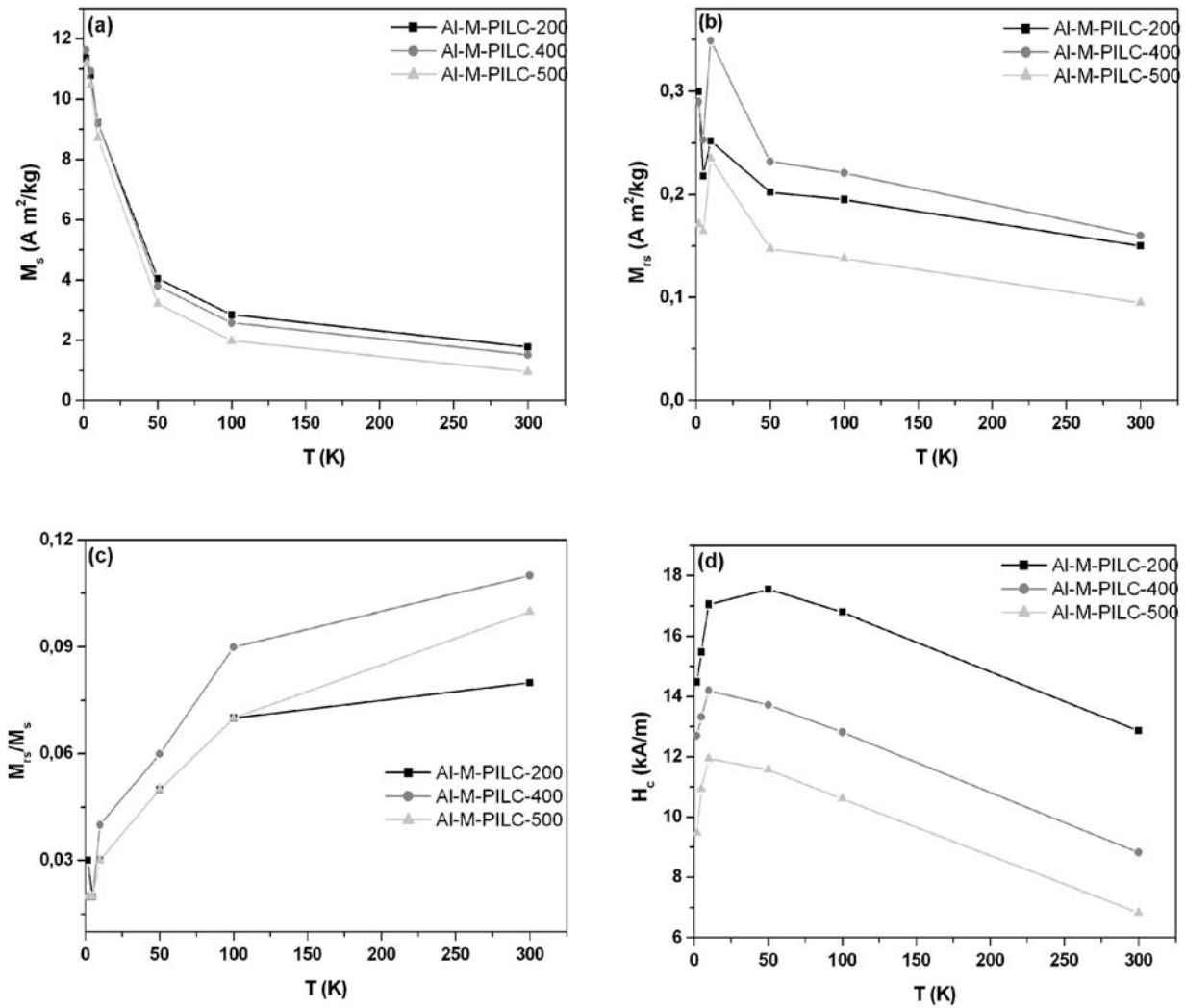


Figure 3.11: Temperature dependency of a) M_s , b) M_{rs} , c) M_{rs}/M_s , and d) H_c of Al-M-PILCs.

3. Magnetic aluminium pillared clays (Al-M-PILCs)

Saturation magnetization at room temperature

The values of M_s of the materials not measured by SQUID (Al-M-PILC-60, -300, and -600) were determined by AGM measurement at room temperature.

The computed values of M_s of Al-M-PILCs (Tab. 3.10) were then compared to the known values of M_s for magnetite, maghemite, iron metal and Fe_xB (Moskowitz, 1991, and Zhang *et al.*, 2001). This suggests then that the latter phases are present in the sample. The presence of a poorly ordered iron alloy has, however, also to be taken into account.

Table 3.10: Specific saturation magnetization of Al-M-PILCs at 300 K.

Samples	Fe₂O₃^{added} (Wt %)	M_s (A m²/kg added iron)
Al-M-PILC-60	3.93	26*
Al-M-PILC-200	3.85	46
Al-M-PILC-300	4.06	37*
Al-M-PILC-400	3.58	42
Al-M-PILC-500	2.35	41
Al-M-PILC-600	1.53	30*
Magnetite Fe ₃ O ₄		90-92
Maghemite γ -Fe ₂ O ₃		60
Iron Fe		218
Fe _x B		~60

*: Measured by AGM

Magnetic domain status

The M_{rs}/M_s - H_{cr}/H_c diagram at 300 K of the measured samples is compared with that obtained for magnetite by Muskowitz (1991) (Fig. 3.12). From this comparison, though it is only valid for magnetite both Al-M-PILC-200 and -500 exhibit PSD state, Al-M-PILC-400 can be MD.

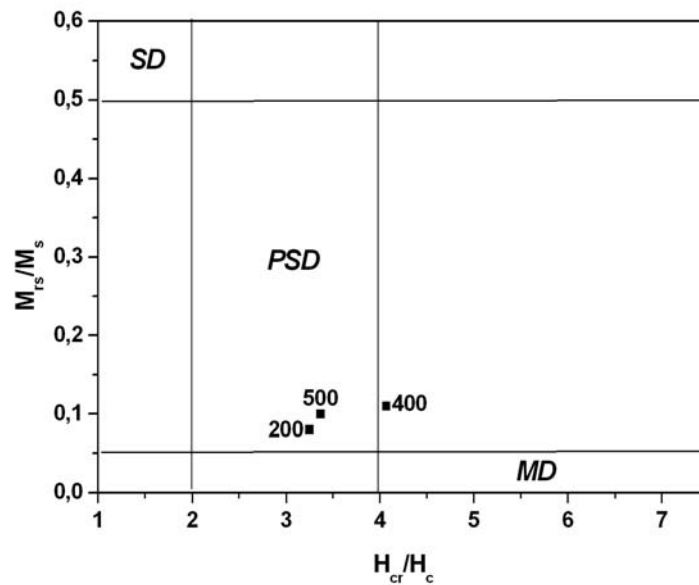


Figure 3.12: M_{rs}/M_s - H_{cr}/H_c diagram of Al-M-PILCs at 300 K. Domain classification after Moskowitz, (1991).

ZFC/FC investigation

Similarly to the case of Ti-M-PILC-400 discussed in the previous chapter (Section 2.2.5), the ZFC/FC curves of the three measured samples (Al-M-PILC-200, -400, and -500) present a very shallow distribution of blocking temperatures, and are dominated by a paramagnetic behaviour (Fig. 3.13). The slight differences between ZFC and FC are indicative of the presence of non-paramagnetic contributions.

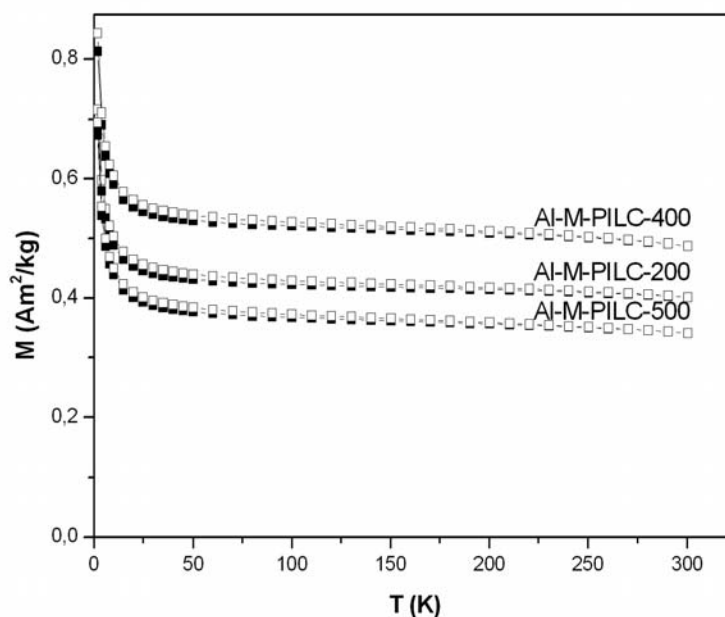


Figure 3.13: ZFC/FC curves of Al-M-PILC. Full symbols ZFC, open symbols FC curves.

3. Magnetic aluminium pillared clays (Al-M-PILCs)

Curie-Weiss law: Determination of θ and C

The values of the Weiss constant, θ , and the Curie constant, C, are reported in Tab. 3.11.

On one hand, the negative sign of θ indicates that all the Al-M-PILCs behave as ferrimagnetic materials. On the other hand, the samples have almost the same values of C.

Table 3.11: Parameters of the Curie-Weiss-law of Al-M-PILCs.

Samples	θ (K)	$C*10^6$ (m³ K/kg)	R²
Al-M-PILC-60	n.d	n.d	n.d
Al-M-PILC-200	-1.6	26.8	0.991
Al-M-PILC-300	n.d	n.d	n.d
Al-M-PILC-400	-1.5	29.1	0.983
Al-M-PILC-500	-1.3	27.3	0.988
Al-M-PILC-600	n.d	n.d	n.d

θ : Weiss constant and C: Curie constant

n.d: not determined.

3.2.6. Mössbauer spectroscopy

The Mössbauer spectroscopy data for the Al-M-PILCs were recorded at room temperature and at 2.7 K. Besides the paramagnetic Fe³⁺ doublet of SWy-2 (Fig. 3.14), the spectra of all Al-M-PILCs samples measured at room temperature also contain a minor ferrous doublet. Thus the ferric iron is partially reduced.

The spectra of all Al-M-PILC samples exhibit besides the ferric and ferrous doublets a very broad background component which contributes to the adsorption between approximately ± 5 mm/s. This feature is identified as a magnetically split sextet caused probably by FeB-alloys (Van Wontergehm *et al.*, 1986). Moreover, a minor indication of a sextet was also observed for the sample which has been calcined initially at 200 °C. Furthermore, the high local variation in the composition presumably results in the absence of the resolved lines in the sextet for most samples. The composition may include both B and Al in the alloy.

The Fe²⁺/Fe³⁺ ratio is decreasing with increasing calcination temperature (Tab. 3.12).

Furthermore, the spectra of Al-M-PILC-200, -400, and 500 at 2.7 K (Fig. 3.15) are characterized by a distribution of relaxation times. The fast relaxation gives rise to two doublets. The slow one leads to a sextet, which is characteristic by the magnetic ordering. In addition, no evidence for metallic iron is found.

Table 3.12: Fe²⁺/Fe³⁺ ratios, isomer shift (IS) and quadrupole splitting (QS) determined by Mössbauer spectroscopy of Al-M-PILCs.

Samples	Fe ²⁺ /Fe ³⁺	Fe ²⁺	Fe ²⁺	Fe ³⁺	Fe ³⁺
	ratio	IS (mm/s)	QS (mm/s)	IS (mm/s)	QS (mm/s)
Al-M-PILC-60	0.37	1.14	2.81	0.35	0.74
Al-M-PILC-200	0.25	1.33	2.46	0.28	0.89
Al-M-PILC-300	0.25	1.12	2.79	0.35	0.74
Al-M-PILC-400	0.17	1.17	2.87	0.36	0.79
Al-M-PILC-500	0.10	1.25	2.39	0.32	0.87
Al-M-PILC-600	0.08	1.14	2.40	0.34	1.06

3. Magnetic aluminium pillared clays (Al-M-PILCs)

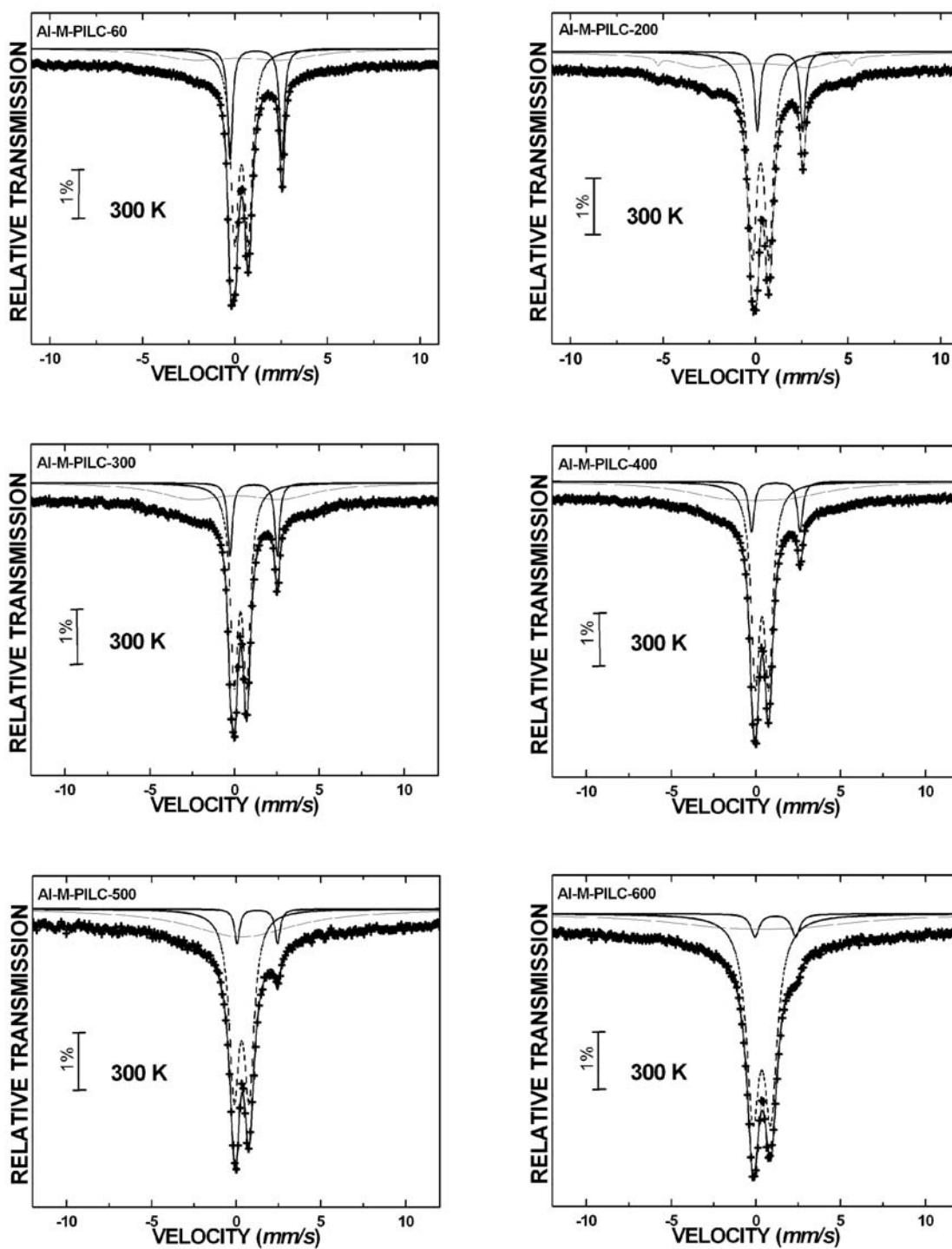


Figure 3.14: Mössbauer spectra of Al-M-PILCs at room temperature.

3. Magnetic aluminium pillared clays (Al-M-PILCs)

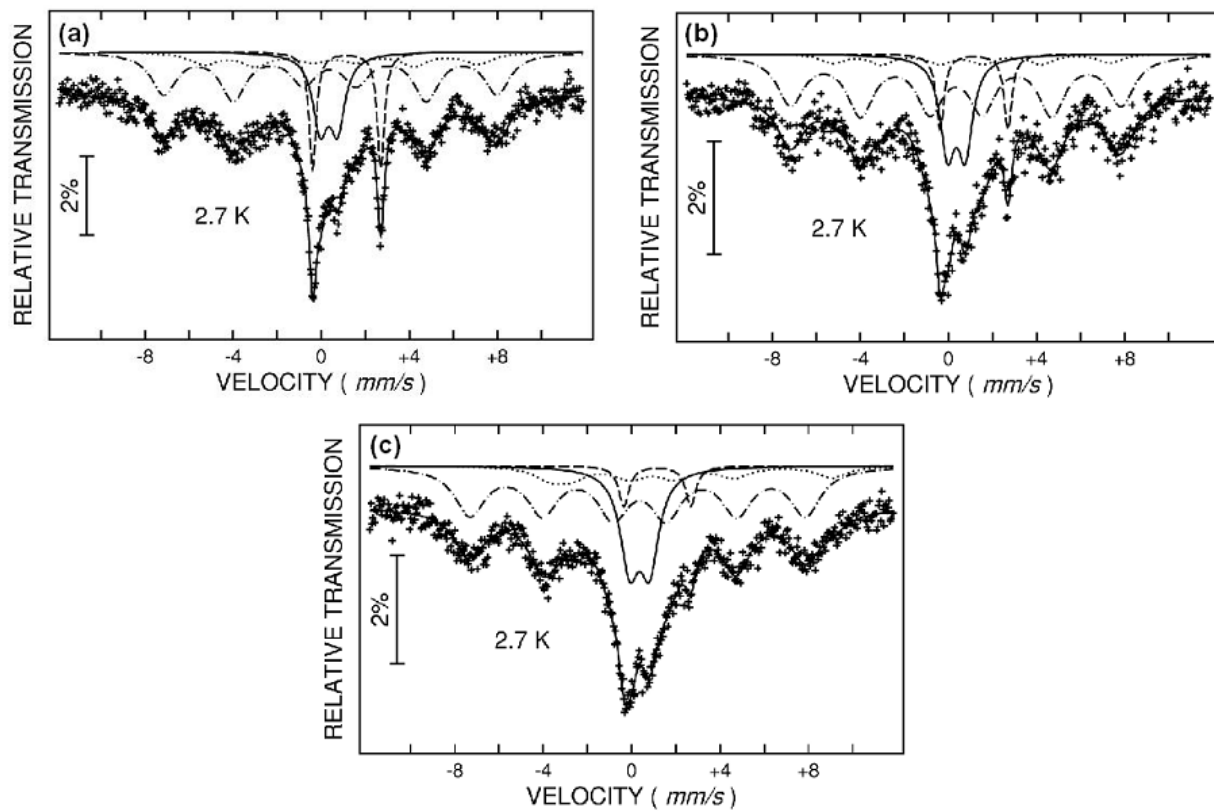


Figure 3.15: Mössbauer spectra 2.7 K of a) Al-M-PILC-200, b) Al-M-PILC-400, and c) Al-M-PILC-500.

3.3. Discussion

During the reduction process, where Fe^{3+} is initially reduced to Fe^{2+} using NaBH_4 as reducing agent, the original structure of Al-PILCs was affected. The change in the Al-PILC structure is caused by the reduction of the initial Fe^{3+} in octahedral positions upon treatment with sodium borohydride as reported by Rozenson and Heller-Kallai (1976). Hence, this reduction led to the partial deterioration of the Al-PILC-structure. This deterioration was more pronounced for the samples calcined at lower temperatures (60, 200, and 300°C). Therefore, this resulted in lower stability and the collapse of the basal spacing accompanied by the disappearance of the peak attributed to bayerite (Fig. 3.5). This collapse leads to a higher loss in SSA and porosity, especially microporosity (Tab. 3.8).

As in the case of Ti-PILC, the calcination temperature influences the textural properties of the materials such as the SSA, the porosity and the stability of the Al-PILCs. Nevertheless, the materials do not behave similarly on the magnetization process, where the adsorption of Fe and reduction by NaBH_4 occurs.

Though the amounts of additional iron of Al-M-PILCs samples (Tab. 3.10) were different, the calculated M_s values were quite similar. Therefore, almost all M_s values support the presence of magnetite, maghemite phases and FeB-alloy.

For the samples Al-M-PILC-60, -200, and -400 the FIR spectra reveal the presence of magnetite and/or maghemite and hematite phases.

The Mössbauer study revealed the presence of both Fe^{2+} and Fe^{3+} iron. Note that the calculated ratios are lower than 0.5, which is the characteristic value for stoichiometric magnetite. Moreover, the negative sign of the Weiss constant θ supports the presence of a ferrimagnetic phase.

Based on the above arguments in this study we assume the presence of a poorly ordered iron-boron alloy. This assumption has been also taken into consideration in the case of Ti-M-PILCs. Since we know the dimension of the interlayer space, which, in the case of Al-M-PILC, is around 0.8 nm, we expect the particle sizes of the additional iron containing alloys to be of the same order. Another supposition could be that these iron-alloy particles turn to be stretched within the interlayer space. The resulting structure is a thin flat entity. This suggestion can be supported by the very broad and shallow distribution of the ZFC/FC of the three measured samples Al-M-PILC-200, -400, and 500. To explain this feature, the separating TOT-layers have to be considered. The latter can hinder the formation of well ordered magnetic domains in these units and hence lead to the observed paramagnetic

3. Magnetic aluminium pillared clays (Al-M-PILCs)

FC/ZFC behaviour of measured samples. But ferrimagnetic contributions are better developed for the 200 °C samples than for the 400 °C and 500 °C calcined sample.

The results of the Mössbauer analysis show that the samples Al-M-PILC-200, -400, and -500 exhibit a beginning of magnetic ordering at 2.7 K. The sextet is better developed for the sample calcined at 200°C. All three samples have the highest saturation magnetization.

Furthermore, the results of the textural properties of the material after the magnetization process show higher relative loss in porosity and specific surface area. This is indeed more accentuated at lower calcination temperatures.

Another important finding is the correlation between specific surface area reductions (Tab. 3.6), the difference in aluminium content $\Delta\text{Al}_2\text{O}_3$ (Tab. 3.9), and the filling factor FF (Tab. 3.13). The loss of SSA is proportional to the loss in Al_2O_3 (Fig. 3.16). The initially low calcined samples (60, 200, 300, and 400 °C) have the highest losses. In addition, the filling factor FF of these samples is decreasing after magnetization from 0.5 to 0.2 on average. This means that after magnetization on average out of five layers only one layer is intercalated with aluminium pillars, thus leading to a partial collapse of the pillared structure.

The higher calcined samples exhibited the higher stability against the magnetization process, which destabilizes the pillar structure. In the sample Al-M-PILC-500 the highest SSA and pore volume was maintained.

Table 3.13: FF and IF of Al-PILCs and Al-M-PILCs

Samples	V_p (cm^3/g)	$V_{\text{IL}}^{\text{the}}$ (cm^3/g)	$V_{\text{IL}}^{\text{exp}}$ (cm^3/g)	FF	IF
Al-PILC-60	0.115	0.339	0.150	0.4	2
Al-PILC-200	0.106	0.246	0.140	0.6	2
Al-PILC-300	0.104	0.298	0.139	0.5	2
Al-PILC-400	0.103	0.287	0.125	0.4	2
Al-PILC-500	0.103	0.261	0.125	0.5	2
Al-PILC-600	0.063	0.257	0.085	0.3	3
Al-M-PILC-60	0.008	0.142	0.031	0.2	5
Al-M-PILC-200	0.014	0.164	0.038	0.2	4
Al-M-PILC-300	0.010	0.164	0.034	0.2	5
Al-M-PILC-400	0.03	0.172	0.046	0.3	4
Al-M-PILC-500	0.048	0.149	0.067	0.4	2
Al-M-PILC-600	0.045	0.104	0.066	0.6	2

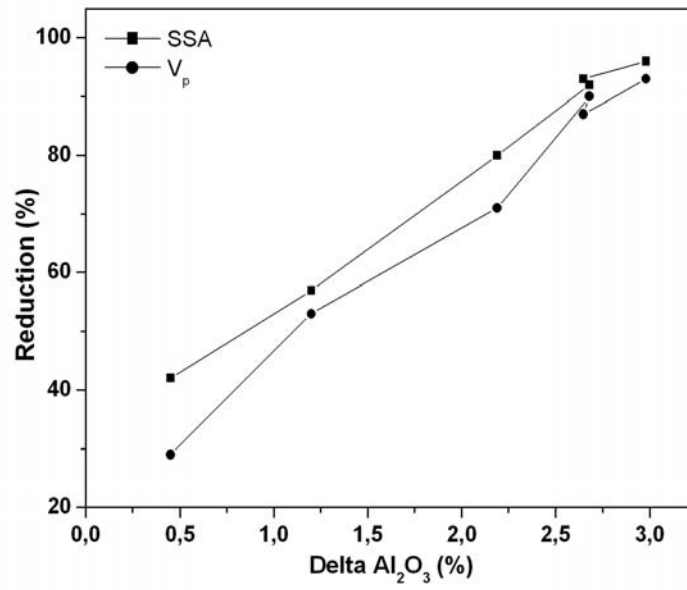


Figure 3.16: Correlation between the ΔAl_2O_3 and the SSA and V_p reduction.

4. Magnetic zirconium pillared clays (Zr-M-PILCs)

The starting material was Na-SWy-2 having a specific surface area (SSA) of 50 m²/g, a basal spacing d_{001} = 1.24 nm, and a cation exchange capacity (CEC) of 85 meq/100 g of clay. The zirconium pillared clays Zr-PILCs were prepared using a freshly made 0.1 M ZrOCl₂.8H₂O as pillaring solution (Yamanaka and Brindley, 1979, Ben Chaabene *et al.*, 2004). The intercalated zirconium montmorillonite was prepared by slow addition with stirring of corresponding amounts of prepared pillaring solution to the Na-SWy-2 suspension in order to obtain 10 mmol Zr/g of clay. The mixture was stirred for 24 h. The solids were separated by centrifugation, washed with distilled water and dried at 60 °C. The intercalated solids were calcined at different temperatures (200, 300, 400, 500 and 600 °C) for 2 h at a heating rate of 1 °C/min from room temperature up to the calcination temperature. The corresponding zirconium pillared clays Zr-M-PILCs were obtained after the insertion of the iron and the subsequent reduction by NaBH₄ at room temperature (Zhang and Manthiram, 1996). The same sample notation has been adapted as in the case of titanium materials.

4.1. Zirconium pillared clays

4.1.1. XRD investigation

The oriented XRD patterns of the obtained zirconium pillared montmorillonite obtained for various temperatures are shown in Fig. 4.1a. The basal spacing for each sample is given in Tab.4.1.

Table 4.1: d_{001} values of Zr-PILCs.

Samples	d_{001} (nm)
Zr-PILC-60	1.83
Zr-PILC-200	1.63
Zr-PILC-300	1.61
Zr-PILC-400	1.56
Zr-PILC-500	1.50
Zr-PILC-600	1.14

4. Magnetic zirconium pillared clays (Zr-M-PILCs)

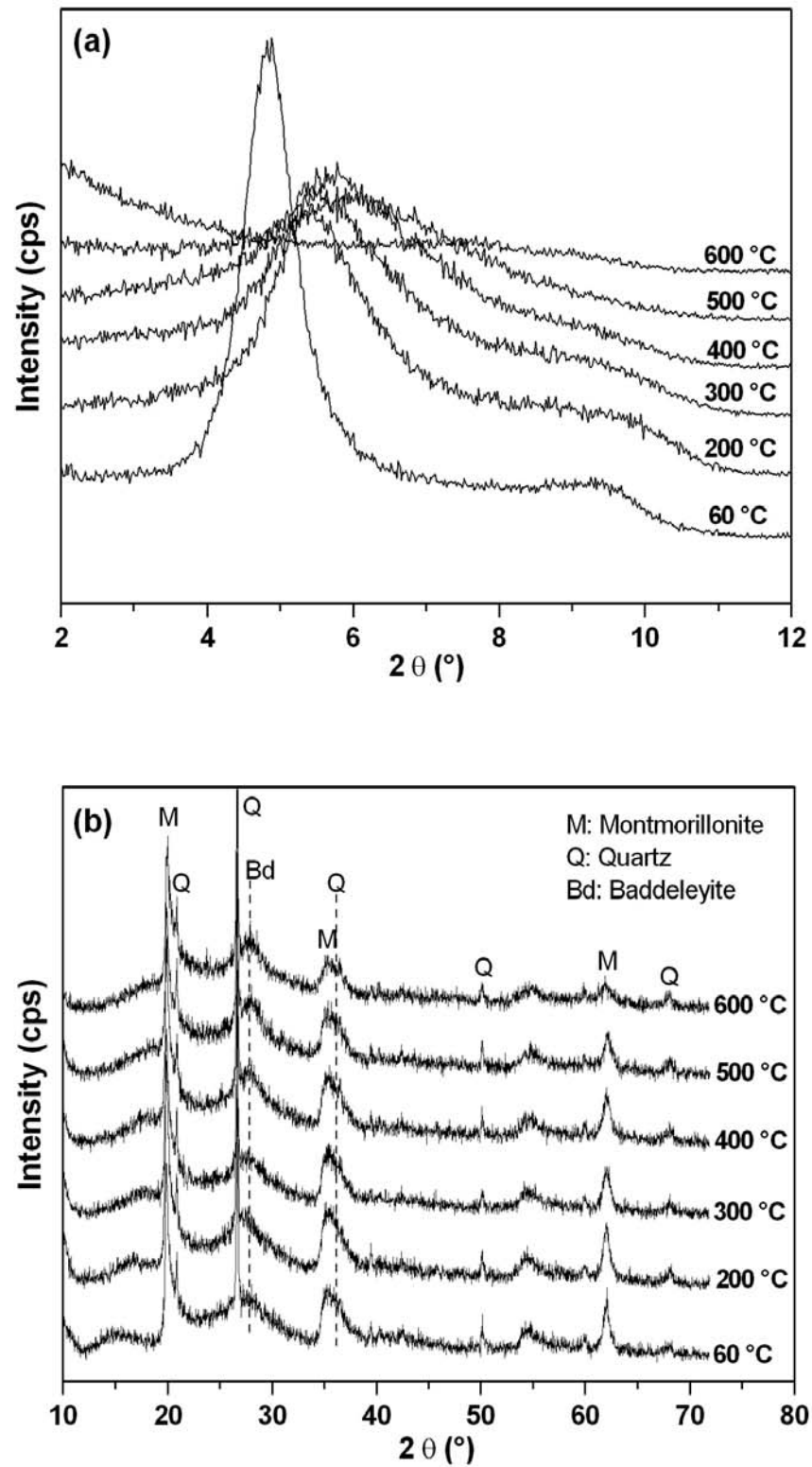


Figure 4.1: a) Oriented X-ray diffractograms of zirconium pillared clay dried at 60 °C and calcined at various temperatures and b) Powder X-ray diffractograms of Zr-PILCs.

4. Magnetic zirconium pillared clays (Zr-M-PILCs)

The parent clay Na-SWy-2 has a reflection at around $7^\circ 2\theta$ with basal spacing of 1.24 nm. This diffraction peak in Fig. 1a has shifted to lower $^\circ 2\theta$ values for all samples except Zr-PILC-600 indicating an expansion in the layer structure as a result of pillaring. A d-value of 1.85 nm is found for Zr-PILC-60. At higher temperatures, the d-value decreased with increasing calcination temperature to reach 1.60 nm for Zr-PILC-200 and -300, and 1.50 for Zr-PILC-400 and -500. A second peak at around $9.5^\circ 2\theta$ decreases in intensity upon increasing calcination temperature. The presence of this peak can be interpreted as the diffraction line (002) of Zr-PILCs as has been suggested in the Ti-PILCs and Al-PILCs materials.

At all calcination temperatures, the powder diffractograms contain peaks of montmorillonite and quartz. Another peak at around $28^\circ 2\theta$, can be attributed to the diffraction line (-111) of Baddeleyite (ZrO_2) which slightly decreases in intensity upon increase in heat treatment (Fig. 4.1b). The full width at half maximum of baddeleyite β was calculated using TOPAS 3.0 provided by Bruker AXS, this calculation was done after normalisation to the intensities relative to the quartz peak. As shown in Tab. 4.2, β increases with calcination temperature reflecting the low crystallinity of baddeleyite at higher temperature. Simultaneously, the average crystallite size, D, computed from the Scherrer equation (Jenkins and Vries, 1970) decreases from 7.4 nm to values between 4.9 and 5.8 nm for calcination temperatures higher than 60°C .

Table 4.2: D and β values of Baddeleyite for Zr-PILCs

Sample	Zr-PILC-60	Zr-PILC-200	Zr-PILC-300	Zr-PILC-400	Zr-PILC-500	Zr-PILC-600
β	1.230	1.620	1.830	1.710	1.710	1.570
D (nm)	7.4	5.5	4.9	5.3	5.3	5.8

4.1.2. N₂ adsorption

SSA and porosity

Tab. 4.3 presents the values of specific surface areas, SSA, and pore volumes adsorbed at P/P₀ 0.7, V_p, as well as meso-, and micropore volumes. All samples show higher surface areas and porosity than the raw material Na-SWy-2 which has SSA=50 m²/g. Thereafter the SSA decreased with higher temperatures. Heating at 600 °C decreases SSA to 68 m²/g. This behaviour was accompanied by the decrease in pore volume mostly in micropore volume indicating a low thermal stability of the Zr-PILCs clay at this temperature.

Table 4.3: Specific surface areas and pore volumes of Zr-PILCs.

Samples	SSA (m ² /g)	V _{mp} (cm ³ /g)	V _{mes} (cm ³ /g)	V _p (cm ³ /g)
Zr-PILC- 60	201	0.066	0.031	0.097
Zr-PILC- 200	175	0.051	0.042	0.093
Zr-PILC- 300	166	0.046	0.045	0.091
Zr-PILC- 400	145	0.036	0.046	0.082
Zr-PILC- 500	105	0.022	0.041	0.063
Zr-PILC- 600	68	0.009	0.037	0.046

SSA: specific surface area, V_p: pore volume at P/P₀ = 0.7 (pore width ≤ 7 nm), V_{mp}: micropore volume, V_{mes}: mesopore volume.

Pore size distribution

The NLDFT differential pore volume (Fig. 4.2, Full symbols) show that for all samples, distribution presents two peaks, one maximum roughly at 14 Å (microporous range), and the other peak, broader and with low intensity value at about 20-65 Å (mesoporous range). The microporosity decreases, thus the intensity of the first peak decreases upon heat treatment. The cumulative pore volume (Fig. 4.2, open symbols) shows two steps, each associated with one of the two major pore distribution peaks.

4. Magnetic zirconium pillared clays (Zr-M-PILCs)

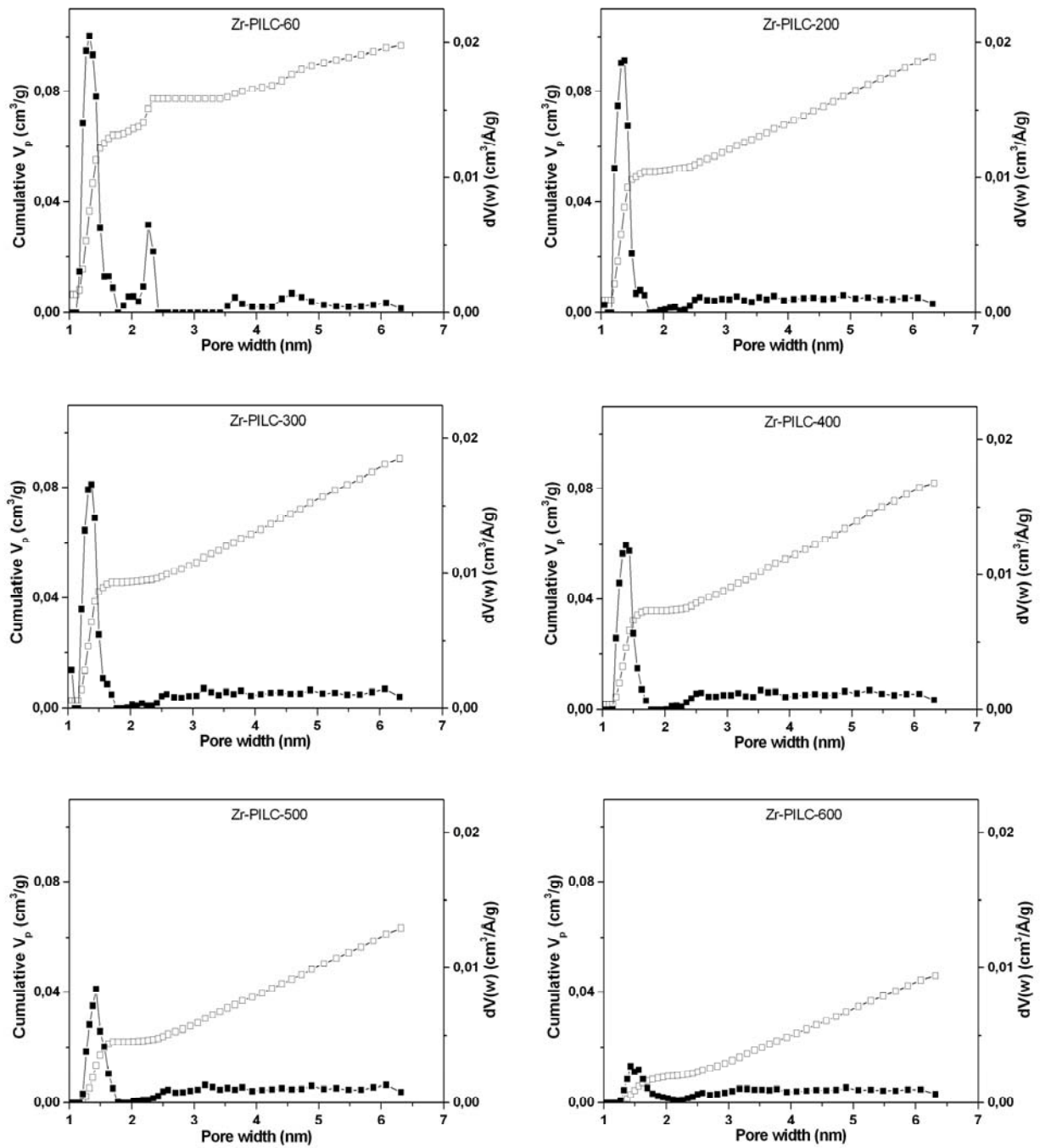


Figure 4.2: Pore size distribution of Zr-PILCs. Full symbols: differential pore volume distribution curves, open symbols: cumulative pore volume curves.

N₂ isotherms

To examine the forms of the isotherms and their loop hysteresis which are related to the pore nature the N₂ isotherms of Zr-PILCs compared with that of Na-SWy-2 in linear and logarithmic relative pressure scales are illustrated in Fig. 4.3. An increase of the adsorbed volume was obtained for all Zr-PILCs comparing with the original clay. The logarithmic isotherm curves show an increase of the adsorbed volumes at $p/p_0 < 0.1$. At this relative pressure range, the corresponding linear curves of Zr-PILCs present type I isotherm reflecting the presence of micropores. At $P/P_0 > 0.1$, the isotherm shapes correspond to type IV (Sing *et al.*, 1985, Lowell *et al.*, 2006) characteristic of mesoporous materials. The presence of mesoporosity is supported by the existence of hysteresis loops in all samples. The isotherm of the parent clay Na-SWy-2 has also hysteresis property, due essentially of the orientation of layers themselves as highlighted in Chapter 2 (Section 2.1.2.). In all cases, the hysteresis loop corresponds to type H4 in the IUPAC classification and this is characteristic of material with narrow slit-like pores.

The nitrogen analyses results speak in favour of the presence of both micro- and mesoporosity. At lower temperatures the microporosity is more dominant than the mesoporosity, upon calcination at temperatures above 400 °C the mesoporosity is more dominant.

In general term, the reduction in the surface areas and micropore volumes of PILCs upon increasing the calcination temperatures could be due to the changes in the Hoffman Klemen effect, i.e. heating causes irreversible migration of small cations to the vacant octahedral sites in the clay layers and partial collapse of the structure occurs (Romero *et al.* 2006). According to Valverde *et al.* (2002 and 2003) the main reason for the reduction in the surface area (mainly the microporous area) at high temperatures is the dehydroxylation and sintering occurring within the structure of the pillared clays.

4. Magnetic zirconium pillared clays (Zr-M-PILCs)

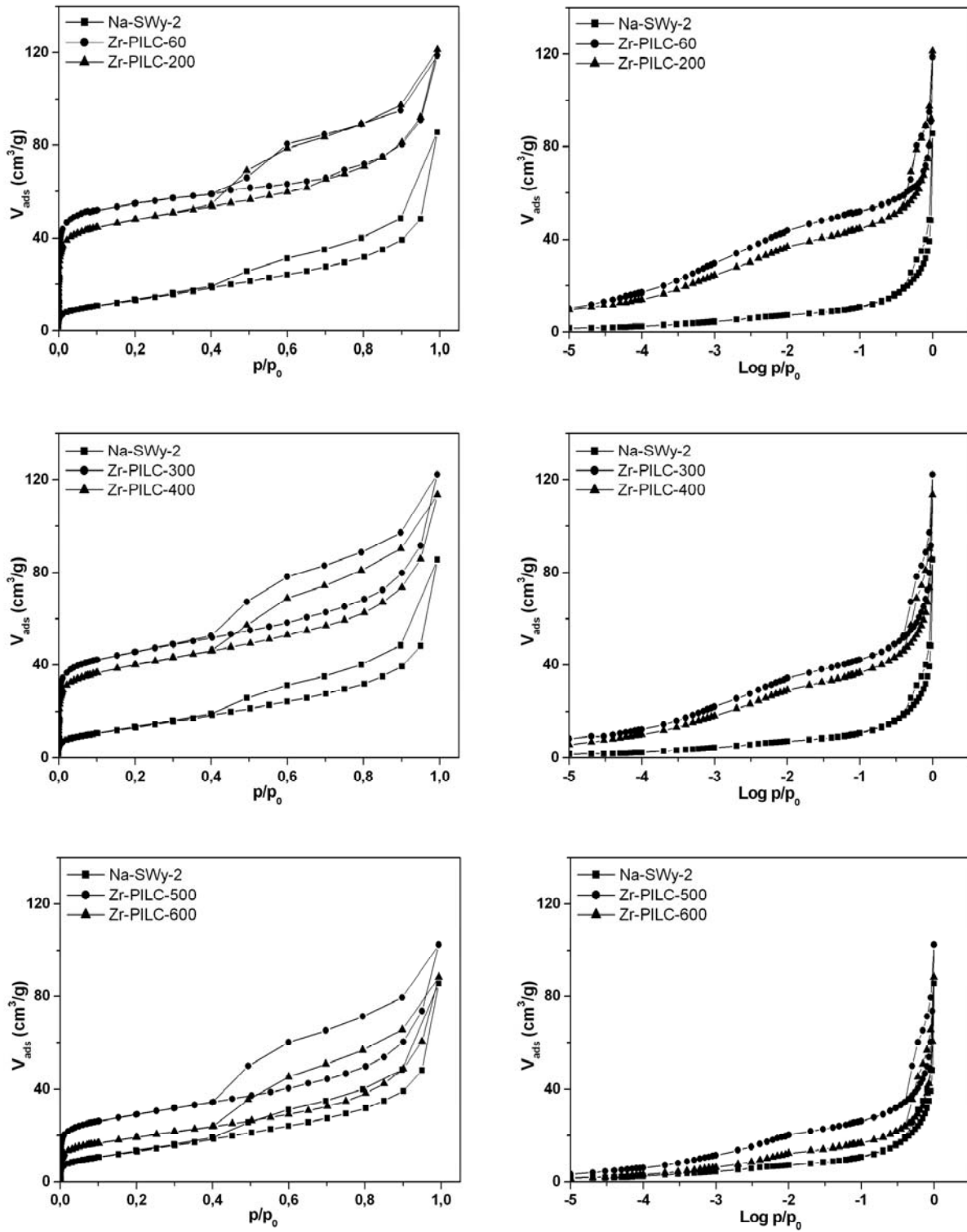


Figure 4.3: N₂ isotherms of Zr-PILCs

4. Magnetic zirconium pillared clays (Zr-M-PILCs)

4.1.3. X-ray fluorescence XRF

Tab. 4.4 collects the chemical composition of Zr-PILCs. These materials contain about 10-13 % of ZrO₂, due to the pillaring with zirconium. The data indicate also that essentially all the sodium ions were exchanged with zirconium polycations.

The LOI decreases with increasing heat treatment, as has been found for Al-PILCs and Ti-PILCs.

Table 4.4: Chemical composition reported as oxides (%wt.) of Na-SWy-2 and Zr-PILCs.

Oxides	Na-SWy-2	Zr-PILC-60	Zr-PILC-200	Zr-PILC-300	Zr-PILC-400	Zr-PILC-500	Zr-PILC-600
SiO ₂	60.42	50.25	52.29	53.47	54.13	56.00	57.03
Al ₂ O ₃	19.79	16.58	17.23	17.69	17.93	18.52	18.86
Fe ₂ O ₃	3.99	3.36	3.49	3.59	3.63	3.76	3.83
MnO	0.01	b.d	b.d	b.d	b.d	b.d	b.d
MgO	2.34	1.83	1.90	1.95	1.98	2.07	2.11
CaO	0.13	0.07	0.08	0.08	0.08	0.08	0.08
Na ₂ O	2.21	b.d	b.d	b.d	b.d	b.d	b.d
K ₂ O	0.11	0.06	0.06	0.06	0.06	0.06	0.07
TiO ₂	0.11	0.10	0.11	0.11	0.11	0.11	0.12
P ₂ O ₅	0.02	0.02	0.02	0.02	0.02	0.03	0.02
SO ₃	0.02	b.d	b.d	b.d	b.d	b.d	b.d
ZrO ₂	n.p	11.38	11.89	12.21	12.40	13.01	13.27
LOI	10.85	16.14	12.71	10.59	9.43	6.14	4.37

b.d: below detection limit.

n.p: not present.

4.1.4. Simultaneous thermal analysis

The obtained pillared samples show high initial weight losses, which gradually decrease at higher temperatures (Fig. 4.4). This decreasing trend was also highlighted by XRF analysis and can be explained on the basis of the partial loss of the swelling properties of the clay after calcination (Mishra and Rao, 2005).

The loss of both physically adsorbed water and the dehydration of the chemical species that form the pillars especially between 36 and 350 °C caused a great total weight loss of Zr-PILCs (Tab. 4.5).

Two endothermic reactions have been also observed in Zr-PILCs DTA curves (Fig. 4.4), the first one near 110-140 °C and the second one at about 635 °C assigned to dehydration and dehydroxylation of both the clay structure and the pillars, respectively. As in regard to the second reaction, on one hand, the dehydroxylation temperature decreases for Zr-PILC-600. This fact shows that Zr-PILCs are less thermally stable at 600 °C, which is in agreement with the XRD and nitrogen adsorption results. On the other hand, the dehydroxylation temperature is lower than that of Na-SWy-2. These behaviours were also observed in Al- and Ti-PILCs. The zirconium oxide pillars formed can be condensed with the structural hydroxyl groups as suggested by Han and Yamanaka, (1997 and 1998).

Table 4.5: STA results of Zr-PILCs and Na-SWy-2.

Samples	Dehydration temperature (°C)	Dehydroxylation temperature (°C)	Recrystallisation 1 temperature (°C)	Recrystallisation 2 temperature (°C)	Total water Content (%)
Na-SWy-2	128	690	n.p	945	9.3
Zr-PILC-60	137	630	882	928	19.3
Zr-PILC-200	131	631	886	928	16.4
Zr-PILC-300	131	633	886	928	13.3
Zr-PILC-400	118	635	884	928	10.5
Zr-PILC-500	112	648	886	929	8.3
Zr-PILC-600	110	475	886	929	6.8

n.p: not present

4. Magnetic zirconium pillared clays (Zr-M-PILCs)

All Zr-PILCs present two exothermic behaviours at 890 °C and 930 °C related to the recrystallisation of structure. The first exothermic peak is observed only in the zirconium materials. The partial recrystallisation in a low temperature range can be explained by the low thermal stability of these materials. The surface area and basal spacing of Zr-PILC-600 (Fig. 4.1 and Tab. 4.1, respectively) show also a strong decreasing trend.

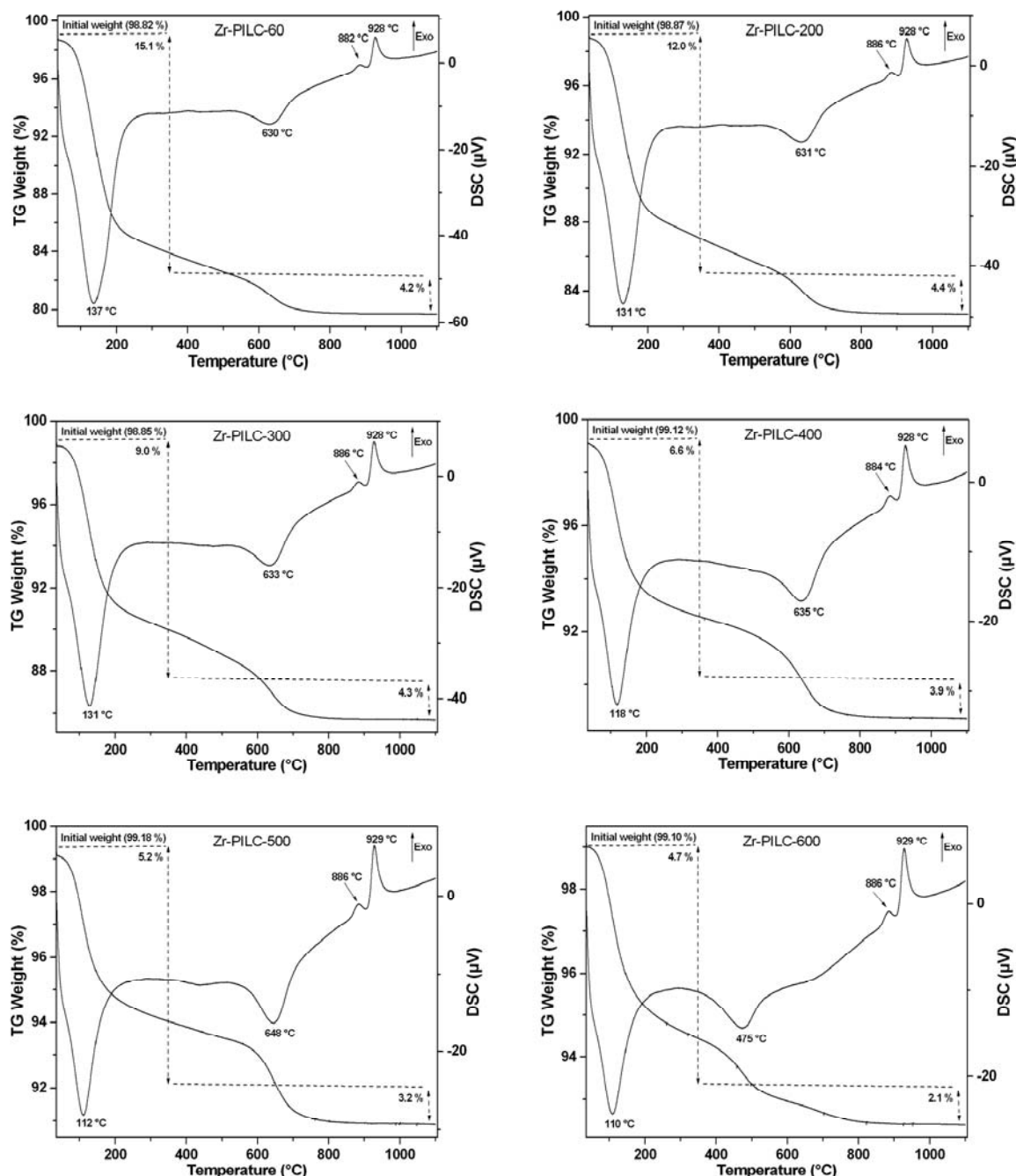


Figure 4.4: STA curves of Zr-PILCs

4.1.5. Cation exchange capacity

The values of the CEC measured by the copper-triethylenetetramine exchange (Meier and Kahr, 1999) of Zr-PILCs are presented in Tab. 4.6. A decrease of CEC after pillaring (Tab. 4.4) was observed. In order to check the origin of CEC as well as the irreversibility of cationic exchange, ICP-OES was used to investigate the exchanged cations and zirconium content in the supernatant solution after CEC reaction. The data show that no zirconium is found after calculation in meq/100 g and only low CEC values of Na⁺ and Mg²⁺ are obtained. Thus, a part of CEC represented the exchange of the residual interlayer cations mostly Na⁺ and Mg²⁺. It seems most likely that protons associated with Zr polycations contribute to the total CEC as suggested by Yamanaka and Brindley, (1979).

The influence of pH on the CEC must be also considered as signaled in the case of Ti-PILCs and Al-PILCs. The low pH of Zr-PILCs (Tab. 4.4) is due essentially to the initial pH of the zirconium pillaring solution which was 1.20. Thus, the edge CEC is not considered in contrast to the unpillared clay Na-SWy-2. Other observed behaviour is the decrease of the CEC for higher calcination temperature. This behaviour is due to the migration of H⁺ ions from the interlayer positions to the octahedral sheet and thereafter the CEC is reduced as explained in Chapter 2 (Section 2.1.5).

Table 4.6: CEC and water content of Zr-PILCs

Samples	CEC (meq/100 g)	CEC reduction (%)	Water content* (%)	pH
Na-SWy-2	85	0	5.7	8.1
Zr-PILC-60	55	35	15.1	4.7
Zr-PILC-200	51	40	12.0	4.2
Zr-PILC-300	48	44	9.0	4.1
Zr-PILC-400	25	71	6.6	4.1
Zr-PILC-500	9	89	5.2	4.7
Zr-PILC-600	8	91	4.7	5.0

*: The water content at 35-350 °C determined from TG curves.

4.2. Magnetic zirconium pillared clays

4.2.1. XRD investigation

Fig. 4.5a shows the oriented diffractograms of zirconium pillared clays. The corresponding d_{001} spacing of these samples is collected in Tab. 3.7. After iron exchange and NaBH_4 reduction, a collapse of the basal spacing was obtained.

From the powder diffractograms (Fig. 4.5b), no new peaks corresponding to iron compounds are observed.

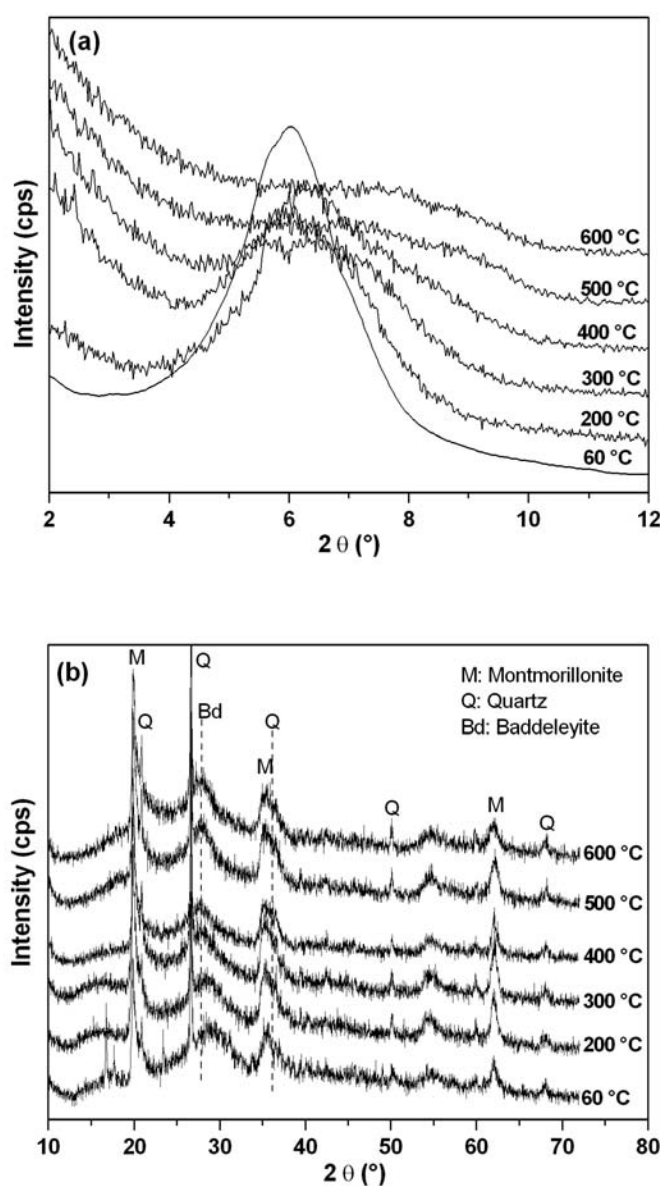


Figure 4.5: a) Oriented X-ray diffractograms of zirconium magnetic pillared clay and b) Powder X-Ray diffractograms of Zr-M-PILCs.

4. Magnetic zirconium pillared clays (Zr-M-PILCs)

Table 4.7: d_{001} values of Zr-M-PILCs.

Samples	d_{001} (nm)
Zr-M-PILC-60	1.47
Zr-M-PILC-200	1.42
Zr-M-PILC-300	1.45
Zr-M-PILC-400	1.40
Zr-M-PILC-500	1.20
Zr-M-PILC-600	1.11

4.2.2. N_2 adsorption

SSA and Porosity

The values of SSA and pore volume regrouped in Tab. 4.8 are decreased. The magnetisation process affects the pillared structure. This behaviour was more pronounced in the case of Zr-M-PILC-60 and Zr-M-PILC-200. These materials exhibit no microporosity. The sample Zr-M-PILC-300 presented the highest SSA and porosity.

Table 4.8: Specific surface areas and pore volumes of Zr-M-PILCs

Samples	SSA (m^2/g)	SSA reduction* (%)	V_{mp} (cm^3/g)	V_{mes} (cm^3/g)	V_p (cm^3/g)	V_p reduction* (%)
Zr-M-PILC-60	4	98	0.000	0.003	0.003	97
Zr-M-PILC-200	10	94	0.000	0.008	0.008	91
Zr-M-PILC-300	123	26	0.029	0.041	0.070	23
Zr-M-PILC-400	81	44	0.014	0.040	0.054	34
Zr-M-PILC-500	43	59	0.003	0.030	0.033	48
Zr-M-PILC-600	33	51	0.001	0.024	0.025	46

*: Specific surface area and pore volume reduction after magnetization

Pore size distribution

The NLDFT cumulative pore volume and the corresponding differential pore volume distribution curves of Al-PILCs are depicted in Fig. 4.6. Samples Zr-M-PILC-60 and -200 present no pore size distribution. In contrast, for Zr-M-PILC-300 and -400 the pore volume can be seen to accumulate around a micro- type pore, with a maximum at 1.4-1.5 nm and a meso-type pore with broader peak about 2.0-6.5 nm.

4. Magnetic zirconium pillared clays (Zr-M-PILCs)

The same peaks were obtained in the case of Zr-M-PILC-500 and -600 with lower intensity. Thus, magnetic zirconium pillared clays have both mesoporous and microporous structure for higher calcination temperature.

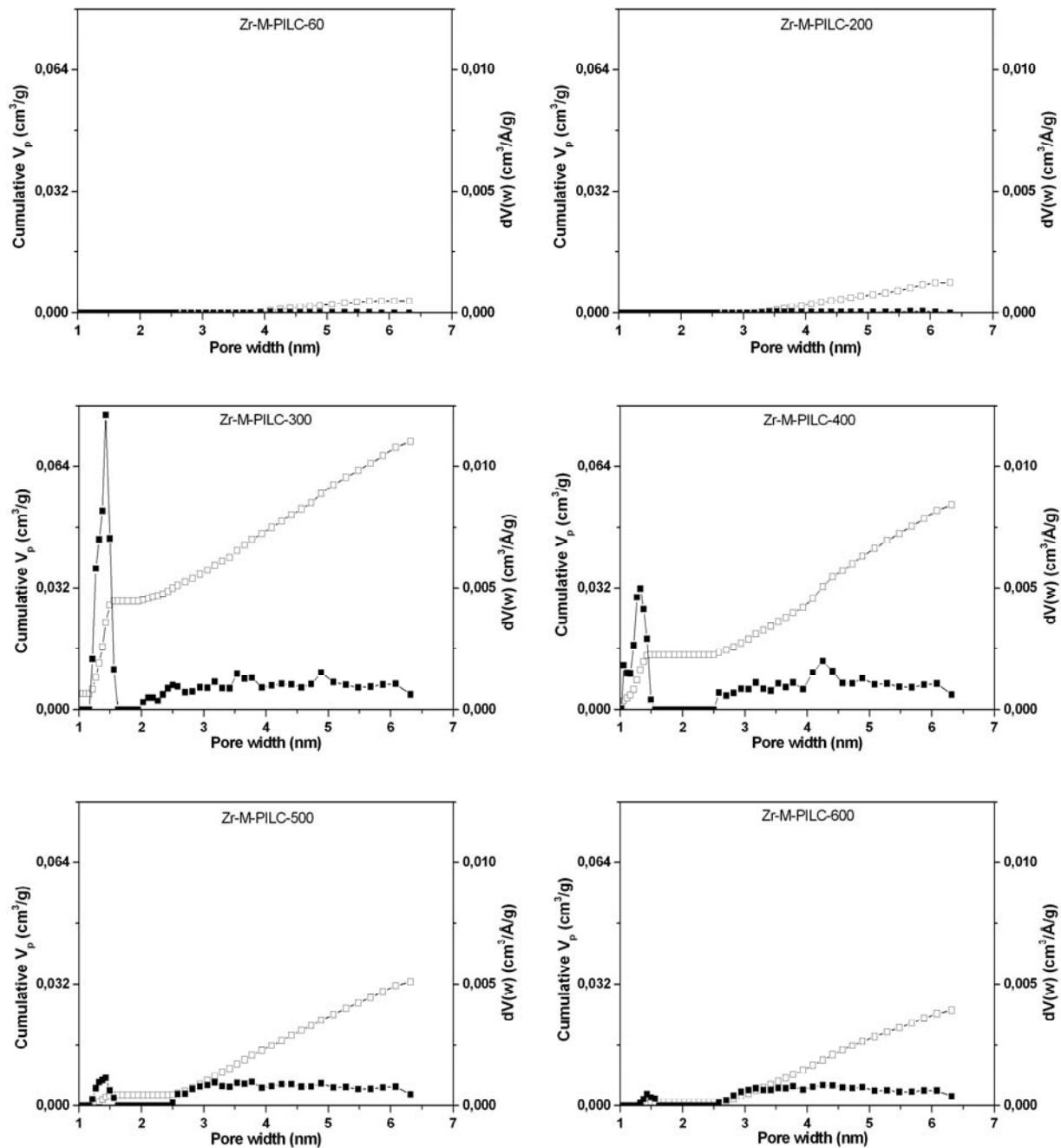


Figure 4.6: Pore size distribution of Zr-M-PILCs. Full symbols/ right y-axis: differential pore volume distribution curves, open symbols/ left y-axis: cumulative pore volume curves.

4. Magnetic zirconium pillared clays (Zr-M-PILCs)

N₂ isotherms

Fig. 4.7 shows the N_2 isotherms of Zr-M-PILCs compared with the Na-SWy-2 and presented in the linear and logarithmic relative pressure x-axis. As a result of the insertion of zirconium pillars followed by the magnetization process, Zr-M-PILC-60, -200, 500, and -600 isotherms show a decrease of the adsorbed volume comparing with the original clay. The isotherm shapes except those of Zr-PILC-M-60 and -200 correspond to type IV isotherms characteristic of mesoporous materials (Sing et al, 1985). The hysteresis loop corresponds to type H4 in the IUPAC classification and this is characteristic of material with slit-like pores. These results reflect that the samples initially calcined above 200 °C present mesoporosity as confirmed by the pore size distribution.

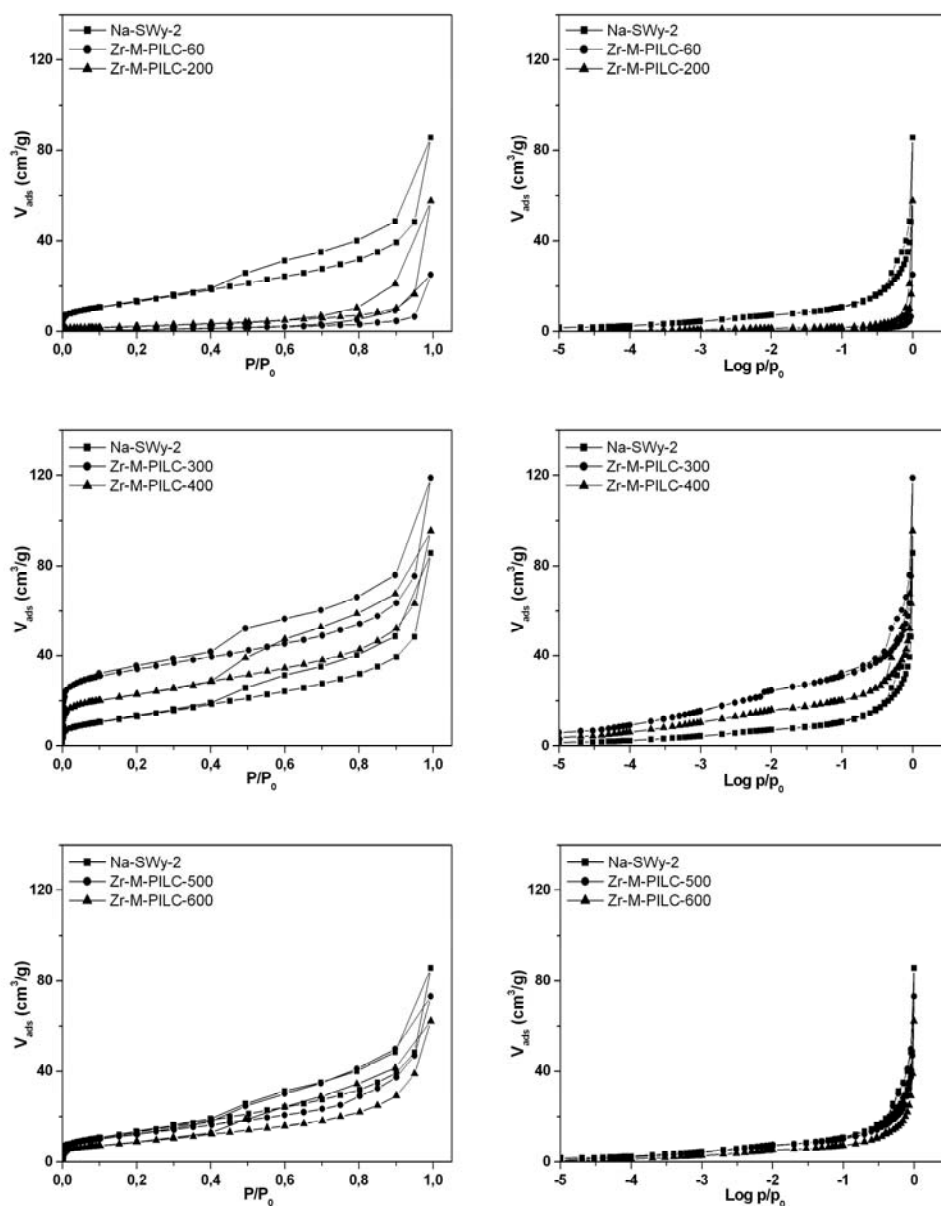


Figure 4.7: N_2 isotherms of Zr-M-PILCs.

4. Magnetic zirconium pillared clays (Zr-M-PILCs)

4.2.3. X-ray fluorescence XRF

Tab. 4.9 collects the chemical composition of Zr-M-PILCs determined by XRF. The additional iron content of Zr-M-PILCs, which is responsible for the magnetic properties, is around 2 % for initially lower calcined samples, and less than or equal to 1 % for the higher calcined ones.

Table 4.9: Fe₂O₃ and ZrO₂ content (%wt.) of Zr-M-PILCs and Zr-PILCs.

	Zr-M- PILC-60	Zr-M- PILC-200	Zr-M- PILC-300	Zr-M- PILC-400	Zr-M- PILC-500	Zr-M- PILC-600
Fe ₂ O ₃ [*]	1.79	2.15	2.09	1.03	0.56	0.45
ZrO ₂ [#]	12.27	12.95	13.58	13.65	13.89	14.17
	Zr- PILC-60	Zr- PILC-200	Zr- PILC-300	Zr- PILC-400	Zr- PILC-500	Zr- PILC-600
ZrO ₂ [#]	13.69	13.74	13.80	13.84	14.03	14.06
ΔZrO ₂	1.42	1.79	0.22	0.19	0.14	-0.11

^{*}: Additional Fe₂O₃ content after magnetization based on the composition of Zr-M-PILCs.

[#]: Additional content based on the composition of Na-SWy-2 given as g of ZrO₂ per 100 g of Na-SWy-2.

ΔZrO₂: Difference in ZrO₂ content (% PILCs- % M-PILCs).

4.2.4. FTIR investigation

FTIR-ATR investigation

In order to investigate whether larger amounts of Fe-oxides are present on the outer surface, ATR method was used. The band observed at 1062 cm^{-1} (Fig 4.8a) is related to the stretching of Si-O groups (Madejova and Komadel, 2001, and Farmer, 1974). A shift of this peak to lower wavenumber (1009 cm^{-1}) with increasing calcination temperature has been observed. This phenomenon can be related to the dehydroxylation effect after calcination. This finding is supported by the decrease of CEC (Tab. 4.4). The appearance of a weak band at 795 cm^{-1} indicates either the presence of traces of poorly crystalline silica (Si-O stretching of quartz and free silica) or Mg-Mg-OH vibrations. Two other weak bands at 776 and 694 cm^{-1} for all Zr-PILCs assigned to the Si-O stretching of quartz, and Si-O group respectively. Furthermore, after the magnetization (Fig. 4.8b), the obtained spectra do not show additional bands; specifically bands indicative of iron bearing phases. These results lead to the conclusion that these phases are not present on the outer surfaces of Zr-M-PILCs.

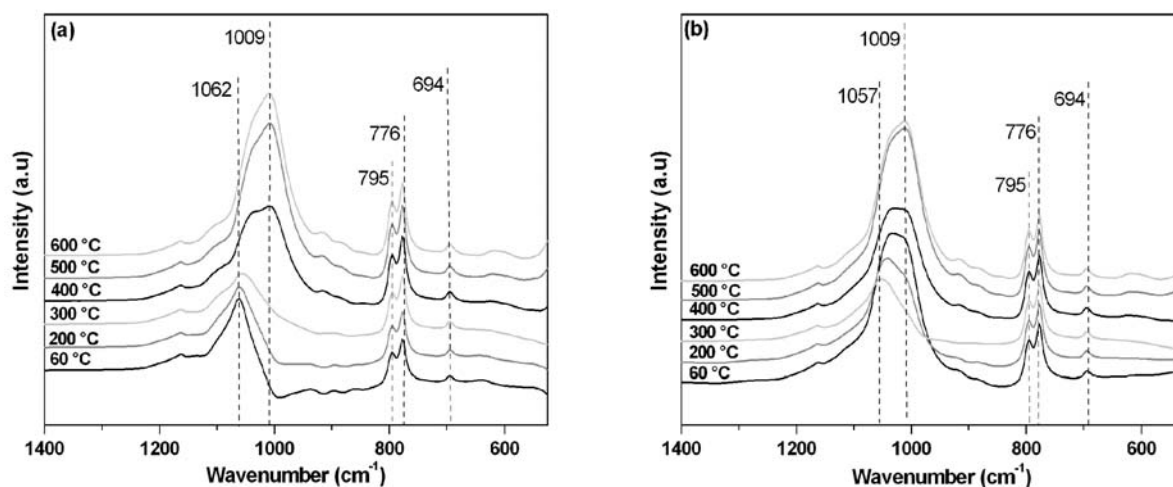


Figure 4.8: FTIR-ATR spectra of: a) Zr-PILCs and b) Zr-M-PILCs.

Far infrared spectroscopy

The spectrum obtained for Zr-M-PILC-300 indicates the presence of magnetite. Further identification of iron phases was not possible for the rest of the Zr-M-PILCs (Fig. 4.9).

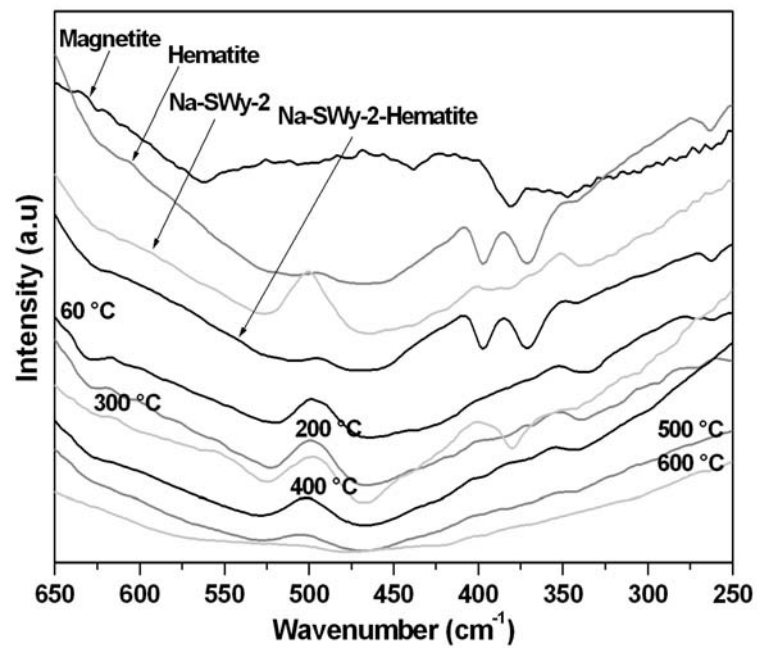


Figure 4.9: FIR spectra of Zr-M-PILCs.

4.2.5. Magnetic properties

Based on the previous results of Zr-M-PILCs, supported by XRD, N₂ adsorption, and XRF analysis, Zr-M-PILC-200, -300, and -500, have been chosen for further magnetic investigation using the SQUID magnetometer.

Hysteresis curves (2, 5, 10, 50, 100, and 300 K)

The hysteresis curves of all samples in the full range (left side, Fig. 4.10) show clearly that saturation magnetization increased with decreasing temperature of SQUID measurements. The samples Zr-M-PILC-200 and Zr-M-PILC-300 reveal a pronounced hysteresis at all temperature suggesting ferro(i)magnetic behaviour (Fig. 4.9b, d). For Zr-M-PILC-500, no hysteresis was obtained at all measured temperatures (Fig. 4.10f).

4. Magnetic zirconium pillared clays (Zr-M-PILCs)

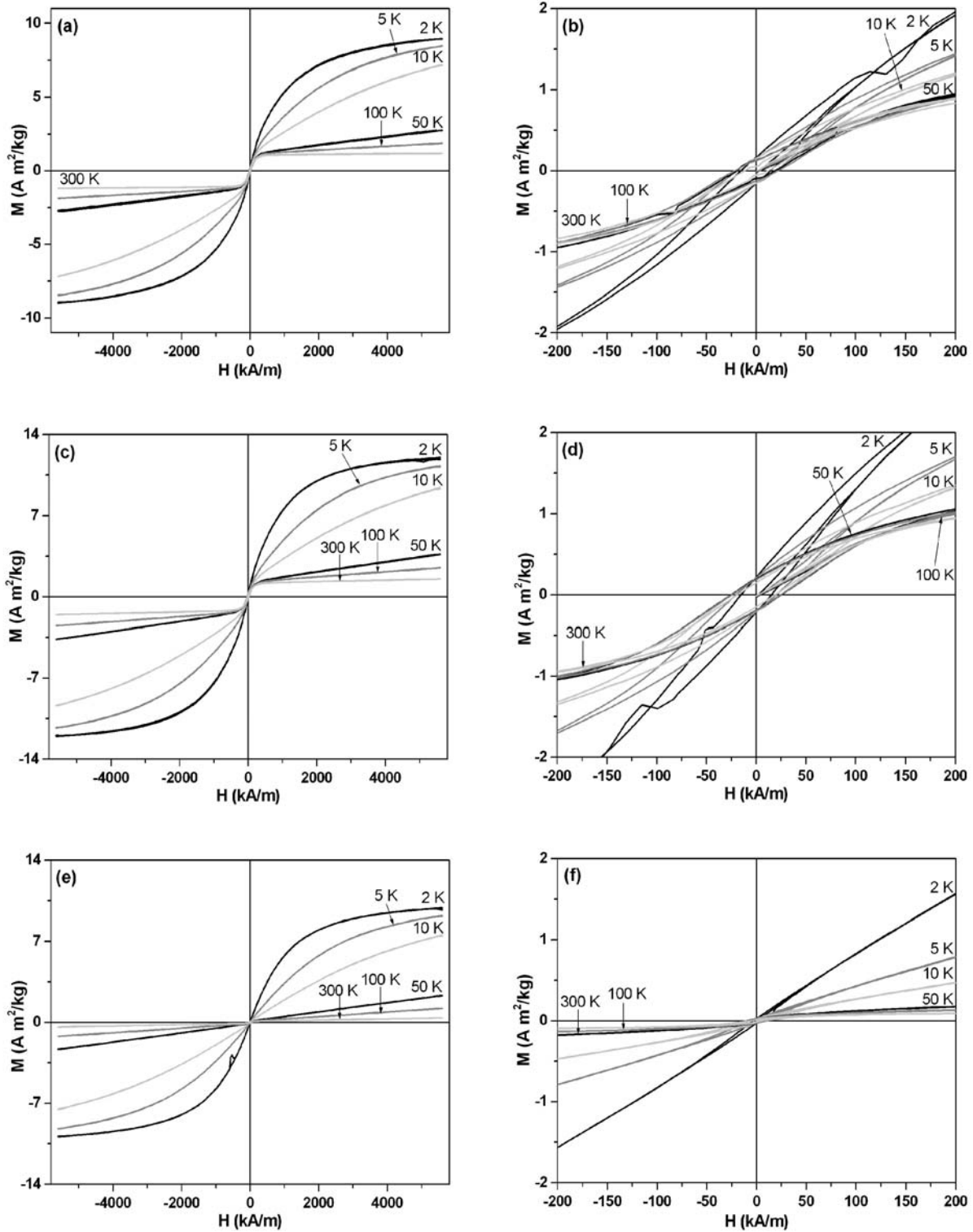


Figure 4.10: Hysteresis loops of Zr-M-PILC-200 (a, b), Zr-M-PILC-300 (c, d), and Zr-M-PILC-500 (e, f). a, c, e: full range; b, d, f: zoom of loops.

4. Magnetic zirconium pillared clays (Zr-M-PILCs)

Temperature dependency of hysteresis parameters

Fig. 4.11 presents the variations of the deduced hysteresis parameters M_s , M_{rs} , H_c , and M_{rs}/M_s of Zr-M-PILCs as a function of the SQUID measurement temperature. On one hand, the values of M_s , M_{rs} , and H_c increase with decreasing temperature. On the other hand, the values of M_{rs}/M_s ratio, however, increase for higher temperature for all the three measured samples.

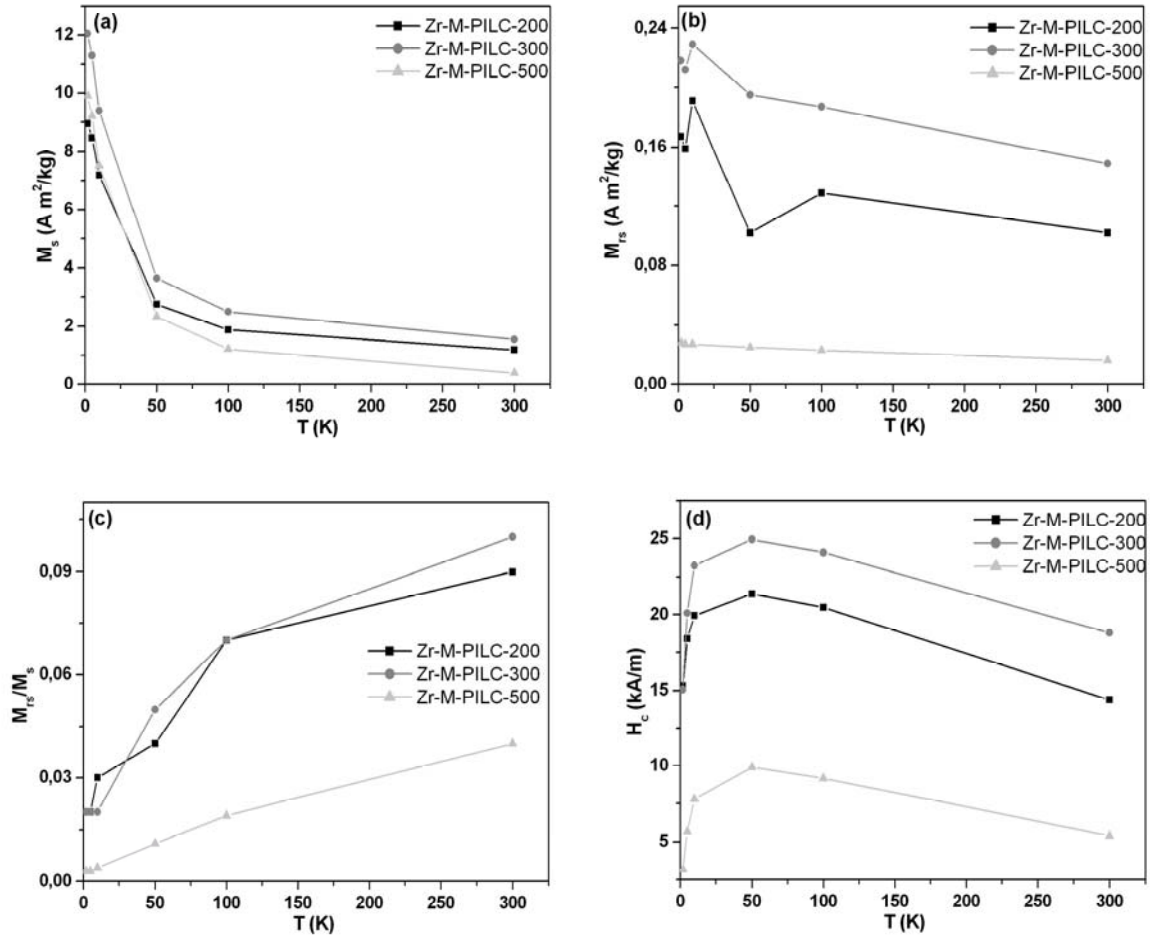


Figure 4.11: Temperature dependency of a) M_s , b) M_{rs} , c) M_{rs}/M_s , and d) H_c of Zr-M-PILCs.

4. Magnetic zirconium pillared clays (Zr-M-PILCs)

Saturation magnetization at room temperature

The values of saturation magnetization M_s at room temperature deduced from the hysteresis curves and normalised to the additional iron content after magnetization are given in Tab. 4.8. In addition, the values of M_s related to the not measured materials (Zr-M-PILC-60, -400, and -600), have been determined by AGM measurement at room temperature. All the presented data were normalized to the additional iron content because this latter is responsible for the magnetic properties. Besides the measured values of M_s , the values of M_s of iron phases are given for comparison (Tab. 4.10). A comparison of the obtained M_s values of Zr-M-PILCs with those of magnetite, maghemite, iron metal and Fe_xB (Moskowitz, 1991, and Zhang *et al.*, 2001) suggests the presence of such phases. The presence of a poorly ordered iron is also considered.

Table 4.10: Specific saturation magnetization of Zr-M-PILCs at 300 K.

Samples	Fe_2O_3 added (Wt %)	M_s (Am^2/kg add iron)
Zr-M-PILC-60	1.79	54*
Zr-M-PILC-200	2.15	66
Zr-M-PILC-300	2.09	72
Zr-M-PILC-400	1.03	47*
Zr-M-PILC-500	0.56	38
Zr-M-PILC-600	0.45	21*
Magnetite Fe_3O_4		90-92
Maghemite $\gamma-Fe_2O_3$		60
Iron Fe		218
Fe_xB		~60

*: Measured by AGM.

Magnetic domain status

Furthermore, the hysteresis parameters determined at 300 K allow also the illustration of the M_{rs}/M_s - H_{cr}/H_c diagram of Zr-M-PILCs (Fig. 4.12).

The obtained diagram was compared with that obtained for magnetite by Muskowitz (1991). From this comparison both Zr-M-PILC-200 and -300 exhibit PSD state, Zr-M-PILC-500 presents MD if magnetite is assumed.

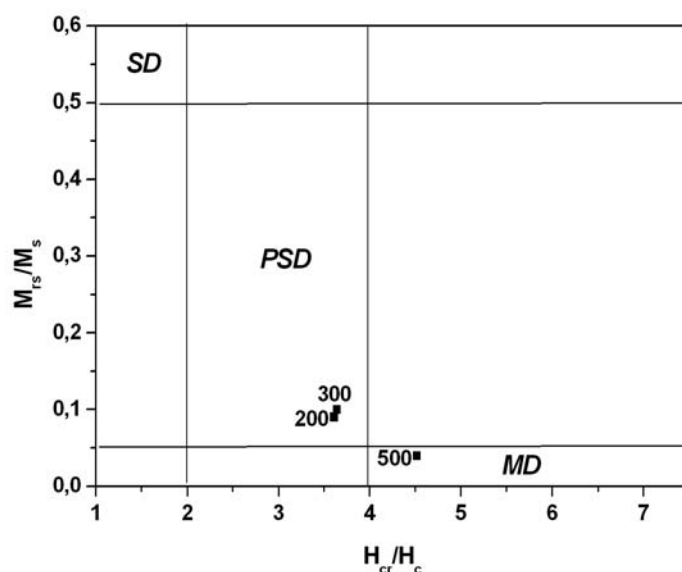


Figure 4.12: M_{rs}/M_s - H_{cr}/H_c diagram of Zr-M-PILCs at 300 K. Domain classification after Moskowitz, (1991).

ZFC/FC investigation

For Zr-M-PILC-200 and Zr-M-PILC-300 the obtained curves show a broad and a shallow distribution of blocking temperatures related to the presence of very weak magnetic ordering (Fig. 4.13). . In contrast, in the case of Zr-M-PILC-500, the plot does not indicate any blocking temperature. This behaviour is supported by the absence of the hysteresis at all the measured SQUID temperatures for this sample and is indicative for paramagnetic behaviour.

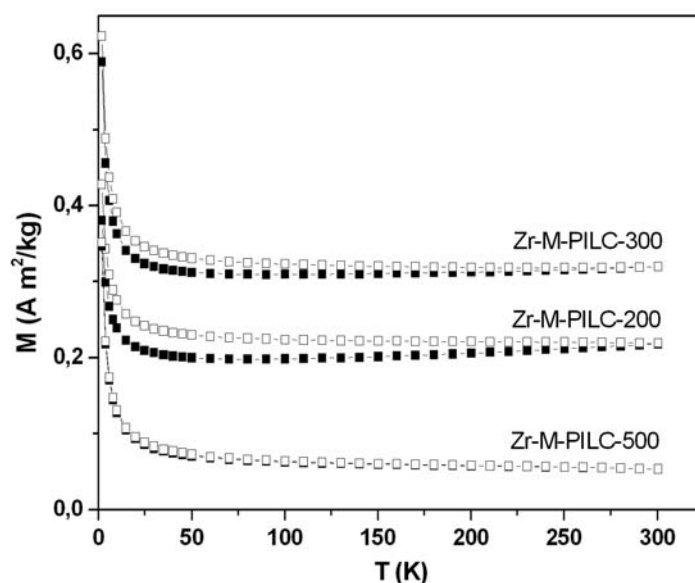


Figure 4.13: ZFC/FC curves of Zr-M-PILC. Full symbols ZFC, open symbols FC curves.

Curie-Weiss law: Determination of θ and C

The values of Weiss constant, θ , and Curie constant, C, are collected in Tab. 4.9. The negative sign of θ (Tab. 4.11) indicates that all the measured Zr-M-PILCs behave as ferrimagnetic materials. Moreover, the determined Curie constant C was higher for samples calcined at higher temperatures.

Table 4.11: Parameters of the Curie-Weiss-law of Zr-M-PILCs

Samples	θ (K)	$C \cdot 10^{-4}$ (m ³ K/kg)	R^2
Zr-M-PILC-60	n.d	n.d	n.d
Zr-M-PILC-200	-1.0	16.0	1.000
Zr-M-PILC-300	-0.6	20.3	1.000
Zr-M-PILC-400	n.d	n.d	n.d
Zr-M-PILC-500	-0.7	20.3	0.999
Zr-M-PILC-600	n.d	n.d	n.d

θ : Weiss constant and C: Curie constant
n.d: not determined.

4.2.6. Mössbauer spectroscopy

The room temperature Mössbauer spectra of Zr-M-PILCs are presented in Fig. 4.14. For the samples initially heated at 300, 400, 500 and 600 °C, a minor ferrous doublet was observed in addition to the ferric doublet, of the parent clay SWy-2 (Fig. 2.14). This indicates that the borohydride reduction only is partially effective in reducing the ferric ions. In contrast a major ferrous doublet was observed in the case of Zr-M-PILC-60 and -200.

The spectra of all samples except those of Zr-M-PILC-500 and -600 exhibit in addition to the features seen at room temperature (ferric and ferrous doublets) a broad background component and thus a minor indication of a sextet due to FeB/Zr-alloys of different compositions (Van Wonergerhm *et al.*, 1986) (Fig. 4.14).

As shown in Tab. 4.12, the deduced Fe^{2+}/Fe^{3+} ratio at room temperature, decreased for samples calcined at higher temperatures.

Furthermore, only the samples Zr-M-PILC-300 and -500 have been measured at low temperature (Fig. 4.15). The Mössbauer spectra are characterized by a distribution on

4. Magnetic zirconium pillared clays (Zr-M-PILCs)

relaxation times. Due to this distribution, part of the sample relaxes fast in the Mössbauer time scale giving rise to two doublets and part of the sample relaxes slowly giving rise to a sextet characteristic of magnetic ordering. The sextet of Zr-M-PILC-300 is more pronounced than that of Zr-M-PILC-500.

Finally, none of the investigated spectra show any evidence for metallic iron as has been found in Ti-M-PILCs and Al-M-PILCS.

Table 4.12: $\text{Fe}^{2+}/\text{Fe}^{3+}$ ratios, isomer shift (IS) and quadrupol splitting (QS) determined by Mössbauer spectroscopy of Zr-M-PILCs.

Samples	$\text{Fe}^{2+}/\text{Fe}^{3+}$	Fe^{2+}	Fe^{2+}	Fe^{3+}	Fe^{3+}
	ratio	IS (mm/s)	QS (mm/s)	IS (mm/s)	QS (mm/s)
Zr-M-PILC-60	0.57	1.14	2.83	0.33	0.84
Zr-M-PILC-200	0.58	1.17	2.88	0.33	0.81
Zr-M-PILC-300	0.11	1.36	2.48	0.30	0.83
Zr-M-PILC-400	0.09	1.31	2.40	0.32	0.83
Zr-M-PILC-500	0.16	1.18	2.52	0.34	0.94
Zr-M-PILC-600	0.07	1.12	2.68	0.38	1.17

4. Magnetic zirconium pillared clays (Zr-M-PILCs)

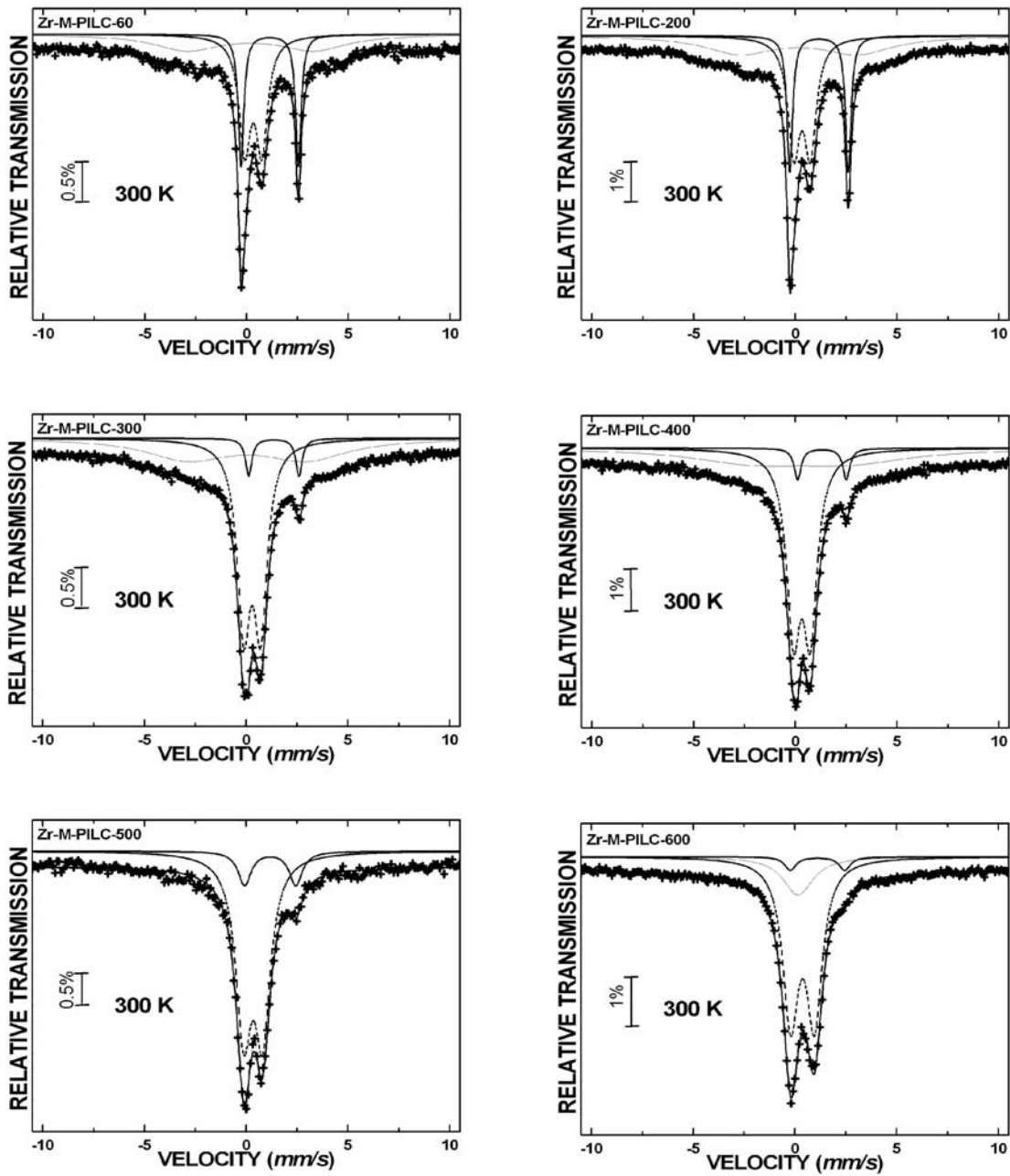


Figure 4.14: Mössbauer spectra of Zr-M-PILCs at room temperature.

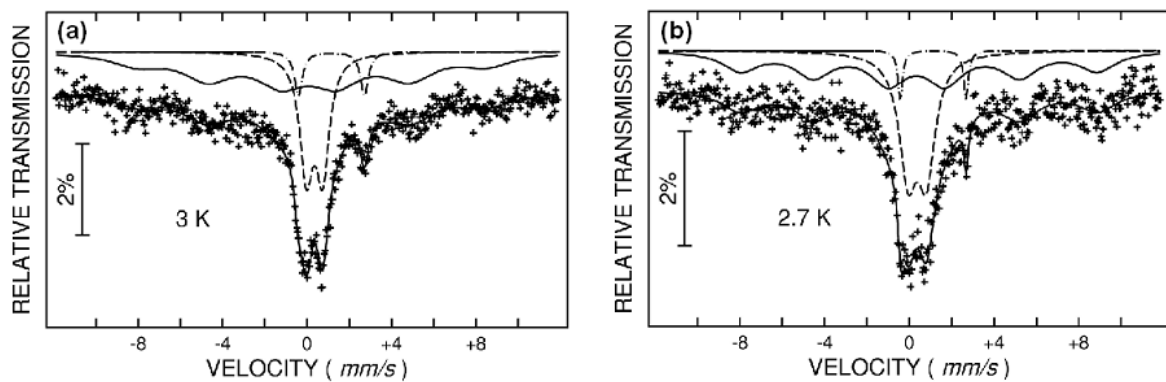


Figure 4.15: Mössbauer spectra of a) Zr-M-PILC-300 at 3 K and b) Zr-M-PILC-500 at 2.7 K.

4.3. Discussion

The Zr-PILC structure was affected during the reduction process. This can be explained by the reduction of Fe^{3+} in octahedral positions upon treatment with sodium borohydride as reported by Rozenson and Heller-Kallai (1976). This reduction led to the partial deterioration of the Zr-PILC-structure, after the introduction of the additional iron. This deterioration was more pronounced for the samples calcined at 60 and 200 °C hence lower stability, as indicated by the higher loss in SSA and porosity (Tab. 4.8).

Calcination temperature influences the SSA, the porosity and the stability, but Zr-PILCs react differently on the magnetization process, which consists of the adsorption of Fe and reduction by NaBH_4 .

The additional iron content of Zr-M-PILCs is around 2 % for lower calcined samples, and about 1 % for higher calcined samples. The M_s values normalized to the additional amount of iron except that of Zr-M-PILC-600 indicate the presence of magnetite/maghemite phases, and FeB-alloy (Tab. 4.10). The sample Zr-M-PILC-300, which has the highest M_s value contains a band indicative of magnetite in its FIR spectrum.

Mössbauer data prove the presence of divalent and trivalent iron, but the calculated ratios are lower than 0.5 for samples Zr-M-PILC-300, -400, -500, and -600, and higher than 0.5 for -60, and -200 the characteristic value for stoichiometric magnetite. The presence of ferrimagnetic phases is supported by the negative sign of the Weiss constant θ .

The sample Zr-M-PILC-500 which has M_s value lower than those of -200 and -300 ZFC/FC show a dominating paramagnetic behaviour.

From Mössbauer results, the samples Zr-M-PILC-300 and -500 exhibit a beginning of magnetic ordering in their Mössbauer spectra at 2.7 K.

The low calcined samples except Zr-M-PILC-300, which have a high CEC value, present high iron content (~ 2 %). In addition the sample Zr-M-PILC-300 contains magnetite in its interlayer space as indicated by FIR spectroscopy.

The high reduction in SSA and V_p for Zr-M-PILC-60 and Zr-M-PILC-200 after magnetization (Tab. 4.8) correlates well with the corresponding difference in zirconium content ΔZrO_2 (Tab. 4.9). This correlation is reflected in the filling factor FF computation (Tab. 4.13). The corresponding FF of these samples is decreasing after magnetization from 0.4 to 0.1 and 0.5 to 0.2 for Zr-M-PILC-60 and Zr-M-PILC-200, respectively. In contrast, the sample Zr-M-PILC-300 which has the highest M_s value, shows the smallest loss in SSA and porosity, thus exhibiting the highest stability.

4. Magnetic zirconium pillared clays (Zr-M-PILCs)

Table. 4.13: FF and IF of Zr-PILCs and Zr-M-PILCs.

Samples	V_p (cm^3/g)	V_{ILthe} (cm^3/g)	V_{ILexp} (cm^3/g)	FF	IF
Zr-PILC-60	0.097	0.324	0.121	0.4	3
Zr-PILC-200	0.093	0.250	0.117	0.5	2
Zr-PILC-300	0.091	0.242	0.115	0.5	2
Zr-PILC-400	0.082	0.224	0.106	0.5	2
Zr-PILC-500	0.063	0.201	0.087	0.4	2
Zr-PILC-600	0.046	0.067	0.070	1.0	1
Zr-M-PILC-60	0.003	0.190	0.024	0.1	8
Zr-M-PILC-200	0.008	0.172	0.031	0.2	6
Zr-M-PILC-300	0.070	0.183	0.094	0.5	2
Zr-M-PILC-400	0.054	0.164	0.078	0.5	2
Zr-M-PILC-500	0.033	0.090	0.057	0.6	2
Zr-M-PILC-600	0.025	0.056	0.050	0.9	1

5. Adsorption

5.1. Introduction

In contrast to the previous chapters which reported the synthesis and characterisation based on pillared clays using three different pillaring agents mainly titanium, aluminium, and zirconium, the present chapter investigates the behaviour of these materials via copper adsorption. In addition, only a few investigations have been focused on the heavy metal adsorption using pillared clays as sorbents (Bouchenafa-Saib *et al.*, 2007, Manohar *et al.*, 2006). Here, the efficiency of the three different pillared clays for the copper adsorption was also compared with that of the three corresponding magnetic forms.

In order to know and suggest the mechanism of the copper sorption on pillared clays and their magnetic forms, adsorption isotherm modelling and kinetic studies were applied.

5.2. Theoretical foundation

5.2.1. Adsorption isotherm

The adsorption equilibrium is usually described by an isotherm equation (Ho and McKay, 1999), whose parameters express the surface properties and affinity of the adsorbent, at a fixed temperature and pH.

Langmuir and Freundlich adsorption isotherms are also classical models for describing equilibrium between metal ions adsorbed onto the sorbent and metal ions remaining in solution at equilibrium at a constant temperature. Both isotherm models can be easily transformed into linear forms to obtain adjustable parameters by linear regression analysis (Doyurum and Celik, 2006).

The theoretical Langmuir isotherm relies on the chemical or physical interaction (or both) postulated to occur between the solute and the available vacant sites on the sorbent surface, which may be described as follows (Langmuir, 1916):

$$C_e/q_e = 1/bq_m + (1/q_m)C_e \quad (1)$$

where q_e is the amount of the sorbate at equilibrium (mg/g), q_m is the maximum metal uptake capacity or monolayer capacity (mg/g sorbent), C_e is the equilibrium concentration (mg/l metal solution), and b (l/mg) is a coefficient related to the affinity between the metal ion and the sorbent.

The Freundlich isotherm is an empirical equation that is based on the sorption of a sorbate on a heterogeneous surface of a sorbent as given by the equation (Freundlich, 1906):

$$q_e = K_f(C_e)^{1/n} \quad (2)$$

where K_f and n are the Freundlich empirical constants indicative of sorption capacity and sorption intensity, respectively.

5.2.2. Adsorption kinetics

The adsorption kinetics was tested with respect to the following well known models: Pseudo-first-order kinetics using the Lagergren equation (Lagergren, 1898):

$$\ln(q_e - q_t) = \ln q_e - k_1 t \quad (3)$$

Where q_e and q_t are the values of amount adsorbed per unit mass at equilibrium and at any time t , and k_1 is the pseudo-first-order adsorption rate constant. A straight line of $\ln(q_e - q_t)$ versus t indicates applicability of the pseudo-first order kinetics model. In a true pseudo-first order process, $\ln q_e$ should be equal to the intercept of plot of $\ln(q_e - q_t)$ against t .

The pseudo-second order equation (Ho and McKay, 1998), based on the sorption equilibrium capacity, may be expressed as:

$$t/q_t = 1/k_2 q_e^2 + (1/q_e)t \quad (4)$$

The plot of t/q_t versus t gives a linear relationship, which allows computation of q_e and k_2 .

During the adsorption, the metal ions are transferred from aqueous phase to the surface of solid and subsequently they may diffuse into the interior of the particles if these are porous, as is the case for pillared clays. The intra-particle diffusion is governed by the following equation (Weber *et al.*, 1963):

$$q_t = K_i t^{1/2} \quad (5)$$

The plots of q_t versus $t^{1/2}$ yield straight lines passing through the origin and the slope gives the diffusion rate constant K_i .

5.3. Materials and adsorption experiment

5.3.1. Materials

Only six samples Ti-PILC-500, Al-PILC-400, and Zr-PILC-300 and their three magnetic forms (Ti-M-PILC-500, Al-M-PILC-400, and Zr-M-PILC-300) were used in copper adsorption experiment. This choice was based on the textural properties as well as the specific saturation magnetization M_s . Although, most of the data related to these samples were already given in previous chapters, in Tab. 5.1 we report again the SSA, M_s , d_{001} , etc.

Table 5.1: Textural and magnetic properties of the chosen materials.

Samples	d_{001} (nm)	SSA (m^2/g)	V_{mp} (cm^3/g)	V_{mes} (cm^3/g)	V_p (cm^3/g)	CEC (meq/100 g)	M_s ($A m^2/kg$)
Ti-PILC-500	2.50	244	0.005	0.154	0.158	13	-
Al-PILC-400	1.73	183	0.048	0.055	0.103	24	-
Zr-PILC-300	1.61	166	0.046	0.045	0.091	48	-
Ti-M-PILC-500	1.37	175	0.004	0.110	0.114	44	62
Al-M-PILC-400	1.42	37	0.003	0.027	0.030	88	43
Zr-M-PILC-300	1.45	123	0.029	0.041	0.070	83	77

d_{001} : Basal spacing.

SSA: Specific surface area.

V_p : Pore volume at $P/P_0 = 0.7$ (pore width ≤ 7 nm).

V_{mp} : micropore volume.

V_{mes} : mesopore volume.

CEC: cation exchange capacity.

M_s : saturation magnetisation.

5.3.2. Adsorption experiment

A stock solution containing 1000 mg of copper metal ion per liter was prepared by dissolving the appropriate amount of $Cu(NO_3)_2 \cdot 3H_2O$ in deionized water and was used to prepare the adsorbate solutions of the required concentrations.

Adsorption experiments were carried out in 250 ml Erlenmeyer flasks by mixing together a constant amount of adsorbent with a constant volume of the aqueous copper solution. The contents in the flasks were agitated by placing them on a shaking table at room temperature (22-25 °C). The pH of the experiments was fixed to 5 in order to avoid the formation of

copper precipitates at higher pH as determined by the MINEQL calculation for each concentration (Schecher and McAvoy, 2003). The pH of the adsorptive solution was adjusted by addition of 0.01 N NaOH or 0.01 N HCl in drops as needed. After stirring, the mixture was centrifuged at 4500 rpm for 10 min and the concentration of copper remaining unabsorbed in the supernatant liquid was determined by atomic absorption spectroscopy AAS. The following conditions were maintained for different sets of experiments:

Adsorption isotherm

Clay suspension 1g/l, Cu²⁺ concentration: 10, 20, 30, 50, 80, and 100 mg/l, reaction temperature 22-25 °C, pH 5, interaction time 1440 min.

Adsorption Kinetics

Clay suspension 1g/l, Cu²⁺ concentration 50 mg/l, reaction temperature 22-25 °C, pH 5, interaction time: 5, 15, 30, 60, 120, 240, 360, 480, 1440 min.

5.3.3. Methods

In addition to the methods described previously in Chapter 1 (Section 1.4) such as XRD, N₂ adsorption, CEC determination, etc. atomic adsorption spectrometry AAS was used in order to determine the copper concentration in mg/l. The AAS analyses were performed on a Varian SpectrAA 220 FS with air-acetylene oxidizing flame (For Cu²⁺, the measurement conditions are: lamp current 4 mA and 222.6 nm wavelength). Before measurement eight standards have been used in calibration step in the required concentration range. For each sample, the copper concentration was measured three times and the mean value was automatically read out.

5.4. Results and discussion

5.4.1. Adsorption isotherm

To examine the relationship between the copper adsorption capacity q_e and the concentration of copper at equilibrium C_e , the sorption data of different materials were fitted to Langmuir and Freundlich isotherms models. These two models are widely used for adsorption data analysis, since they have the ability to describe experimental results for a wide range of initial metal concentrations. The Langmuir and Freundlich constants and their correlation coefficients (R^2) evaluated from these isotherms for Cu²⁺ are given in Tab. 5.2. The corresponding linear fits are illustrated in Fig. 5.1 and Fig. 5.2. The adsorption characteristics of Cu²⁺ on the three chosen pillared clays followed more closely the Langmuir isotherm model than the Freundlich isotherm model. This observation is

further supported by the evaluation of the respective correlation coefficients, which is a measure of how well the predicted values from a forecast model match the experimental data. The R^2 values for Ti-PILC-500, Al-PILC-400, and Zr-PILC-300 were 0.91, 0.93, and 0.92 and 0.54, 0.69, and 0.87, for Langmuir and Freundlich models, respectively. However, for M-PILCs, both Langmuir and Freundlich plots had good linearity ($R^2= 0.92-0.99$).

In general terms, the copper sorption on pillared clays can involve cation exchange processes on the surface and interlayer clays sites, or complexation reactions with the corresponding pillar oxides, or pore diffusion process. Although, M-PILCs have lower d_{001} , SSA and V_p than PILCs, the maximum copper uptake capacity q_m of magnetic pillared clays was significantly higher than that of the corresponding initial pillared clays as noted from Tab. 5.2. The same trends were obtained for the Freundlich parameter K_f which presents the sorption capacity. Since the magnetic materials have higher CEC than the pillared clay, the adsorption is more dependent upon cation exchange. The nature of the oxide pillar has to be also considered, indeed, Ti-M-PILC-500 and Al-M-PILC-400 have higher q_m than Zr-M-PILC-300. Thus, the complexation reactions with aluminium and titanium pillars are more important than with zirconium pillars. As regards the pillared clays except Zr-PILC-300, the copper species are probably mainly bound to pillar oxides since their CEC was deduced after the pillaring process. For all samples, pore diffusion will be examined thereafter in the kinetic part. After magnetization, the number of adsorption sites increases as proved by the increase of the Langmuir monolayer capacity q_m , thus the parameter b which is related to the strength of the existing sites and the affinity between the copper and the sorbent was also influenced. Indeed, the magnetic pillared sorbents have higher b values than those of pillared sorbents.

Table 5.2: Langmuir and Freundlich isotherms parameters of pillared and magnetic pillared clays.

Clay adsorbent	Langmuir parameters			Freundlich parameters		
	q_m (mg/g)	b (l/mg)	R^2	K_f (mg/g)	$1/n$ (l/g)	R^2
Ti-PILC-500	11.1	0.09	0.91	3.7	0.22	0.54
Al-PILC-400	10.8	0.03	0.93	1.4	0.37	0.69
Zr-PILC-300	15.1	0.07	0.92	3.5	0.29	0.87
Ti-M-PILC-500	35.6	4.21	0.99	11.6	0.26	0.99
Al-M-PILC-400	37.7	1.94	0.96	10.6	0.26	0.94
Zr-M-PILC-300	30.8	1.75	0.94	6.4	0.35	0.92

Furthermore, the parameter $1/n$ which is indicator of adsorption intensity (Freundlich, 1906) is less than 1 for all samples suggesting that the adsorption sites are heterogeneous (Bouras, 2003, Boubarka *et al.*, 2008). This fact was also attributed to a chemical adsorption (Bouras, 2003).

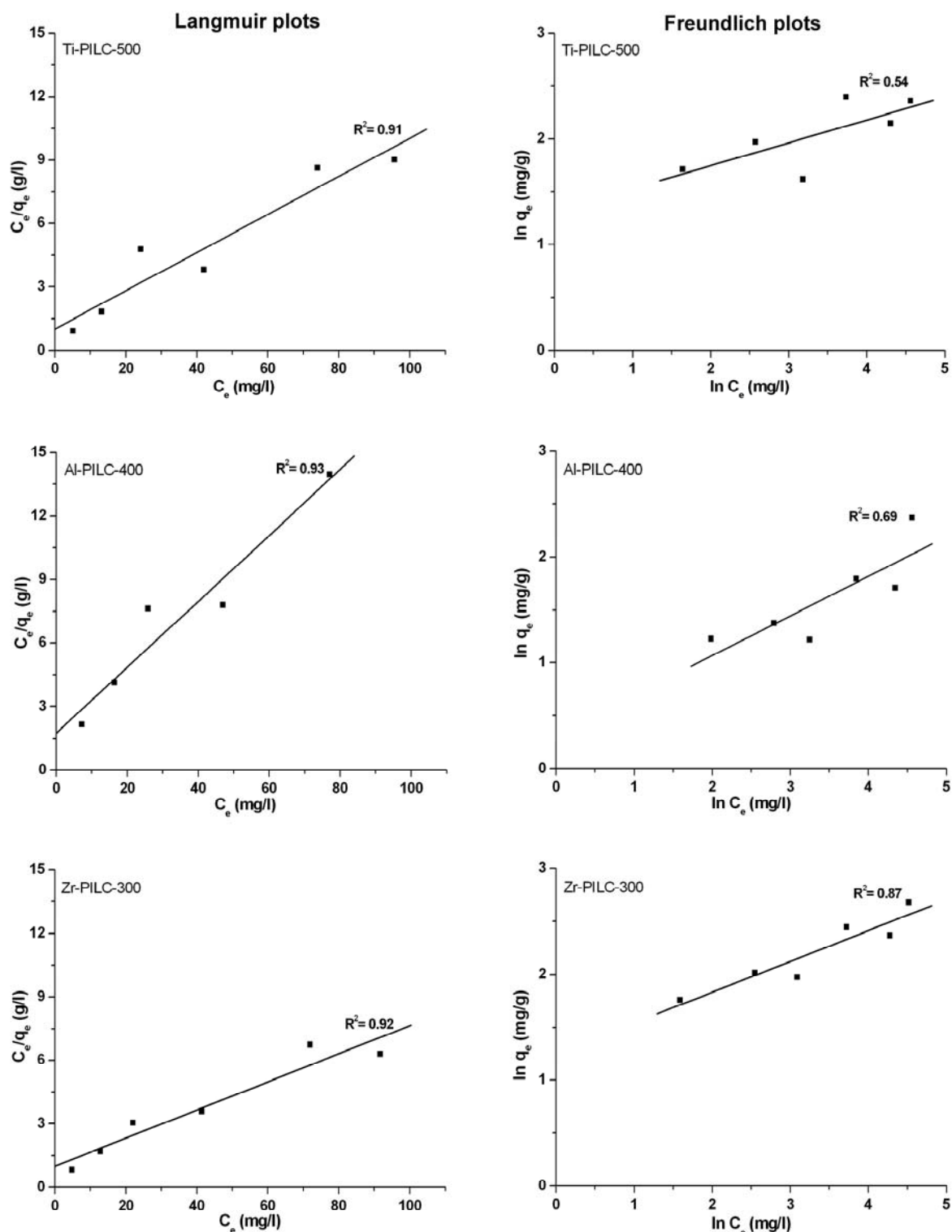


Figure 5.1: Langmuir and Freundlich plots for copper adsorbed on pillared clays: Ti-PILC-500, Al-PILC-400, and Zr-PILC-300.

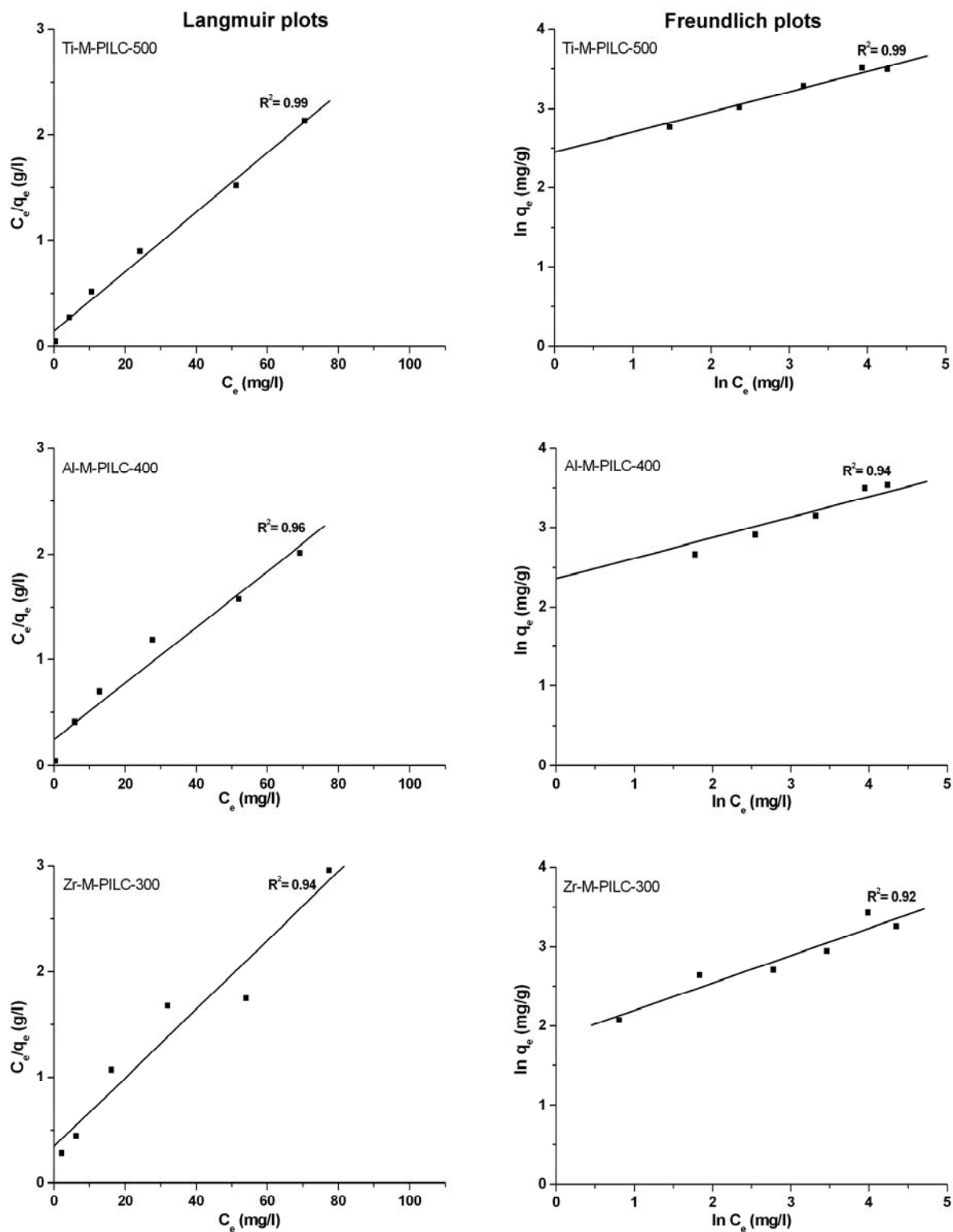


Figure 5.2: Langmuir and Freundlich plots for copper adsorbed on magnetic pillared clays: Ti-M-PILC-500, Al-M-PILC-400, and Zr-M-PILC-300.

5.4.2. Adsorption kinetics

The controlling mechanism of Cu uptake on pillared and magnetic pillared samples was investigated by fitting the experimental sorption data to pseudo-first order and pseudo-second order kinetics models. The results of the kinetics parameters calculated from the linear plots of pseudo-first order and pseudo-second order kinetics models are presented in Tab. 5.3. The computed q_e was also compared with the experimental q_{eExp} .

The low correlation coefficients obtained for the first-order model indicate that the sorption of copper on PILCs as well as on M-PILCs did not follow the first-order reaction.

This is also observed when q_{e1} obtained from this plot is compared with the experimental q_{eExp} (Tab. 5.2). The first-order kinetics is therefore inappropriate to control the rate of copper adsorption.

The experimental data were observed to fit well to the second-order equation (Fig. 5.3). The correlation coefficients R^2 for the linear plots of t/q_t against t were observed to be close to 1 for both sets of samples. The computed q_{e2} values for all sorbents were also very close to the experimental q_{eExp} values. These observations suggest that the process controlling the rate may be a chemical sorption involving valence forces sharing or exchanging of electrons between sorbent and sorbate (Ho and McKay, 1998), this result is in agreement with the $1/n$ values obtained from Freundlich plots.

The constant rate values k_2 of magnetic materials are higher than those of pillared sorbents, this can be explained by the easiness of the copper sorption on the M-PILCs rather than on PILCs, although pillared clays have high specific surface areas and pore volumes.

In order to check the pore diffusion of copper into the pillaring structure, the intra-particle diffusion was applied to all the chosen materials. The plots of q_t versus $t_{1/2}$ (not shown) yield no zero intercept indicating that the diffusion of copper species into the pores is not the dominating factor controlling the mechanism of the process (Weber *et al.*, 1963).

Table 5.3: First and second-order kinetics parameters for the adsorption of Cu^{2+} and experimental $q_{e\text{Exp}}$ on pillared clays and their magnetic forms.

Clay adsorbent	First-order			Second-order			$q_{e\text{Exp}}$ (mg/g)
	q_{e1} (mg/g)	k_1 (min^{-1})	R^2	q_{e2} (mg/g)	k_2 (g/mg min)	R^2	
Ti-PILC-500	4.4	0.002	0.90	11.3	0.003	1.00	11.5
Al-PILC-400	2.8	0.004	0.69	8.1	0.002	0.99	6.7
Zr-PILC-300	3.7	0.004	0.61	12.6	0.003	1.00	12.1
Ti-M-PILC-500	2.0	0.015	0.21	24.2	0.005	1.00	22.6
Al-M-PILC-400	0.9	0.001	0.02	20.7	0.005	1.00	22.1
Zr-M-PILC-300	0.9	0.001	0.05	19.7	0.014	1.00	22.2

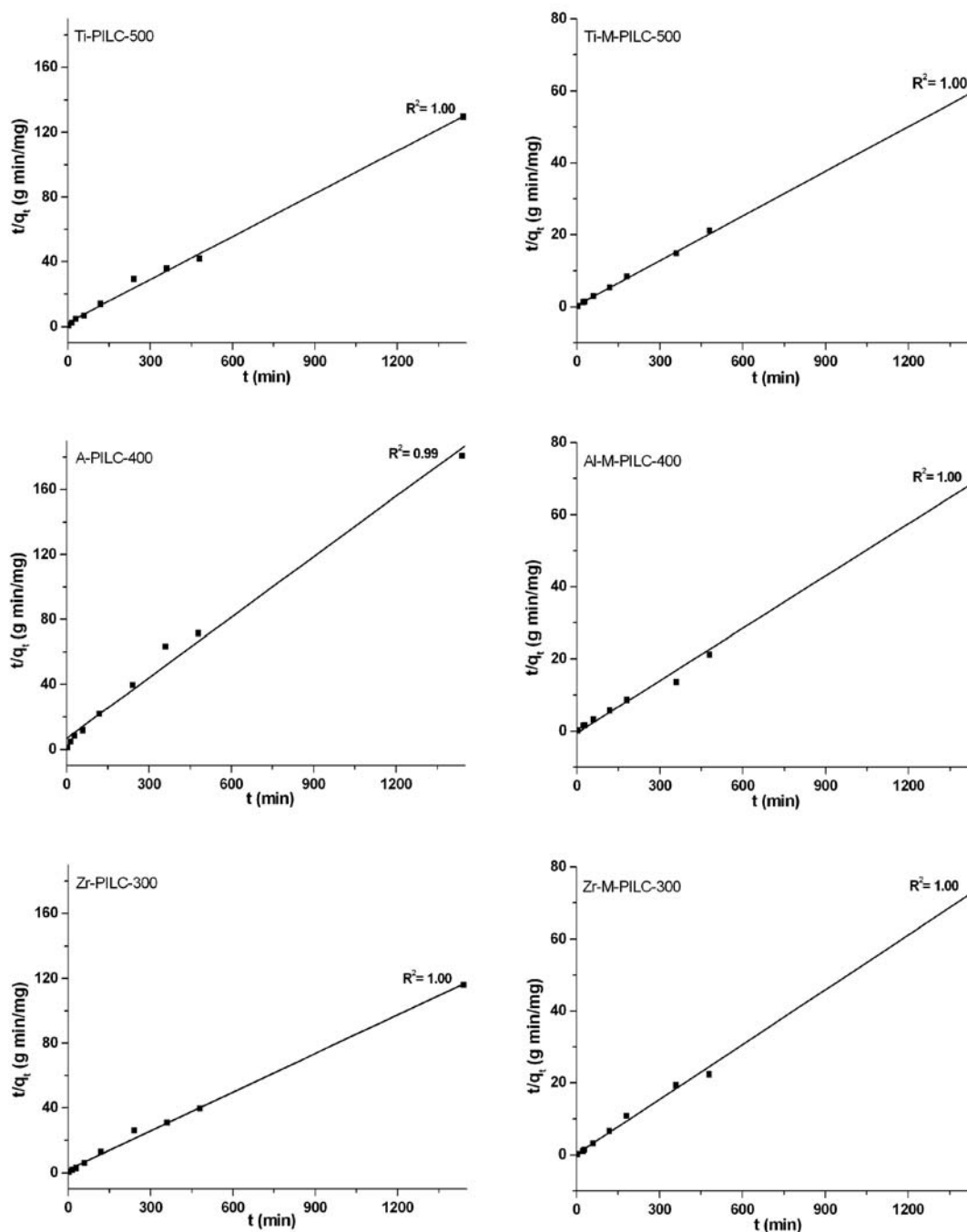


Figure 5.3: Second-order plot for copper adsorbed on pillared clays: a) Ti-PILC-500, b) Al-PILC-400, and c) Zr-PILC-300.

6. Discussion

In the present work the study of magnetic properties upon Fe-intercalation and subsequent reduction by NaHB_4 of pillared clays obtained at different calcination temperatures was investigated. The influence of the nature of the pillars and its thermal stability on the porosity was presented.

It was found that the obtained pillared clays react differently to the magnetization process as a function of the nature of the intercalated pillar and its calcination temperature. For all pillared clays, the increase in the calcination temperature led to the decrease of the CEC. Moreover, this feature is different as a function of the pillar species. At low temperature (60, 200, and 300 °C) the CEC compared with that of the starting clay was reduced to 70 %, 50 %, and 40 % for Ti-PILCs, Al-PILCs, and Zr-PILCs, respectively. After heat treatment above 400 °C an average reduction of 83 % in CEC was obtained for all PILC samples. Thus the PILCs present a difference in CEC at lower temperatures, the corresponding CEC values follow the order: Zr-PILCs > Al-PILCs > Ti-PILCs. This behaviour can be explained by the differences in the quantities of H^+ ions liberated after the formation of pillars as described by Cool and Vansant, (1998). Since the different intercalated species do not have the same structure, the amount of the H^+ ions liberated after heating is therefore not the same. In this case, a high value of H^+ corresponds to low CEC values.

This explanation is supported in STA results by the differences in the temperature of the release of the structural hydroxyl groups, coming from clay and pillars, between the pillared clays showing that each pillar elements behave differently upon heating. Thermal treatment up to 600 °C showed that the dehydroxylation temperatures occurred in the following order: Al-PILCs > Zr-PILCs > Ti-PILCs.

After magnetization, SSA and porosity decreased. This loss was different for each pillared clay and for each calcination temperature. Temperatures of 300 °C, 400 °C, and 500 °C for Zr-M-PILCs, Ti-M-PILCs, and Al-M-PILCs, respectively were the best calcination temperatures maintaining the highest SSA and V_p with high saturation magnetization M_s . A comparison of the Weiss constant of the most stable magnetic pillared clays (Ti-M-PILC-400, Al-M-PILC-500, and Zr-M-PILC-300) shows that the ferrimagnetic behaviour is more pronounced for Ti-M-PILC-400 and Al-M-PILC-500 than that of Zr-M-PILC-300.

Furthermore an examination of the chemical composition through the differences between pillar element content after pillaring and magnetization show the best correlation with SSA and porosity reduction in the case of aluminium materials. $\Delta\text{Al}_2\text{O}_3$ decreases at

higher temperature to attend 1.21 % for Al-M-PILC-500 confirming again the stability of aluminium pillar oxide at 500 °C. In the case of Zr materials, ΔZrO_2 decreases with increasing calcination temperature. A value of 0.22 % has been found in the case of Zr-M-PILC-300. For this sample, the low value of the ΔZrO_2 is in agreement with the small reduction in SSA (26 %). Thus at 300 °C the zirconium pillars are stable against magnetization.

In regard to Ti materials the negative values for ΔTiO_2 can not be explained. The apparent gain in TiO_2 must be attributed to errors in the determination of Ti in the XRF measurements. There is no reaction feasible in the magnetization process which would lead to an increase of Ti content.

A comparison of the copper adsorption features of some pillared clays and their magnetic forms as function of pillar species was presented. The obtained results show that the copper adsorption mechanism is more involved by cation exchange process. The complexation between pillars and copper species is also considered. In addition, although pillared clays have high specific surface areas, pore volumes, and basal spacing, the copper sorption is easily effectuated on the M-PILCs rather than on the PILCs.

7. Appendix

7.1. Theoretical part

Clays are important materials with a large variety of applications in ceramics, oil drilling, and the metal and paper industry. Clays are furthermore used as adsorbents, decoloration agents, ion exchangers, and molecular sieve catalysts (Kloprogge, 1998).

For the application as molecular sieve catalyst a group of expandable clays known as smectites is employed which are phyllosilicates or layer silicates having a layer structure. Montmorillonite which belongs to the smectite clay mineral group is the most popular type of clay applied in pillaring processes. The basic structural unit of this group of clays consists of two tetrahedral Si sheets separated by one octahedral Al or Mg sheet. Substitutions of Al^{3+} by Mg^{2+} in the case of montmorillonite result in negative charges on clay layers, which are compensated by hydrated cations in the interlayer space. Montmorillonite is one of the swelling clays; water is able to enter into the interlayer region, thereby expanding the clay layers, and the interlayer cations can be exchanged with other larger hydrolysed metal cations or organic/inorganic complexes. These two properties of smectites, swelling and ion-exchangeability are critical for the successful synthesis of PILCs.

7.1.1. Pillared clays

Pillared clays constitute one of the most widely studied families among the groups of microporous materials developed by molecular engineering. These solids are obtained by exchanging the interlayered cations of layered clays with bulky inorganic polyoxocations, followed by calcination. The intercalated polycations increase the basal spacing of the clays and, upon heating, they are converted to metal oxide clusters by dehydration and dehydroxylation. These metal oxide clusters, named pillars, are inserted between the clay layers, yielding temperature stable oxide pillars that permanently keep the layers apart, preventing its collapse. After pillaring, the presence of this new porous structure and the incorporation of new active sites present several possible applications of these materials.

Preparation

In general terms, the experimental procedure for the synthesis of a PILC can be described as follows (Fig. 7.1). A suspension containing layered clay such as montmorillonite is mixed with a solution containing a polyoxocation. The reaction between the polycation and the clay, consisting of the substitution of the exchangeable cations in the interlayer space of the clay by the inorganic polyoxocations, is usually known as cationic exchange reaction or

intercalation. After the reaction, the resulting suspension is separated and washed, giving rise to the intercalated clay. Its calcination at high temperature stabilizes the polymeric cation, thus preventing the collapse of the interlayer space and generating a stable porous structure.

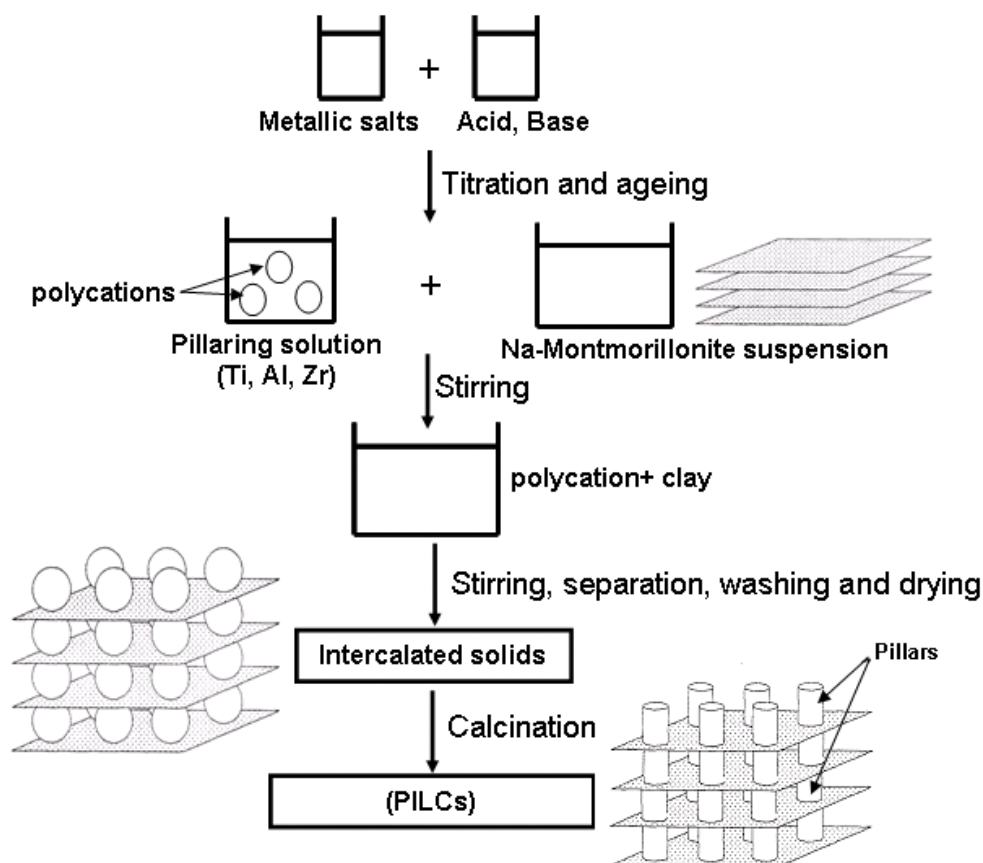


Figure 7.1: General preparation procedure of pillared clay (PILCs).

Factors influencing the pillaring process

A great variety of factors can influence the intercalation/pillaring process. First, several host clays can be used as parent materials. The intercalation into montmorillonite is, by far, the most documented process. Another factor to be considered is the intercalating solution. The $[\text{Al}_{13}\text{O}_4(\text{OH})_{24}(\text{H}_2\text{O})_{12}]^{7+}$ polyoxycation, usually denoted as Al_{13} , is the most widely used, mainly because the aluminum chemistry is very well known. Consequently, the Al-pillared clays are, by far, the most documented pillared clays. Pillaring with polycations formed upon the hydrolysis of Zr^{4+} , Ti^{4+} , Cr^{3+} , Fe^{3+} , or Ga^{3+} , among other elements, has also been reported (Kloprogge, 1998). In addition to the nature of the metallic cation, other important factors affecting the intercalating solutions should be taken into account, such as the conditions of hydrolysis, the concentration, the time and conditions of ageing, and so

forth. The washing, drying, and calcination processes have a great influence on the properties of the final solids, especially in the development of the porosity.

The insertion of metal oxide pillars into the interlayer region of the smectite group leads to the development of a new class of different thermally stable porous solids, because the pores formed between the layers can be systematically controlled by varying pillaring species. Thus, such materials have attracted more and more attention as a new type of porous solid, useful as a catalyst.

In this work, titanium, aluminum, and zirconium pillared clays were investigated. Titanium pillared clays have considerably large basal spacing ($d_{001}=1.8-2.4$ nm) and a large specific surface area SSA (260-350 m²/g) as well as high porosity (Romero *et al.*, 2006). Einaga, (1979) suggested the existence of $[(\text{TiO})_8(\text{OH})_{12}]^{4+}$ species in the pillaring solution, but the complex structure was not determined. Another work (Del Castillo, 1993) suggests the presence of $[\text{TiO}_2(\text{OH})_4]_n$. Thus the structure of the titanium polycation is still not well identified.

The Zr-PILCs are less investigated and documented in the literature because of the sensitivity of the Zr^{4+} species. The zirconyl ion is present as a tetrameric cation with the general formula $[\text{Zr}_4(\text{OH})_8(\text{H}_2\text{O})_{16}]^{8+}$ (Ohtsuka et al., 1993).

The calcination step converts the different polyoxycation precursors into their oxides pillars. During calcination, dehydration and dehydroxylation reactions of the charged pillars occur to give neutral oxide particles. This heating process has a great influence on the obtained porosity and stability.

7.1.2. Background in magnetism

Basic definitions (Morrish., (1965) and Moskowitz, (1991))

The magnetic properties of an atom arise as a result of interactions between the spin moment of the electron, μ , and the orbital moment, L , the contribution of the latter is of comparatively minor importance.

Important parameters used to characterize the magnetic properties of solids are summarized in Tab. 7.1.

Table 7.1: Basic definitions in magnetism

Magnetic term	Symbol	SI unit	CGS unit	Conversion factor
Magnetic moment	μ	A m^2	emu	$1 \text{ A m}^2 = 10^3 \text{ emu}$
Magnetic field	H	A/m	Oe	$1 \text{ A/m} = 4\pi/10^3 \text{ Oe}$
Magnetization	$M=\mu/\text{mass}$	$\text{A m}^2/\text{kg}$	emu/g	$1 \text{ A m}^2/\text{kg} = 1 \text{ emu/g}$
Magnetic susceptibility	$\kappa=M/H$	m^3/kg	emu/Oe g	$1 \text{ m}^3/\text{kg} = 10^3/4\pi \text{ emu/Oe g}$

A: Ampere, m: meter

Oe: Oersted

emu: electromagnetic unit.

When a substance is placed in a magnetic field of strength, H , the magnetization M (i.e. the magnetic moment of the sample per unit mass, is related to H by the magnetic susceptibility, χ , of the substance. Magnetic susceptibility can be used in a general way to describe the various classes of magnetic materials.

Types of magnetism

The best way to introduce the different types of magnetism is to describe how materials respond to a magnetic field.

The magnetic behaviour of materials can be classified into the following major groups (Fig. 7.2):

1- *Diamagnetism*

2- *Paramagnetism*

3- *Ferromagnetism*

4- *Ferrimagnetism*

5- *Antiferromagnetism*

Materials in the first two groups are those that are not magnetically ordered, however materials in the last three groups exhibit a magnetic order below a certain critical temperature.

1- Diamagnetism

Diamagnetic substances are composed of atoms which have no net magnetic moments (there are no unpaired electrons). However, when exposed to a field, a negative magnetization is produced and thus the susceptibility is negative. Note that when the field is zero the magnetization is zero. The other characteristic behaviour of diamagnetic materials is that the susceptibility is temperature independent.

2- Paramagnetism

This class of materials, some of the atoms have a net magnetic moment due to unpaired electrons. Application of a magnetic field causes random alignment of the atomic magnetic moment in the direction of the field, resulting in a positive magnetization and positive susceptibility, and like diamagnetism, the magnetization is zero when the field is removed. Magnetic susceptibility of paramagnetic materials is inversely proportional to the temperature and its behaviour is described by the Curie law equation:

$$\chi = C/T \quad (1)$$

where C is the Curie constant and T is the temperature.

3- Ferromagnetism

In a ferromagnetic material the magnetic moments of all atoms are aligned parallel to each other resulting in large spontaneous magnetization even in the absence of a magnetic field at temperatures below the Curie point, and therefore a large positive susceptibility.

In addition, ferromagnets can retain a memory of an applied field once it is removed, this behaviour is called hysteresis and plot of the variation of magnetization with magnetic field is called a hysteresis curve which will be presented later.

4- Ferrimagnetism

In a ferrimagnetic material atomic moments are ordered in an antiparallel sense, but the sum of the moment pointing in one direction exceeds those pointing in the opposite direction, so ferrimagnetic materials have a net magnetic moment. Ferrimagnetism is therefore similar to ferromagnetism and exhibits all the properties of ferromagnetic behaviour: spontaneous magnetization, Curie temperature, a large positive susceptibility, and hysteresis.

5- Antiferromagnetism

In an antiferromagnetic substance atomic moments are aligned in an antiparallel manner, such substances have zero overall magnetic moment. Antiferromagnetic materials have no hysteresis, but a small positive susceptibility that varies also with temperature.

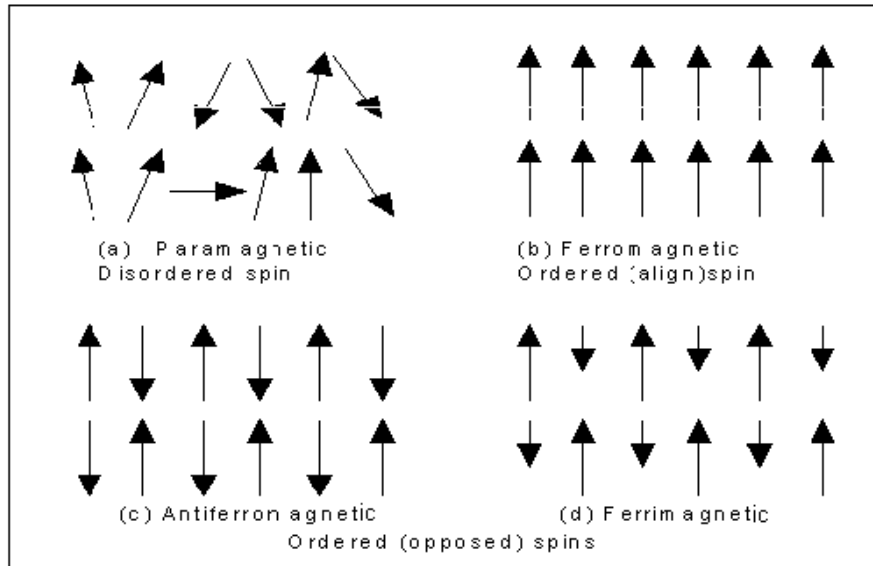


Figure 7.2: Summary of different types of magnetic behaviour.

Temperature dependency of susceptibility “Curie-Weiss law”

The magnetic susceptibility varies with temperature and its behaviour is described by the Curie-Weiss law in the paramagnetic region,

$$\chi = C / (T - \theta) \quad (2)$$

C and θ are the Curie constant and the Weiss constant, respectively and T is the temperature. Below a certain temperature (Curie or Néel) which depends on the substance itself, it undergoes a transition to a magnetically ordered state and becomes ferromagnetic, antiferromagnetic or ferrimagnetic. The transition temperature is termed the Curie temperature (T_c) for ferromagnetic and ferrimagnetic substances and the Néel temperature (T_N) for antiferromagnetic substances. However, above T_c and T_N materials behave as paramagnets, and they can be distinguished by their intercept on the temperature axis θ (Fig. 7.3).

$\theta > 0$, ferromagnetism.

$\theta < 0$, ferrimagnetism and antiferromagnetism.

$\theta = 0$, paramagnetism.

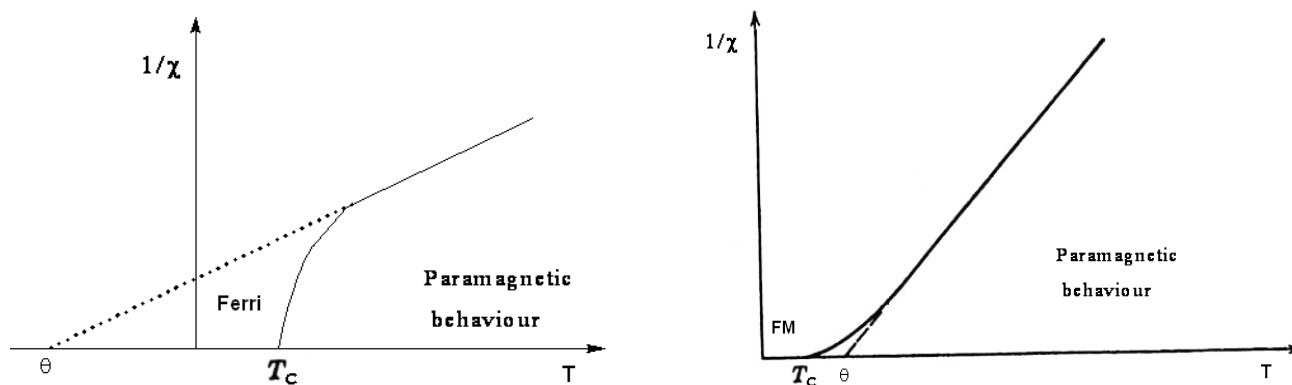


Figure 7.3: Illustration of the susceptibility of a ferromagnetic (FM) and ferrimagnetic (Ferri) materials.

Hysteresis curve and magnetic parameters

The plot of the variation of magnetization with magnetic field is called a hysteresis curve (Fig. 7.4). The saturation magnetization M_s is the magnetization when the magnetic material is saturated with the applied field. Upon reducing the field to zero, the magnetization does not go to zero but persists as a retentivity or remanent magnetization M_{rs} . Increasing the field in the negative direction, a point is reached where the induced magnetization becomes zero, the field at this point is called the coercivity H_c . Increasing the field further in the negative direction results in saturation again but in the negative direction. The various hysteresis parameters are intrinsic properties and are dependent on temperature. Another hysteresis property is the coercivity of remanence (H_{cr}), this is the field which, when applied and then removed, reduces the saturation remanence to zero. It is always larger than the coercive force. The magnetic squareness M_r/M_s , and H_c/H_{cr} ratio can be also deduced from the hysteresis curve.

The magnetic properties of iron compounds can be determined by using magnetometry. Some magnetic parameters such as magnetic order, Curie or Néel temperature, and saturation magnetization are collected in Tab. 7.2.

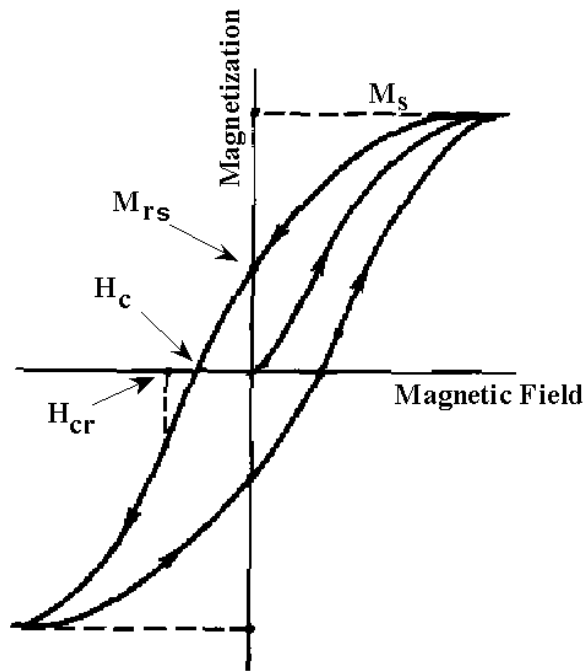


Figure 7.4: Hysteresis curve

Table 7.2: Magnetic properties of iron minerals.

Minerals	Composition	Magnetic order	T_c (T_N) ($^{\circ}\text{C}$)	M_s ($\text{A m}^2/\text{kg}$)
Oxides				
Magnetite	Fe_3O_4	Ferri	575-585	90-92
Hematite	$\alpha\text{-Fe}_2\text{O}_3$	Canted AFM	675	0,4
Maghemite	$\gamma\text{-Fe}_2\text{O}_3$	Ferri	~ 600	~ 80
Oxyhydroxides				
Goethite	$\alpha\text{-FeOOH}$	AFM, weak FM	~ 120	< 1
Lepidocrocite	$\gamma\text{-FeOOH}$	AFM (?)	-196	
Feroxyhite	$\delta\text{-FeOOH}$	Ferri	~ 180	< 10
Metals				
Iron	Fe	FM	770	218

FM: Ferromagnetic order.

Ferri: Ferrimagnetic order.

AFM: Antiferromagnetic order.

T_c : Curie temperature.

T_N : Néel temperature.

M_s : Saturation magnetization at room temperature.

7.2. Ti-M-PILC hysteresis

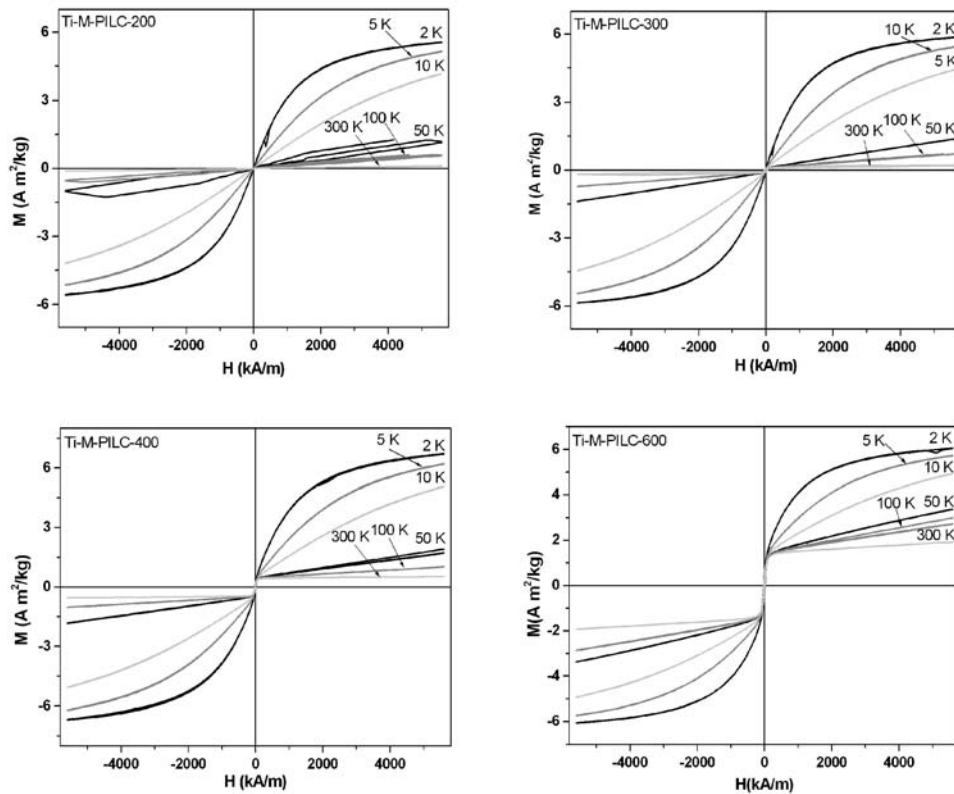


Figure 7.5: Hysteresis loops of Ti-M-PILC-200, -300, -400, and -600 (full range).

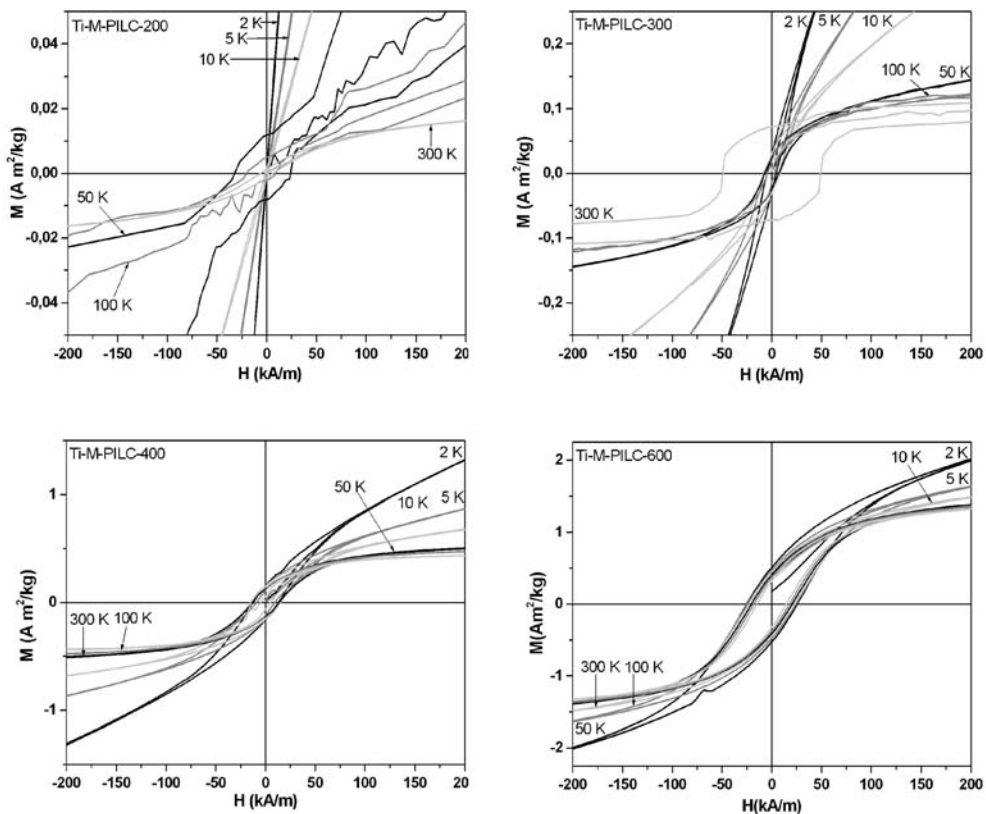


Figure 7.6: Hysteresis loops of Ti-M-PILC-200, -300, -400, and -600 (zoom of loops).

7.3. Abbreviations list

PILC	Pillared clays
M-PILC	Magnetic pillared clays
XRD	X-ray diffraction
d_{001}	Basal spacing
EG	Ethylene glycol
D	Crystal size
k	Shape factor with (0.9)
λ	Wavelength
FWHM (β)	Full width at half maximum
SSA	Specific surface area
V_p	Pore volume at $p/p_0 = 0.7$ (pore width ≤ 7 nm)
V_{mp}	Micropore volume (width less than 2 nm)
V_{mes}	Mesopore volume (width between 2 and 50 nm)
NLDFT	Non local density functional theory
PSD	Pore size distribution
XRF	X-ray fluorescence
LOI	Loss on ignition
CEC	Cationic exchange capacity
r.h.	Relative humidity
ICP-OES	Inductively coupled plasma-optical emission spectroscopy
ξ	Layer charge
M	Molecular weight
f.u	Formula unit
u.c	Unit cell
STA	Simultaneous thermal analyses
DTA	Differential thermal analysis
DSC	Differential scanning calorimetry
TG	Thermogravimetry
H ₂ O-MS	H ₂ O-mass spectrometer
CO ₂ -MS	CO ₂ -mass spectrometer
FTIR-ATR	Attenuated total reflection infrared spectroscopy
FIR	Far infrared spectroscopy
ESEM	Environmental scanning electron microscope

μ	Magnetic moment
H	Magnetic field
M	Magnetization
χ	Magnetic susceptibility
T_c	Curie temperature
T_N	Néel temperature
AGM	Alternating gradient magnetometer
SQUID	Superconducting quantum interference devices
M_s	Specific saturation magnetization
M_{rs}	Saturation remanent magnetization
H_c	Coercivity
H_{cr}	Coercivity of remanence
M_{rs}/M_s	Magnetic squareness
SD	Single domain
MD	Multi domain
PSD	Pseudo-single domain
SPM	Superparamagnetism
ZFC	Zero-field-cooled
FC	Field-cooled
χ_{FC}	Field-cooled susceptibility
χ_{ZFC}	Zero-field-cooled susceptibility
θ	Weiss constant
C	Curie constant
N	Atoms/cm ³
μ	Number of magnetons
μ_B	Bohr magneton ($9.27400915(23) \times 10^{-24} \text{ J T}^{-1}$)
k	Boltzmann's constant, ($1.3806504(24) \times 10^{-23} \text{ J K}^{-1}$)
IS	Isomer shift
QS	Electric quadrupole splitting
B_{hf}	Magnetic hyperfine field
FF	Filling factor
IF	Intercalation factor
V_{ILthe}	Theoretical interlayer volume
V_{ILexp}	Experimental interlayer volume

V_{PL}	Pillar volume
d_{IN}	Interlayer space
a, b	Montmorilloniute unit cell dimensions
N_{av}	Avogadro number ($6.023 \cdot 10^{23}$)
AAS	Atomic adsorption spectrometry
q_e	Amount of the sorbate at equilibrium
C_e	Equilibrium concentration
q_m	Maximum metal uptake capacity or monolayer capacity
b	Coefficient related to the affinity between the metal ion and the sorbent.
K_f	Freundlich empirical constant indicative of sorption capacity
n	Freundlich empirical constant indicative of sorption intensity
q_t	Value of amount adsorbed per unit mass at any time t
k_1	Pseudo-first-order adsorption rate constant
K_i	Diffusion rate constant
k_2	Pseudo-second-order adsorption rate constant
q_{eExp}	Experimental amount of the sorbate at equilibrium

8. References

Bachir, C., Lan, Y., Mereacre, V., Powell, A.K., Koch, C.B., and Weidler, P.G. (2009) Magnetic titanium pillared clays (Ti-M-PILCs): Magnetic studies and Mößbauer spectroscopy. *Clays and Clay Minerals*, **57**, 433-443.

Bouberka, Z., Khenifi, A., Sekrane, F., Bettahar, N., Derriche, Z. (2008) Adsorption of direct Red 2 on bentonite modified by cetyltrimethylammonium bromide. *Chemical Engineering Journal*, **136**, 295-305.

Bouchenafa-Saib, N., Khouli, K. and Mohammedi, O. (2007) Preparation and characterization of pillared montmorillonite: application in adsorption of cadmium. *Desalination*, **217**, 282-290.

Bouras, O. (2003) Propriétés adsorbantes d'argiles pontées organophiles: synthèse et caractérisation. Thèse, Faculté des sciences et techniques, Université de Limoges.

Brindley, G. W. and Brown, G. (1980) Crystal structures of clay minerals and their X-ray identification. Mineralogical Society, Monograph **5**, London, p. 539.

Brunauer, S., Emmett, P. H. and Teller, E. (1938) Adsorption of gases in multimolecular layers. *Journal of the American Chemical Society*, **60**, 309-319.

Caglioti, G., Paoletti, A., and Ricci, F.P. (1958) Choice of collimators for a crystal spectrometer for neutron diffraction. *Nuclear Instruments*, **3**, 223-228.

Chaabene, S.B., Bergaoui, L. and Ghorbel, A. (2004) Zirconium and sulphated zirconium pillared clays: a combined intercalation solution study and solid characterization. *Colloids and Surfaces A: Physicochem. Eng. Aspects*, **251**, 109-115.

Chipera, S.J. and Bish, D.L. (2001) Baseline studies of the clay minerals society source clays: Powder X-ray diffraction analyses. *Clays and Clay Minerals*, **49**, 398-409.

Chipera, S.J. and Bish, D.L. (1993) Effects of humidity on clay and zeolite quantitative XRD analyses. *Proceedings of the 30th Annual Clay Minerals Society Meeting, San Diego, California*, p. 53.

Cool, P., and Vansant, E.F. (1998) Pillared clays: Preparation, characterization and applications. *Molecular Sieves*, **1**, 265-288.

Del Castillo, H.L., Grange, P. (1993) Preparation and catalytic activity of titanium pillared montmorillonite. *Applied Catalysis A: General*, **103**, 23-34.

Doyurum, S. and Celik, A. Pb(II) and Cd(II) removal from aqueous solutions by olive cake, *Journal of Hazardous Materials*, **138**, (2006) 22-28.

Einaga, H. (1979) Hydrolysis of titanium (IV) in aqueous (Na, H)Cl solutions, *Journal of the Chemical Society, Dalton Transactions*, **12**, 1917-1919.

Elmchaouri, A. and Mahboub, R. (2005) Effects of preadsorption of organic amine on Al-PILCs structures. *Colloids and Surfaces A: Physicochem. Eng. Aspects*, **259**, 135-141.

Farmer, V.C. (1974) The infrared spectra of minerals. Monograph **4**, Mineralogical Society, London.

Freundlich, H.M.F. (1906) Über die Adsorption in Lösungen, *Zeitschrift für Physikalische Chemie*, **57**, 385-470.

- Greene-Kelly, R. (1966) The montmorillonite minerals (smectites) in the differential thermal investigation of clays. Mackenzie, R. C. (editor), Mineralogical Society, London, 140-164.
- Han, Y.S., and Yamanaka, S. (1998) Preparation and adsorption properties of mesoporous pillared clays with silica sol. *Journal of Porous Materials*, **5**, 111-119.
- Han, Y.S., Matsumoto, H., and Yamanaka, S. (1997), Preparation of New Silica Sol-Based Pillared Clays with High Surface Area and High Thermal Stability *Chemistry of Materials*, **9**, 2013-2019.
- Ho, Y.S. and McKay, G. (1999) The sorption of lead (II) ions on peat. *Water Research*, **33**, 578-584.
- Ho, Y.S. and McKay, G. (1998) Sorption of dye from aqueous solution by peat. *Chemical Engineering Journal*, **70**, 115-124.
- Hofmann, V. and Klemen, R. (1950), Verlust der Austausch fähigkeit von Lithiumionen und Bentonit durch Erhitzung, *Zeitschrift für anorganische und allgemeine Chemie*, **262**, 95-99.
- Hutson, N.D. (1999) Control of microporosity of Al₂O₃-pillared clays: effect of pH, calcination temperature and clay cation exchange capacity. *Microporous and Mesoporous Materials*, **28**, 447-459.
- Ishii, M., Shimanouchi, T. and Nakahira M (1967) Far-infrared absorption spectra of layer silicates. *Inorganica Chimica Acta*, **1**, 387-392.
- Jasmund, K. and Lagaly.G. (1993) *Tonminerale und Tone. Struktur, Eigenschaften, Anwendung und Einsatz in Industrie und Umwelt (Gebundene Ausgabe)*.
- Jenkins, R. and de Vries, J. L. (1970) *An Introduction to X-Ray Powder Diffractometry*, Eindhoven-Philips Gloeilampenfabrieken, Holland, p. 27.
- Johansson, G. (1960) On the crystal structures of some basic aluminum salts. *Acta Chemica Scandinavica*, **14**, 771-773.
- Kloprogge, J.T. (1998) Synthesis of smectites and porous pillared clay catalysts: A review. *Journal of Porous Materials*, **5**, 5-41.
- Khalaf, H., Bouras, O, and Perrichon, V. (1997) Synthesis and characterization of Al-Pillared and cationic surfactant modified algerian bentonite, *Microporous Materials*, **8**, 141-150.
- Köster, H.M. (1977) Die Berechnung kristallchemischer Strukturformeln von 2:1-Schichtsilikaten unter Berücksichtigung der gemessenen Zwischenschichtladungen und Kationenumtauschkapazitäten, sowie der Darstellung der Ladungsverteilung in der Struktur Mittels Dreieckskoordinaten. *Clay Minerals*, **12**, 45-54.
- Lagaly, G. (1981) Characterization of clays by organic compounds. *Clay Minerals*, **12**, 45-54.
- Lagaly, G. (1994) Layer charge determination by alkylammonium ions in layer charge characteristics of 2:1 silicate clay minerals. Mermut, A.R. editor, *Workshop Lecture Volume. The Clay Minerals Society*, **6**, 1-46.
- Lagergren, S. (1898) Zur Theorie der sogenannten Adsorption gelöster Stoffe, *Kungliga Svenska Vetenskapsakademiens, Handlingar*, Band 24, 1-39.
- Langmuir, I. (1916) The constitution and fundamental properties of solids and liquids, *Journal of the American Chemical Society*, **38**, 2221-2295.

- Lenoble, V., Bouras, O., Deluchat, V., Serpaud, B., and Bollinger, J-C. (2002) Arsenic adsorption onto pillared clays and iron oxides. *Journal of Colloid and Interface Science*, **255**, 52-58.
- Levin, I., Brandon, D. (1998) Metastable Alumina Polymorphs: Crystal Structures and Transition Sequences. *Journal of the American Ceramic Society*, **81**, 1995-2012.
- Lowell, S., Shields, J.E., Thomas, M.A., and Thommes, M. (2006) Characterization of porous solids and powders: surface area, pore size and density. *Particle Technology Series*. P 11.
- Manohar, D.M., Noeline, B.F. and Anirudhan, T.S. (2006) Adsorption performance of Al-pillared bentonite clay for the removal of cobalt (II) from aqueous phase. *Applied Clay Science*, **31**, 194-206.
- Mackenzie, R.C. (1970) Simple phyllosilicates based on Gibbsite- and Brucite-like sheets in differential thermal analysis. Mackenzie, R. C. (editor), Academic Press, London, New York, 497-537.
- Madejova, J. and Komadel, P. (2001) Baseline studies of the clay minerals society source clays: infrared methods. *Clays and Clay Minerals*, **49**, 410-432.
- Maes, N., Heylen, I., Cool, P. and Vansant, E.F. (1997) The relation between the synthesis of pillared clays and their resulting porosity. *Applied Clay Science*, **12**, 43-60.
- Mak, S.Y. and Chen, D.H. (2004) Fast adsorption of methylene blue on polyacrylic acid bound iron oxide magnetic nanoparticles. *Dyes Pigments*, **61**, 93-98.
- Meier, L.P. and Kahr, G. (1999) Determination of the cation exchange capacity (CEC) of clay minerals using the complexes of copper (II) ion with triethylenetetraamine and tetraethylenepentamine. *Clays and Clay Minerals*, **47**, 386-388.
- Mermut, A.R. and Lagaly, G. (2001) Baseline studies of the clay minerals society source clays: Layer-charge determination and characteristics of those minerals containing 2:1 layers. *Clays and Clay Minerals*, **49**, 393-397.
- Mishra, B.G. and Rao, G.R. (2005) Cerium containing Al- and Zr-pillared clays: Promoting effect of cerium (III) ions on structural and catalytic properties. *Journal of Porous Material*, **12**, 171-181.
- Moore, D.M. and Reynolds Jr., R.C. (1997) X-ray diffraction and the identification and analysis of clay minerals. 2 ed., University Press, Oxford, p. 241.
- Morrish, A.H. (1965) *The Physical Principles of Magnetism*, Jhon Wiley & Sons, Inc. New York. London. Sydney.
- Moskowitz, B. M. (1991) Hitchhiker's guide to magnetism. The Environmental Magnetism Workshop. Institute for Rock Magnetism, University of Minnesota.
- Mössbauer, R.L., (1958) Kernresonanzfluoreszenz von Gammastrahlung in IR-191. *Zeitschrift für Physik*, **151**, 124.
- Naguib, N., Weidler, P.G., and Nüesch, R. (2003), Development of the application of magnetic micro-sorbents for the elimination of hazardous inorganic contaminants from natural waters. 10th Conference of the European Clay Groups Association, volume abstracts, p. 202.
- Neimark, A.V. and Ravikovitch, P.I. (2001) Capillary condensation in MMS and pore structure characterization. *Microporous and Mesoporous Materials*, **44**, 697-707.

- Niederbudde, E.-A., Stanjek, H. and Emmerich, K. (2002) Tonminerale Methodik in Handbuch der Bodenkunde.
- Ohtsuka, K., Hayashi, Y., Souda, M. (1993) Microporous ZrO₂-Pillared Clays Derived from Three Kinds of Zr Polynuclear Ionic Species. *Chemistry of Materials*, **5**, 1823-1829.
- Olis, A.C., Malla, P.B., and Douglas, L.A. (1990) Therapi destination of the layer charges of 2:1 expanding clays from a singlealk ylammonium ion expansion. *Clay Minerals*, **25**, 39-50.
- Oliveira, L.C.A., Rios, R.V.R.A., Fabris, J.D., Garg, V.K., Sapag, K. and Lago, R.M. (2002) Activated carbon/iron oxide magnetic composites for the adsorption of contaminants in water. *Carbon*, **40**, 2177-2183.
- Oliveira, L.C.A., Rios, R.V.R.A., Fabris, J.D., Sapag, K., Garg, V.K. and Lago, R.M (2003) Clay-iron oxide magnetic composites for the adsorption of contaminants in water. *Applied Clay Science*, **22**, 169-177.
- Peigneur, P., Maf, .S A. and Cremers, A. (1975) Heterogeneity of charge density distribution in montmorillonite as inferred from cobalt adsorption. *Clays and Clay Minerals*, **23**, 71-75.
- Prost, R. and Laperche, V. (1990) Far-infrared study of potassium in micas. *Clays and Clay Minerals*, **38**, 351 - 355.
- Ravikovitch, P.I. and Neimark, A.V. (2001) Characterization of nanoporous materials from adsorption and desorption isotherms. *Colloids and Surfaces A: Physicochemical and Engineering Aspects*, **187**, 11-21.
- Romero, A., Dorado, F., Asencio, I., Garcia, P.B., and Valverde, J.L. (2006) Ti-pillared clays: synthesis and general characterization. *Clays and Clay Minerals*, **54**, 737-747.
- Rozenon, I. and Heller-Kallai, L. (1976) Reduction and oxidation of Fe³⁺ in dioctahedral smectites –1: Reduction with hydrazine and dithionate. *Clays and Clay Minerals*, **24**, 271-282.
- Rühlicke, G. and Kohler, E.E. (1981) A simplified procedure for determining layer charge by the n-alkylammonium method. *Clay Minerals*, **16**, 305-307.
- Schecher, W.D. and McAvovy, D.C. (2003).MINEQL+: A Chemical Equilibrium Program for Personal Computers, User Manual Version 4.5, Environmental Research Software, Hallowell, ME.
- Schoonheydt, R.A., Pinnavaia, T., Lagaly, G. (1999) Pillared clays and pillared layered solids. *Pure Applied Chemistry*, **71**, 2367-2371.
- Schuette, R., Goodman, B.A., Stucki, J.W. (2000)Magnetic properties of oxidized and reduced smectites. *Physics and Chemistry of Minerals*, **27**, 251-257.
- Seaton, N.A., Walton, J.P.R.B., and Quirke, N. (1989) Anew analysis method for the determination of the pore size distribution of porous carbons from nitrogen adsorption measurements. *Carbon*, **27**, 853-861.
- Sing, K.S.W., Everett, D.H., Haul, R.A.W, Moscou, L., Pierotti, R.A, Rouquérol, J., Siemieniewska, T. (1985) Reporting physisorption data for gas/solid systems with special reference to the determination of surface area and porosity. *Pure and Applied Chemistry*, **57**, 603-619.
- Sterte, J. (1986), Synthesis and properties of titanium oxide cross-linked montmorillonite. *Clays and Clay Minerals*, **34**, 658-664.

Steudel, A. (2008) Selection strategy and modification of layer silicates for technical applications. Dissertation, Fakultät für Bauingenieur-, Geo- und Umweltwissenschaften der Universität Karlsruhe.

Stokes, G.G. (1845) On the theories of internal friction of the fluids in motion. *Transactions of Cambridge Philosophy Society*, **8**, 287-319.

Suzuki, M., Suzuki, I.S. and Walter, J. (2003) Quasi-two-dimensional magnetism in Ru and Rh metal layers sandwiched between grapheme sheets. *Physical Review B*, **67**, 094406.

Thommes, M., Smarsly, B., Groene, M., Ravikovitch, P.I. and Neimark, A.V. (2006) Adsorption hysteresis of nitrogen and argon in pore networks and characterization of novel micro- and mesoporous silicas. *Langmuir*, **22**, 756-764.

Valverde, J.L., Sánchez, P., Dorado F., Molina C.B., Romero A. (2002) Influence of the synthesis conditions on the preparation of titanium-pillared clays using hydrolyzed titanium ethoxide as the pillaring agent. *Microporous and Mesoporous Materials*, **54**, 155-165.

Valverde, J.L., Sánchez, P., Dorado, F., Asencio, I., Romero, A (2003) Preparation and characterization of Ti-pillared clays using Ti alkoxides: Influence of the synthesis parameters. *Clays and Clay Minerals*, **51**, 41-51.

Van Olphen, H. (1963) *An Introduction to Clay Colloid Chemistry*, 2nd edition. Wiley, New York.

Van Wonerghem, J., Morup, S., J. W. Koch, C., W. Charles, S. and Wells. S. (1986) Formation of ultra-fine amorphous alloy particles by reduction in aqueous solution. *Nature*, **322**, 622-623.

Velde, B. and Couty, R. (1985) Far Infrared Spectra of Hydrous Layer Silicates. *Physics and Chemistry of Minerals*, **12**, 347 - 352.

Vogt, K. and Köster, H.M. (1978) Zur Mineralogie, Kristallchemie und Geochemie einiger Montmorillonite aus Bentoniten. *Clay Minerals*, **13**, 25-43.

Weber, Jr.W.J., Morris, J.C. (1963) Kinetics of adsorption on carbon from solution. *Journal of the Sanitary Engineering Division, ASCE*, **89**, 31-60.

William, F. and Moll, J. (2001) Baseline Studies of the Clay Minerals Society Source Clays: Geological Origin. *Clays and Clay Minerals*, **49**, 374-380.

Yamanaka, S. and Brindley, G.W. (1979) High surface area solids obtained by reaction of montmorillonite with zirconyl chloride. *Clays and Clay Minerals*, **27**, 119-124.

Zhang. L and Manthiram. A (1996) Ambient temperature synthesis of fine metal particles in montmorillonite clay and their magnetic properties. *NanoStructured Materials*, **7**, 437-451.

Zhang, Z. D., Yu, J. L., Zheng, J. G., Skorvanek, I., Kovac, J., Dong, X. L., Li, Z. J., Jin, S. R., Yang, H. C., Guo, Z. J., Liu, W. and Zhao, X. G. (2001) Structure and magnetic properties of boron-oxide-coated Fe(B) nanocapsules prepared by arc discharge in diborane. *Physical Review B*, **64**, 024404.